CERN-ACC-NOTE-2020-0023

Review of LEIR operation in 2018

S. Albright, R. Alemany Fernández, M. E. Angoletta, H. Bartosik, A. Beaumont, G. Bellodi, N. Biancacci, M. Bozzolan, M. Buzio, F. Di Lorenzo, A. Frassier, D. Gamba, S. Hirlander, A. Huschauer, S. Jensen, V. Kain, G. Kotzian, D. Kuchler, A. Latina, T. Levens, E. Mahner, E. Manosperti, O. Marqversen, D. Moreno, D. Nicosia, M. O'Neil, E. Ozturk, A. Saa Hernandez, R. Scrivens, G. Tranquille, C. Wetton, M. Zampetakis.

Keywords: CERN, LEIR, ion chain, Pb, beam performance, 2018 operation, beam parameters

Summary

During run 2 (2015-2018) the LEIR machine experienced several important improvements in terms of extracted intensity, driven by the LHC Injectors Upgrade (LIU) project requirements. In 2018 the machine not only gave another step forward in extracted intensity, but also demonstrated that it could deliver the LIU target intensity in a reproducible and reliable way. The main steps that allowed the high performance reach of the NOMINAL beam and improvements to the machine stability are detailed in this paper. This work is also intended to be a reference for the restart after the Long Shutdown 2.

Contents

1 Introduction

In the context of the LHC Injector Upgrade (LIU) project (1; 2), which aims at upgrading the existing accelerator chain in view of the increased beam performance required for the High Luminosity LHC era, an intense program of machine development (MD) studies were launched in LEIR during run 2. The aim being to understand and overcome the intensity limitations that were restricting the extracted lead beam intensity to values almost a factor two below the required LIU target of $9 \cdot 10^{10}$ charges extracted, as can be seen in Fig. 1. The red lines in the figure indicate the extracted intensity from LEIR before 2015 and the LIU target; the evolution of the intensity over the NOMINAL cycle during run 2 is also visible in the plot[1].

Several factors contributed to the performance improvements as from 2015. On one hand the optimization of the machine settings to avoid losses at resonances, and the optimization of the RF capture for the bunch profile flattening in the double harmonic RF system to minimize transverse space charge effects. In addition, the beam intensity from Linac 3 could be increased in 2016 by almost 40% compared to 2015 following a source extraction system aperture restriction removal. Since 2016 LEIR could deliver intensities above the LIU target.

The main challenges left for the 2018 run were to demonstrate that the LIU intensities could be delivered in a reliable and stable way during operation, together with pursuing a deeper understanding of the performance limitations. Therefore, the machine experienced another year of important improvements in performance, from both extracted intensity and stability of operation point of views. In 2018 it was possible to extract 10% more intensity from the NOMINAL cycle, as shown in Fig. 1, and guarantee, on average, a stable operation above the LIU target. This significant achievement was possible thanks to the remarkable LEIR and Linac 3 team efforts. The machine operation was largely improved thanks to innovative ad-hoc optimization tools and the identification of performance degradation sources. On the machine development side, several studies were done on impedance, space charge, and electron cooling: the source of the fast vertical instability was identified (old transverse feedback pickup) and suppressed by appropriate cable termination; Intra Beam Scattering (IBS) was observed to play an important role at capture together with space charge; the electron cooler was further characterised. Studies were also done to extend the injection plateau to accommodate 8 injections with a faster ramp rate, and on the new transfer line optics to better match the PS periodic solution. Last but not least, 2018 has seen the NOMINAL beam operating with accelerating harmonic 3 and shaping harmonic 6 (h = 3+6) which allowed LHC to achieve 67% of the LIU target on total intensity compared to 58% for the h=2+4 case. In the following sections we will present a summary of the machine software and hardware upgrades (Sec. 2), the low and high level RF operation in 2018 (Sec. 3), and the new White Rabbit B-train implementation and results of the reliability run (Sec. 4). We will also give an overview of the NOMINAL beam setup from an operational point of view (Sec. 5) and the performance and stability reached in 2018 (Sec. 6), together with a summary of the main machine studies (Sec. 7).

[1] 2017 is not illustrated because the ion complex operated Xenon beams that year.

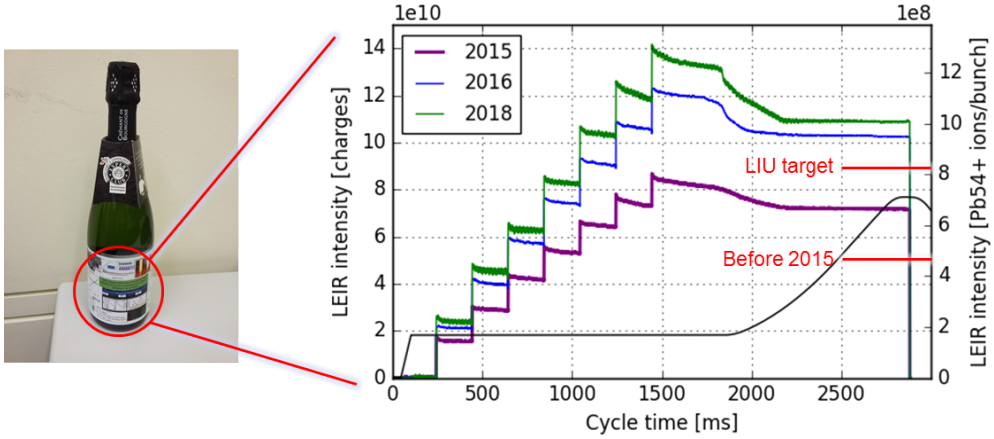

Figure 1: LEIR intensity of the NOMINAL cycle from 2016 to 2018 (with exception of 2017 when LEIR operated with Xe39+).

2 Hardware and software upgrades

2.1 Optimization tools

Various processes in LEIR are poorly instrumented and models are not always available on-line. Examples are the LEIR multi-turn injection and electron cooling. These aforementioned processes are sensitive to changing conditions, such as intensity and energy distribution from Linac 3, orbit in LEIR or injected trajectory. Until recently, these processes were manually tuned at start-up and re-tuned manually over and over again in case of drifts, with impact on reproducibility, efficiency and maximum achievable performance. In spring 2018 numerical optimizers were therefore made available in the LEIR control room. The most frequently used numerical optimizer was the *Powell method* (3). It is one of the most intuitive algorithms and is also known as conjugate direction method. It is initialised with a set of search vectors (usually along the directions of the various degrees of freedom, each with an adequate step size) as well as an initial guess for the minimum (very often the current setting of all degrees of freedom). The algorithm then minimises the objective function by bi-directional line search along these search vectors and derives a new minimum setting for all degrees of freedom as well as new search vectors, which are then linear combinations of the original search vectors. This carries on until the convergence criterion for the minimum is reached. Other methods such as the *Nelder-Mead* (4) algorithm were made available as well. All these algorithms are available in python's *Scipy* library. The CERN accelerator equipment can be interfaced through python and hence a *PyQt* application was provided to launch and configure optimizers. The objective was to maximise injected intensity by optimizing the injected trajectory (x, x', y, y') using 4 bends at the end of the line or only ETL.BHN10, the injection orbit at the injection point or also the orbit bumps at the e-cooler section to maximise the accumulated intensity. The tool could optimize discrete settings or functions (i.e. the injection plateau). Figure 2 shows a screenshot of the tool in the control room.

The LEIR optimizer did not only allow a quick recovery of performance after changes

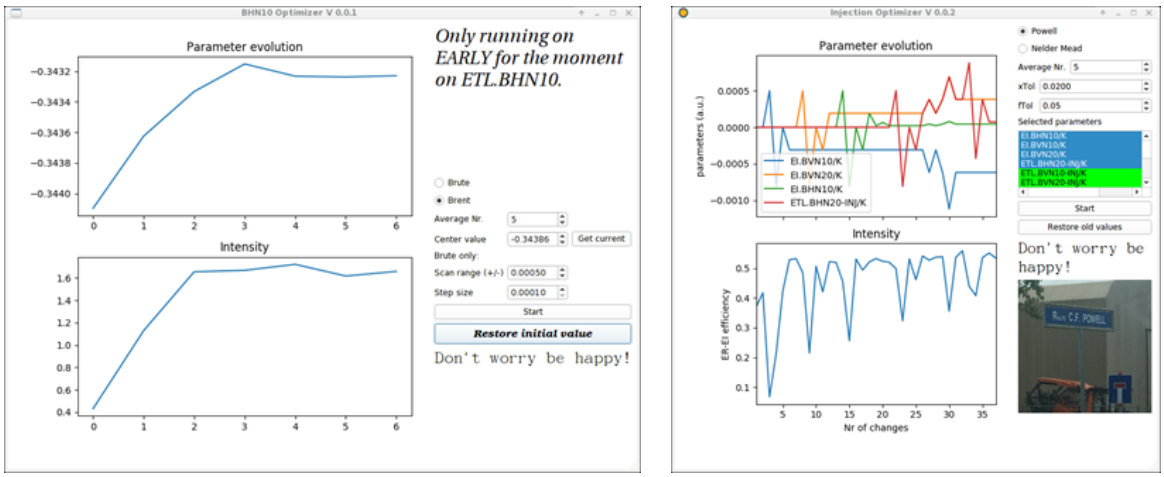

Figure 2: On the left, the ETL.BHN10 optimizer, on the right, the optimization of the LEIR injection bump. The corrections are reported on the top plot, while the achieved intensity is reported at the bottom.

and improved reproducibility, but it also allowed to reach a record injection efficiency of more than 80% (see Fig. 3 as an example) in comparison to the 70% of the machine design report (5).

For future LEIR runs, the tool needs to be extended to include more powerful derivative free algorithms (e.g. COBYLA, BOBYQA, Bayesian optimization, extremum seeking) and generalise optimization of function settings from plateaus only to any function segments.

2.2 Transfer line Beam Position Monitors and Secondary Emission Monitor grids

During 2017 and 2018 nine new Beam Position Monitors (BPMs), also called pickups, have been installed along the transfer line connecting Linac 3 to LEIR as illustrated in Fig. 4.

An example of the device is shown in Fig. 5. Previously there were no BPMs in the line, only Beam Screens and Secondary Emission Monitors (SEMs). Table 1 summarises the main specifications for the LEIR transfer line BPM system.

Parameter	Value	Comment
Accuracy	0.5 mm	-
Resolution	0.2 mm	For 4 μA current
Time resolution	1 μs	Along 200 μs pulse
Max. beam displacement	$\pm$15 mm	-
Max. beam current	50 μA	-
Number of injections	1-13	Every 100-200 ms

Table 1: Summary of the main specifications for the LEIR transfer line BPM system.

Initially a charge amplifier based acquisition system was installed, in order to measure

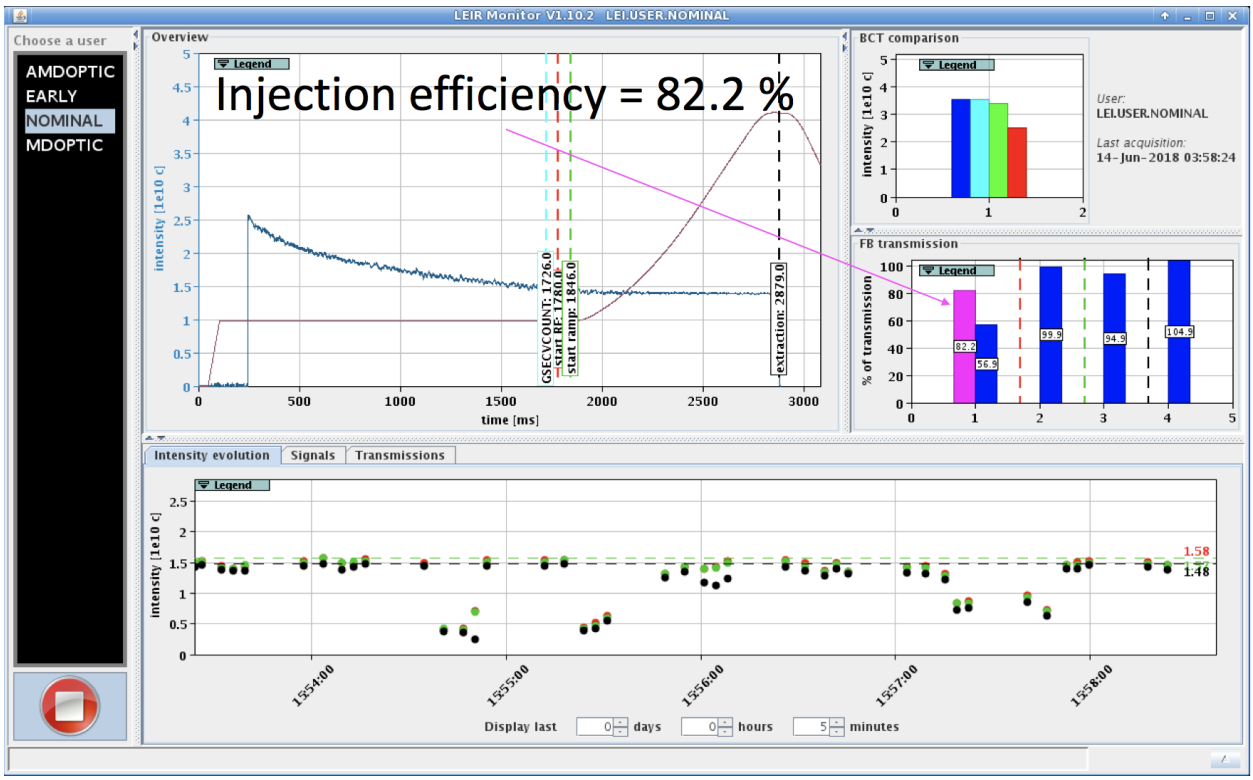

Figure 3: An example of the injection efficiency achieved after beam trajectory steering by the LEIR optimizer from the LEIR monitor application. A NOMINAL cycle is shown with one injection. On the top left plot the intensity evolution versus time is shown, with dashed lines representing the end of cooling (cyan), start of RF capture (red), start of the ramp (green), extraction (black). The top right plot shows the injected intensity along the line from the ITH (blue) and ETL (cyan and green) BCTs to the LEIR ring (red). The injection efficiency is given in the middle right plot by the magenta bar, together with the transmission efficiency from injection to the end of cooling. The remaining blue bars respectively refer to the transmission efficiency during capture, acceleration and extraction to the PS (red-green-black dashed lines in the intensity evolution plot). At the bottom, the intensity at capture (red dots), start of the ramp (green dots) and extraction (black dots) is shown versus time. In 2018 there were cases of efficiency even above 80% in comparison to the 70% of the machine design report (5).

the image charge of the beam on the electrodes, but it was discovered that this solution suffers heavily from spurious electrons charging the electrodes (6).

Despite the efforts to understand the phenomena and mitigate the electrons charging by means of repelling voltages and a solenoidal magnetic field, an accurate position measurement was not possible. Consequently, a different acquisition system has been developed exploiting the 101.3 MHz bunching component of Linac 3, which was tested during 2018 using 3 BPMs. The drawback of the new system is its dependence on the amplitude of the 101.3 MHz component of the beam current, and that it does not work for unbunched beams. However, the operational beam must be bunched, and the BPM sum signals could be additionally used for bunching debug purposes by comparing their shape to the BCT signals.

Figure 4: Nine new BPMs installed in the injection lines ITE (blue), ETL (red) and EI (purple) to allow a better trajectory measurement of the Linac 3 pulses injected into the LEIR machine (at the bottom-right).

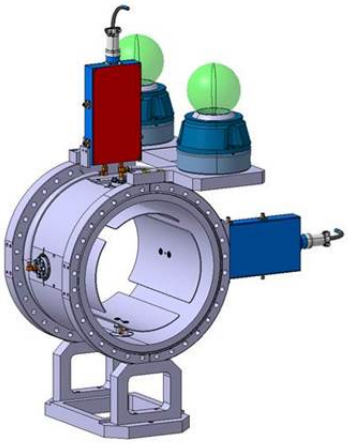

Figure 5: 3D pickup view.

The new acquisition system is based on an analogue frontend performing down-mixing and amplification of the pickup signals, with each electrode processed individually. The schematic blocks can be seen in Fig. 6. A local oscillator (LO) of 91.09 MHz is used to obtain the 10.2 MHz IF signal, sampled by the STRUCK SIS3300 ADC card running at a maximum of 100 MS/s.

All the electronics are moved outside of the transfer line tunnel, which will make maintenance and repair easier. Position is calculated by the FESA class using the Δ/Σ algorithm based on the amplitude of the down-mixed signal. To be noted that even if the individual Δ and Σ signals are dependent on the bunch length (i.e. 101.3 MHz component), this is not the case for the position.

Insensitivity to the spurious electrons charging the electrodes, the new acquisition system has been commissioned by comparing the sum signals of the horizontal and vertical planes

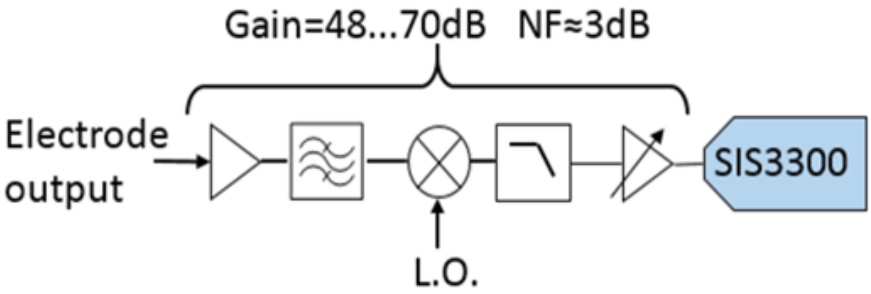

Figure 6: New analogue front end schematic blocks.

for the same BPM, Fig. 7, and also for different BPMs as compared in Fig. 8 relying on the fact that beam losses are very low. An MDEARLY cycle without energy ramping of the Linac 3 pulse, i.e. a mono-energetic beam, was setup to have an almost flat dispersive trajectory (Fig. 8) along the pulse. This condition removes the sum signal dependence on the position.

A 220 kHz modulation on the sum signal (which is proportional to the beam current) is evident in Fig. 8. Further investigation of the origin, maybe in Linac 3, is foreseen in the next run when all the nine BPMs will be upgraded. A calibration system to take into account the channels mismatches correction is also foreseen, with the complementary function of system functionality check.

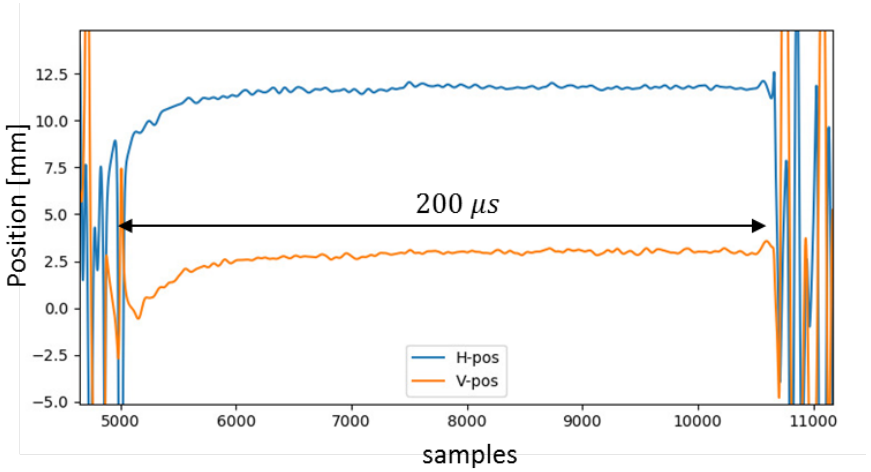

Figure 7: Horizontal and vertical position at EI.BPMI30 with no energy ramping from Linac 3 sampled at 25 MS/s.

During the Year End Technical Stop (YETS) 2017-2018 the ETL semgrids acquisition electronics were upgraded to a new version with different signal processing for the incoming beam from Linac 3 (200 μs long pulse, energy ramping along the pulse duration) and the extracted beam to PS (200 ns bunch length with bunch to bucket injection). The linear amplification of the Linac 3 energy-ramped pulse with an ADC sampling rate of 4 μs allowed acquisition of the change in beam position over the 200 μs Linac 3 pulse, and first measurements of the dispersion. For the extracted beam, the classical integrator is used.

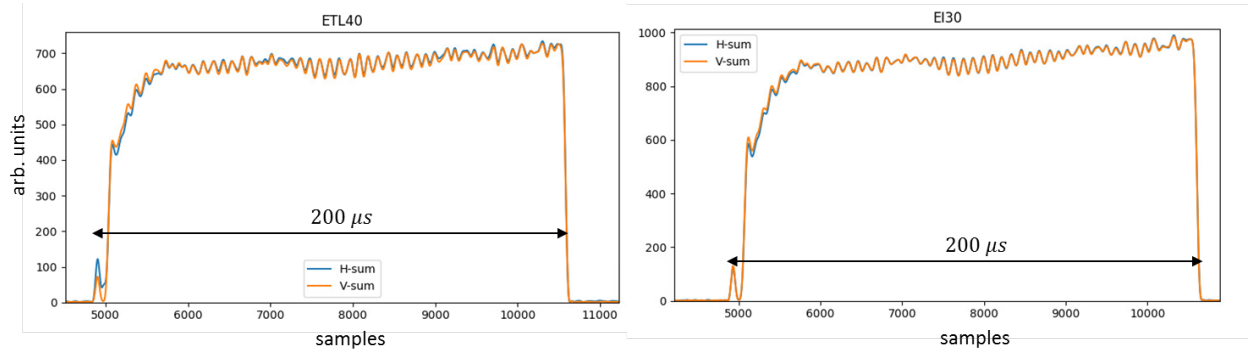

Figure 8: Horizontal and vertical ETL.BPMI40 and EI.BPMI30 sum signals sampled at 25 MS/s.

Device name	β	Plane
ER.UCV22	low	vertical
ER.UCV32	high	vertical
ER.UCH10	high	horizontal + longitudinal
ER.UCH40	low	horizontal + longitudinal

Table 2: Schottky pickup devices, energy range and measurement plane.

2.3 New Schottky acquisition

During the injection and accumulation phase, when the circulating beam is unbunched, diagnostics with the longitudinal Schottky noise is routinely used to measure the momentum spread in order to control the injection, cooling and capture efficiency. The longitudinal Schottky noise at injection ($\beta < 0.1$) is detected by a succession of short strip line pickups connected in series. There is one system per transverse plane; the horizontal one yields also longitudinal information [2]. The configuration of the complete system is described in (7). Table 2 compiles the list of pickups.

Until 2018, the Schottky data were processed based on spectrum analysers (Fig. 43 in Sec. 4.4 shows an example of the spectrum analyser Graphical User Interface (GUI)). In addition, a new system (based on VME/VFC) with a standard FESA interface was installed during the year. The system was tested and made operational, however, the readout speed was found to be too low for cycle-to-cycle usage. Consequently, the system was updated during LS2 (8) to use PCI Express, thereby increasing the readout speed by roughly a factor 50. It is now possible to read approximately 4 Gbit in a 3.2 s LEIR cycle, which is sufficient for standard Schottky monitoring applications. The corresponding FESA class has also been updated and simplified.

With the commissioning of the new system, two different applications were developed to fully exploit the functionality of the longitudinal Schottky data. On one hand a Java application, with the GUI shown in Fig. 9, allowed to control, display and take reference measurements of the beam frequency. In parallel, a Python application based on *PyQt* was

[2] A second set of strip-line pickups is installed for measuring any kind of particle velocity, but was not used operationally during run 2.

developed to monitor the average beam energy distribution from Linac 3 by analysing the beam frequency from a given cycle, MDEARLY, for which the Linac 3 ramping cavity was switched off in order to get a monoenergetic beam. This analysis allowed to monitor the beam quality from Linac 3 and spot possible problems as described in Sec. 5.12. The GUI of the Python application can be seen in Fig. 67.

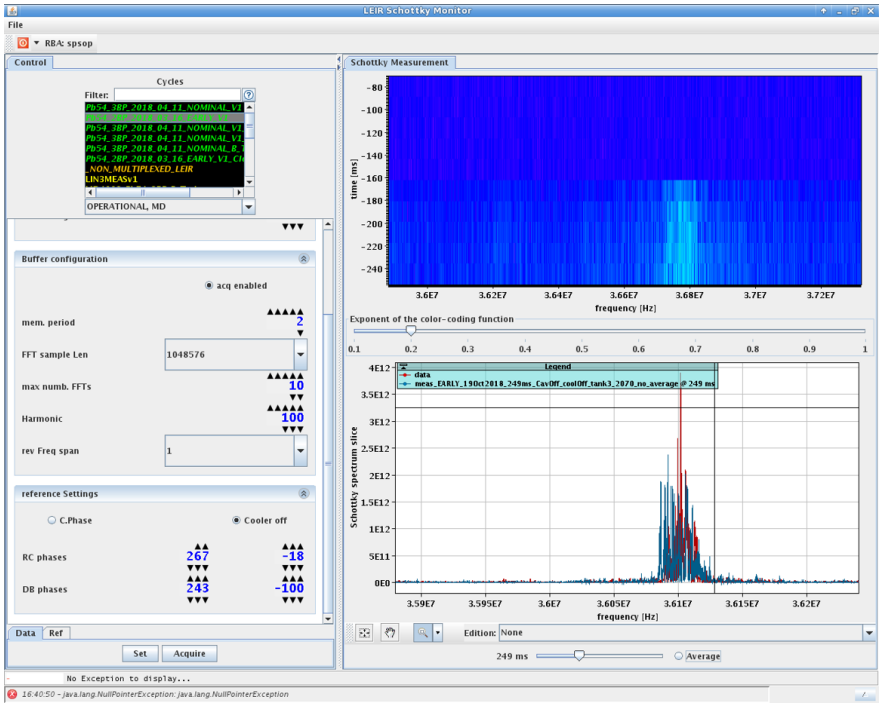

Figure 9: GUI of the Java application controlling the longitudinal Schottky measurements. The left panel shows the available cycles on which measurements can be performed, and a series of control knobs. On the right-top plot the evolution as a function of time (for a selected time window during the cycle) of the calculated beam frequency is displayed. The right-bottom plot shows the frequency distribution for a given instant in time.

2.4 New BPM ring system

The new orbit system was implemented since end of 2017 and made operational from July 2018. The previous system was modified in a way that pickups and head amplifiers could remain unchanged, but distribution amplifiers, acquisition system, firmware and software were updated. One pickup (the UEH14) was found shorted and it was repaired during LS2. Additional tests demonstrated that a guard-voltage is needed on the pickups, which is therefore planned for installation during LS2. The new installed system brought several advantages and added functionalities: among the advantages, a clear improvement in the stability of the orbit readings, as illustrated in Fig. 10. The new functionality covers the trajectory acquisition that provides turn-by-turn data and, eventually, first turn data.

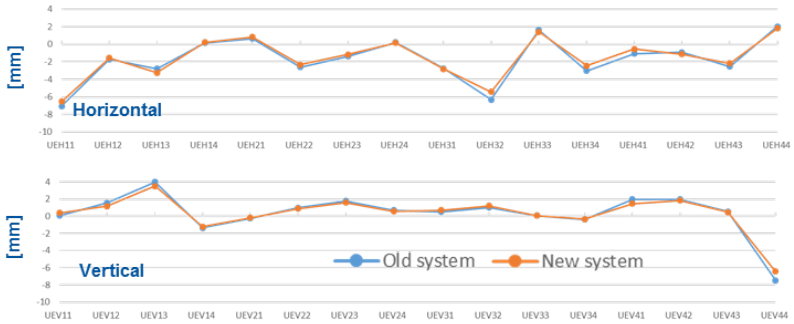

(a)

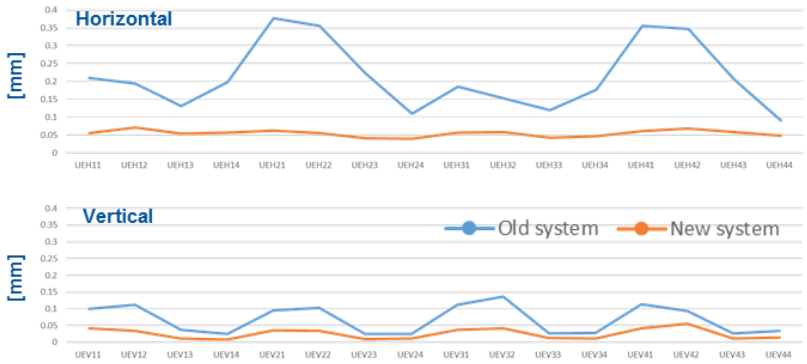

(b)

Figure 10: New orbit system. (a) average orbit measurement for the new system (orange) compared to the old system (blue), (b) standard deviation of the orbit measurement for the new system (orange) compared to the old system (blue). A clear improvement in the horizontal measurement is visible with the new system.

2.4.1 Turn-by-turn and first-turn acquisition

In 2018 the orbit system was extended with turn-by-turn functionality and initial testing of the system (also known as the *trajectory system*) was carried out, giving the position of the bunched beam (9). The hardware provides 69 samples per turn following the RF frequency. The FESA class performs bunch detection and computes the position. The readout time was found to be too long and is being evaluated/optimized during LS2. Figure 11 shows the application developed by BE/BI to visualise the turn-by-turn data available from the BPM system. With the present system, it was already possible to perform preliminary optics measurements summarized in (10).

The system is also capable of operating in so called *first-turn mode* in order to smooth the setup of the machine at the very beginning of the beam commissioning (11). First-turn traces were obtained by sequentially closing the LEIR vacuum valves, and were found to be significantly distorted/masked by the beam hitting the orbit pickups. This observation supports the need for the previously mentioned guard-voltage system. Few good shots for the horizontal planes are shown as an example in Fig. 12: a "normal" signal should look like the one in the bottom of the picture, i.e. a derivative of the injected Linac 3 square pulse. This is due to the fact that the beam can be modelled as a source coupled capacitively to the

Figure 11: LEIR BPM GUI to visualise turn-by-turn measurements from the orbit system.

pickup plate which is in parallel to the head amplifier input resistance. This is equivalent to an RC circuit which high-pass filters the frequency content of the injected pulse and results in the removal of the DC component. For low frequencies with respect to the cut-off frequency, the output signal corresponds to the derivative of the input signal.

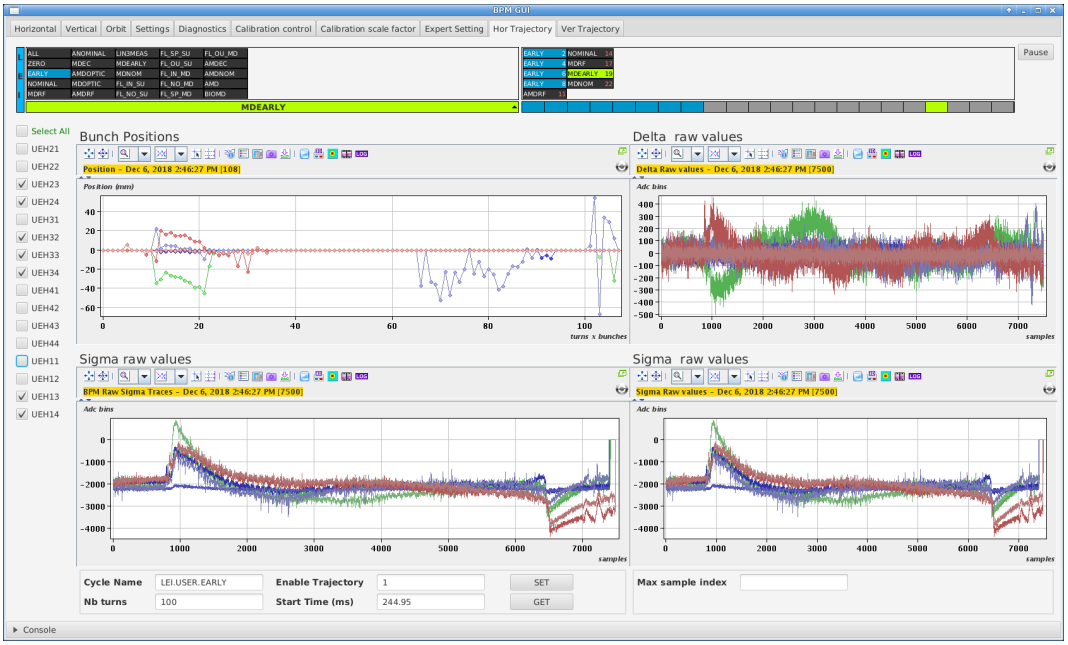

Figure 12: LEIR BPM GUI to visualise first turn measurements from the orbit system. The measurements shown in the GUI correspond to the horizontal plane.

2.5 New beam dump system

The LEIR dump is a new external dump designed to safely dispose of the ion beams extracted from the LEIR machine when the beam is not requested by the PS. Up to 2018, there was no dump installed, therefore the beams accumulated in LEIR not requested by the downstream machines were lost on the PS injection septum, or inside the LEIR machine itself. The higher intensity of the LIU ions beam requires particles to be disposed of cleanly and safely, so a new dedicated dump was designed for this purpose. The new dump for the extracted beam is installed in the PS switchyard, at the exit of the ETL.BHN10 magnet, near the end of the bi-directional LEIR transfer line ETL as shown in Fig. 13.

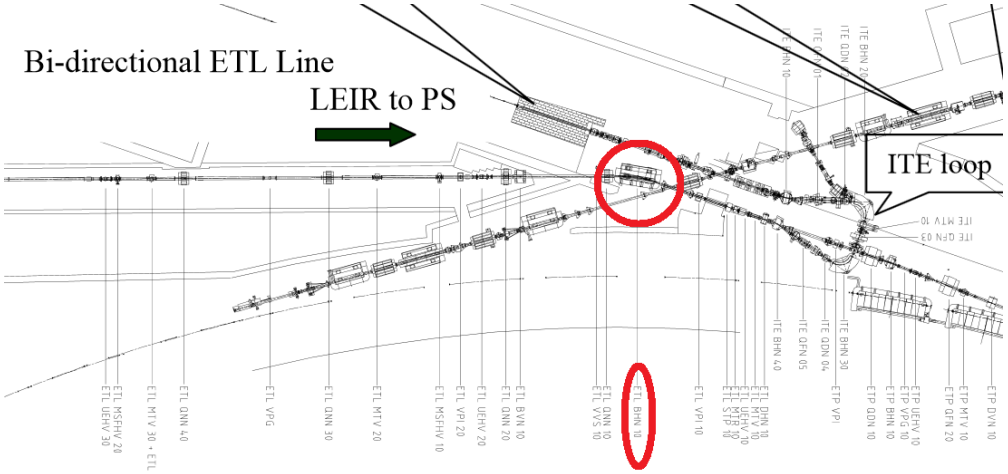

Figure 13: Linac 3 to LEIR to PS transfer line showing the position of the new beam dump where the ETL.BHN10 magnet is.

2.5.1 Hardware

The dump is composed of a solid cylinder (where the beam impacts) with 11 fins made of the same aluminium alloy EN-AW 6082 T6 (12; 13). The number of fins was optimized in order to have the best compromise in terms of functionality and heat dissipation. An extension of an aluminium tube was inserted in order to house the groove for the ring that connects the dump to the flange. This is necessary to maintain the retaining ring away from the points with higher temperatures. The device was milled and turned out of a single block. The layout is shown in Fig. 14 and the vacuum pipe layout is shown in Fig. 15.

The dump was designed for continuous beam operation of 24h/day, 7 days a week. The device is directly supported by the vacuum chamber; no additional supports are used. The volume occupied by the dump is about $8 \cdot 10^{-4}$ m^3.

2.5.2 Controls implementation

ETL.BHN10 dipole magnet is pulsed during injection and extraction. Depending on destination during extraction, two different deflection angles are needed, 0.33 rad to send the beam to PS or 0.16 rad to send the beam to the dump as shown in Fig. 16. The current sent to the

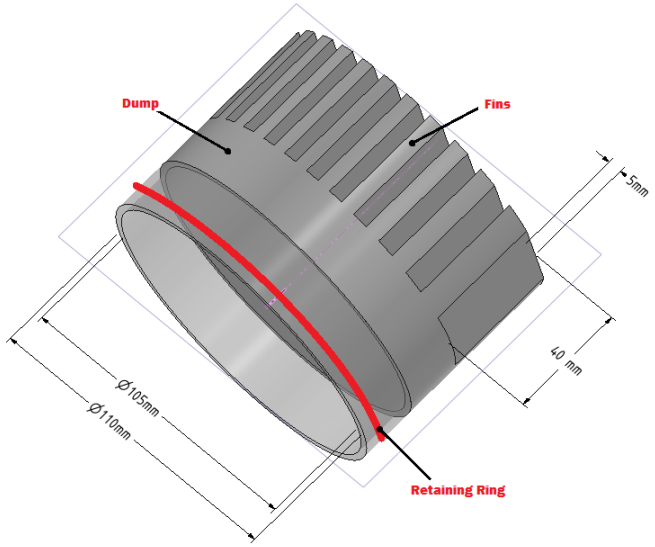

Figure 14: LEIR dump conceptual design.

Figure 15: Layout of the new vacuum chamber.

magnet is programmed according to the deflection angles and is implemented in two different functions as shown in Fig. 17, where the blue curve is for the dump destination, and the red curve for the PS destination. Both curves share the same injection current. The deflection angle to PS (K_to_ps) is generated via the BRHO parameter in the beam process type DISCRETE_LEIREjection_Pb20854 and assigned to the parameter ETL.GSBHN10/KICK. The deflection value to the dump (K_to_dump) is calculated according to Eq. (1) and assigned to the parameter ETL.GSBHN10-DUMP/KICK.

$$K\_to\_dump = K\_to\_ps \frac{rho\_to\_ps}{rho\_to\_dump} \tag{1}$$

The parameters rho_to_ps and rho_to_dump are hard coded in the make rule with values 6580 mm and 13608 mm, respectively.

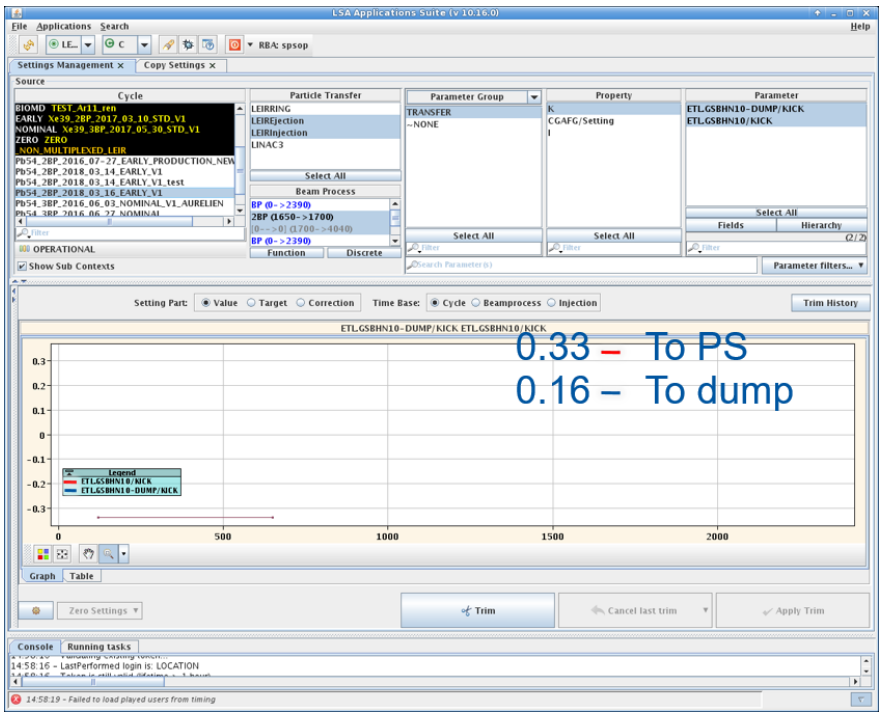

Figure 16: Deflection angles in radians for the ETL.BHN10 when destination is PS (red) and the dump (blue). The value at injection, same for both configurations, is also visible at the bottom-left. The horizontal coordinate is the cycle time in ms.

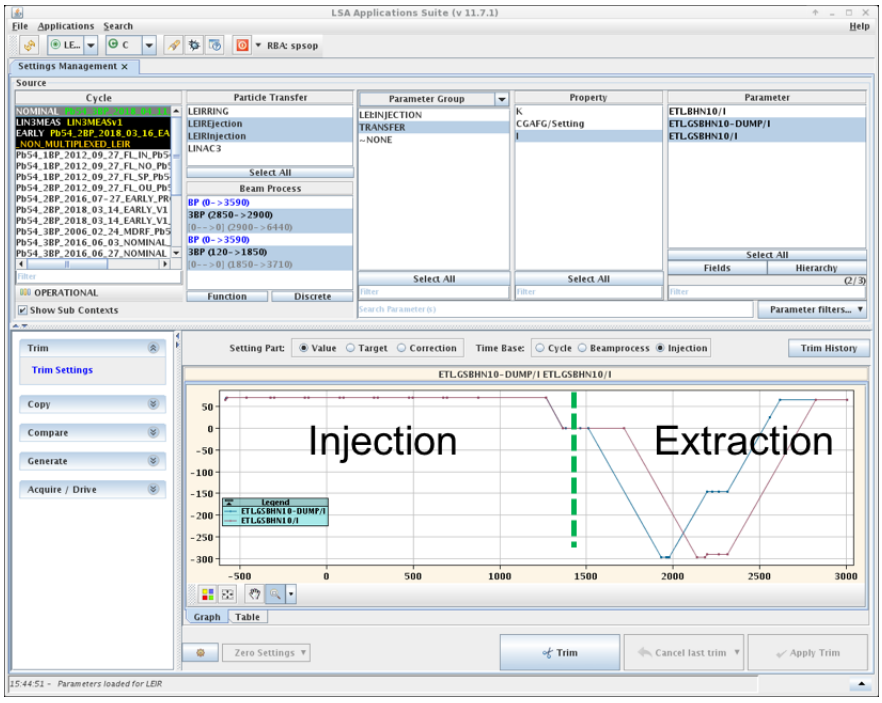

Figure 17: Current functions in amperes for the ETL.BHN10 when destination is PS (red) and the dump (blue). The horizontal coordinate is the cycle time in ms.

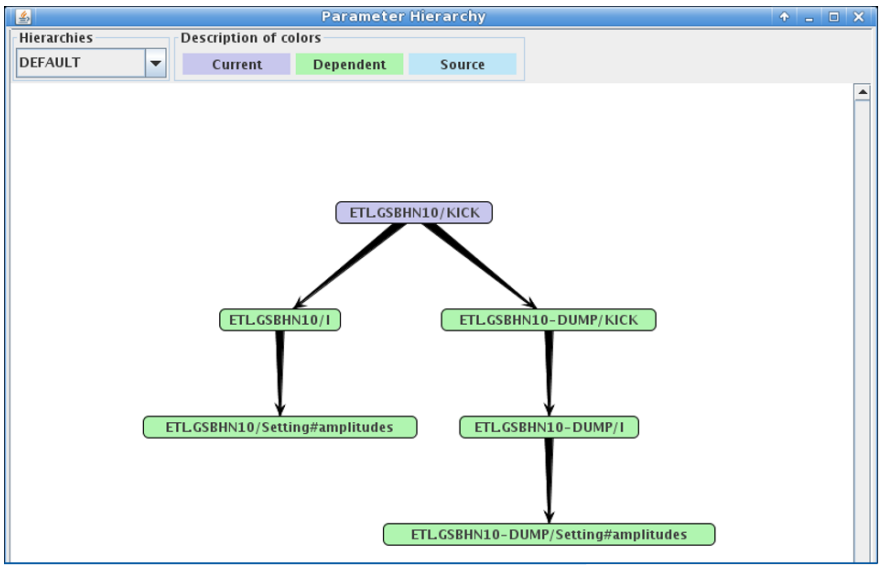

Figure 18: LSA make rule implementation for the calculation of the current values to be sent to the hardware.

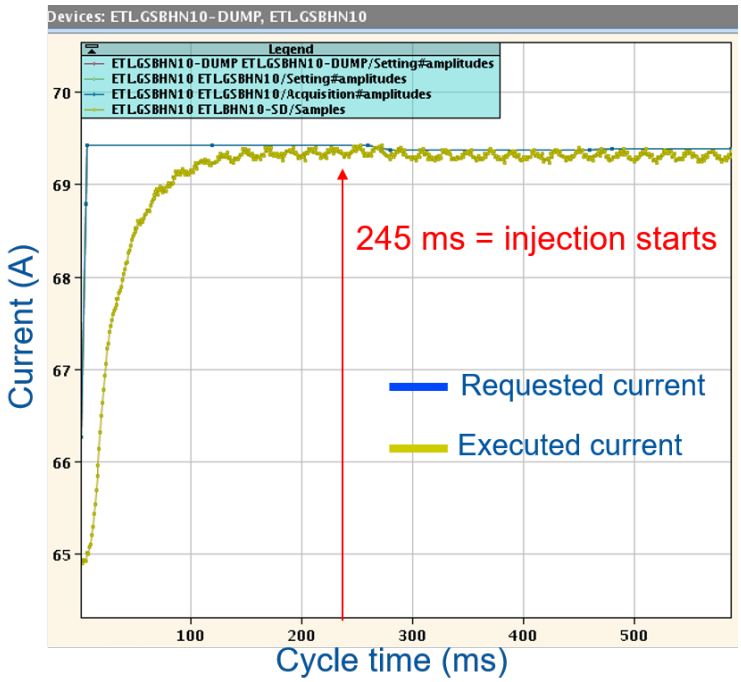

Figure 19: Current functions for the ETL.BHN10 zoomed around the injection time. By the time the first injection takes place, the current is well stabilised at the required value.

Via LSA trim editor the operator can modify the value of ETL.GSBHN10/KICK to optimize the injection into LEIR. The only parameter that should be trimmed is ETL.GSBHN10/KICK because the make rule automatically computes the corresponding ETL.GSBHN10-DUMP/KICK value (which should never be trimmed). From the KICK value the make rule calculates the currents (I) and the Setting#amplitudes to be sent to

the CGAFG devices, the ETL.GSBHN10 and the ETL.GSBHN10-DUMP, as schematically represented in Fig. 18. The CGAFG (deployed on CVORB hardware) are the function generators for the power converters. The settings that will be loaded into the hardware (ETL.GSBHN10/Setting#amplitudes or ETL.GSBHN10-DUMP/Setting#amplitudes) will depend on the destination. The destination is encoded into the payload of the field TO_PS of the timing event CTIM called EX.FCY500-CT, which is a 500 ms forewarning event, i.e. arrives 500 ms before the cycle starts. If TO_PS is true, the destination is PS and the ETL.GSBHN10/Setting#amplitudes is downloaded into the CVORB hardware, if it is false, the destination is the dump and ETL.GSBHN10-DUMP/Setting#amplitudes is downloaded instead. Upon reception of the timing event EX.SCY-CT (start of cycle) the EX.SGFAS-POW3 event is triggered and instructs the CVORB hardware to start playing the downloaded function such that the power converter of the ETL.BHN10 magnet will provide the appropriate current according to destination.

To be noted that the destination within the timing event EX.FCY500-CT is not at all dynamic, it is fixed by the programmed supercycle in the cycle management system. For the moment, LEIR does not benefit from the dynamic destination implementation.

During the development of the ETL.GSBHN10 function for the NOMINAL cycle, it was observed that if the ETL.GSBHN10/I or ETL.GSBHN10-DUMP/I were starting and finishing at 0 A, when the next cycle arrived the power converter did not have time enough to reach the current at the required injection value, usually around 70 A. Important current fluctuations and sensitivity to temperature drifts at the time of the first injection at 245 ms were systematically observed due to current overshooting (see also Sec. 6.3). The make rule was modified such that the current function always finishes at 65 A at the end of the cycle, and therefore, also starts at 65 A at the start of cycle. Thus, when the next cycle starts, the power converter is already at 65 A and has enough time to reach the required injection current well before the first injection arrives as illustrated in Fig. 19.

2.5.3 Measured temperatures

The average beam power from LEIR is quite low, and the beam dump was not expected to suffer large temperature rises. Figure 20 shows how the temperature of the dump rises by less than 1 °C following an extended intervention in Linac 3, followed by the beam restart.

The thermal calculations for the design of the beam dump lead to a maximum steady state external temperature rise of 14 °C (14). Several factors could reduce the expected average beam power relative to the value used for the thermal analysis (a factor 2 from peak intensity, factor 2 as only half cycles are of NOMINAL type, factor 2 as only half of the cycles go to the dump, factor 1.5 as LEIR NOMINAL-type cycles are 3.6 s long with respect to the 2.4 s duration of EARLY-type cycles) - all together the measured temperature rise observed at that time of 1°C is therefore consistent.

2.6 New magnetic sensors for B field measurement

Contrary to most other B-train systems in operation at CERN, the LEIR machine does not have a dedicated reference main bending magnet for the field measurement (the other exception is AD, where the measurement is not required). As a result, the sensors can only

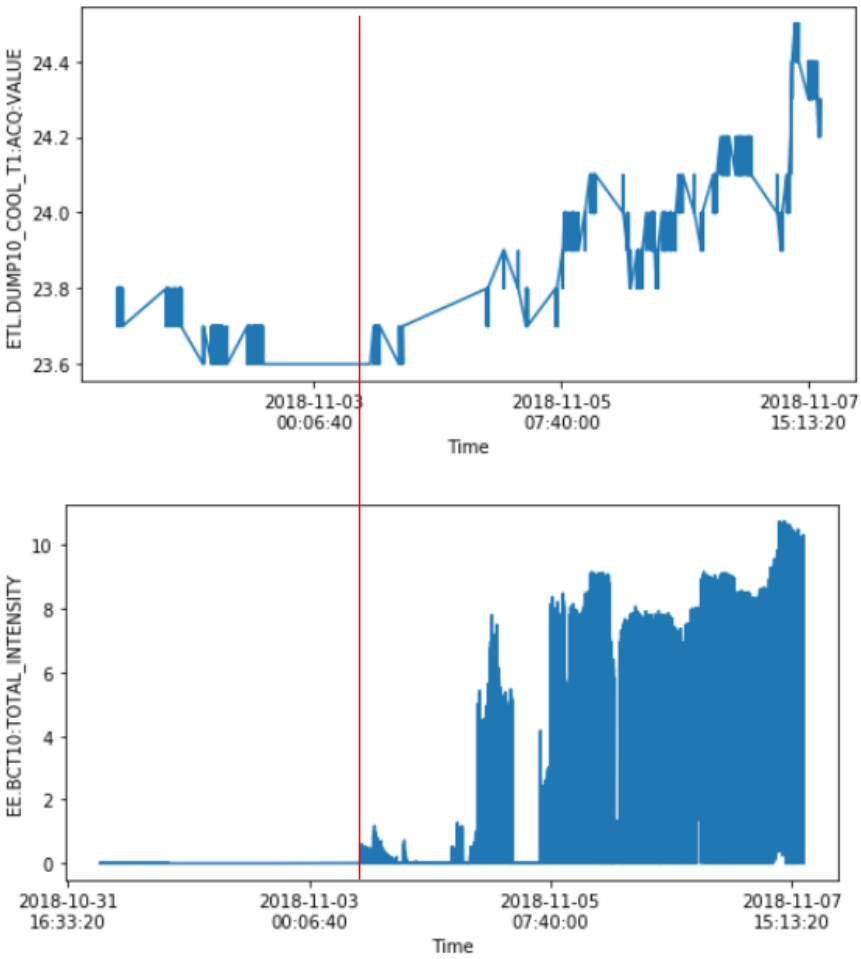

Figure 20: Top: dump temperature (measured on the external surface); bottom: beam intensity extracted from LEIR. Plots are shown as beam is restarted following a Linac 3 stop (the red vertical line indicates when the first beam is ejected from LEIR).

be installed in the ring dipoles. The legacy system was based on one operational and one spare induction coil installed in the BHN30 and BHN20 dipoles, respectively, tightly wedged between the vacuum chamber and the bottom magnet pole. No field marker was included to provide the integration constant for the coil voltage, which made the legacy B-train blind to magnetic hysteresis effects. The coil inside BHN20 developed an electrical fault shortly after installation, which was never repaired since that would have required opening up the whole magnet.

Therefore, after a detailed study involving operation, vacuum, handling and magnet teams, it was decided to include a new set of coils and field markers in the new system, which are located in the accessible fringe field region of the magnets. This choice considerably lowers the cost of installation and ensures easy maintainability of the system in the long term, at the risk of a slight degradation of measurement accuracy due to non-linear effects.

Two identical assemblies, including one induction coil and two field markers have been installed in BHN20 and BHN30 on the mid-plane of the gap, in the outer region just outside the vacuum chamber and the surrounding bake-out insulation, as shown in Fig. 21. Only one

of the field markers has been used for operation, the other being a hot spare. The position of the sensors was optimized on the basis of the results of a DC Opera finite element (FE) simulation, shown in Fig. 22. They have been mounted at a radial distance with respect to the closed orbit of $x \approx 200$ mm, where the ratio between the field at extraction and injection, (Fig. 22b) is approximately equal to the ratio at $x = 0$ mm, which is taken as an indication of minimal impact of saturation (which is otherwise clearly visible at $x \approx 130$ mm). In this region the radial gradient is, in relative terms, about 1% mm^{-1} at all field levels.

The induction coils are 102 mm long, have an effective area of 0.60367 m^2 and are positioned tangentially to the ring circumference. At both ends of each coil there is a ferromagnetic resonance (FMR) field marker, based on a ø3 mm YIG sample in a 3 GHz GCPW resonator (15). This kind of sensors, similar to those that have been in operation at the PS for the last few years, are the only choice that can guarantee a repeatability of at least 10^{-3} despite the relatively high field gradient. The nominal working point of the markers is 106 mT, with a gradient of 1.2 T/m. According to FE calculations, this corresponds to 252 mT at the closed orbit i.e. about 20 mT lower than the nominal injection field for the beam used in the tests, i.e. 272.1 mT. These settings ensure that the FMR resonance is crossed at a dB/dt that is adequate to generate a strong detectable signal, while at the same time being as temporally close as possible to beam injection, when the highest possible field measurement accuracy is required.

Due to their external placement, the magnetic sensors are exposed to the temperature fluctuations in the ring hall, which is in a surface building without air conditioning. The observed fluctuations can be very large, up to 15°C in a single day and 15°C from winter to summer. For this reason, a temperature regulation system (shown in Fig. 21b and Fig. 21c) was installed to keep the assembly at 35 ± 0.1°C, which based on calibration tests should ensure marked field errors within ± 4 μT.

2.7 $B\rho$ generation in LSA

The LSA generation of the Bρ function and, therefore, the beam momentum in LEIR, is performed integrating the time derivative of the beam rigidity, $\dot{B\rho}$, along the cycle. The $\dot{B\rho}$ function, therefore, needs to be obtained first. For this purpose an algorithm has been implemented in python, which is explained in the following subsections (16; 17).

2.7.1 $\dot{B\rho}$ calculation

The $\dot{B\rho}$ is calculated for a few points in the cycle, which depend on the particle type:

1. t = 0.02 s and 0.12 s, which define the ramp function from the pre-injection plateau to the injection plateau. This depends on the kinetic energy per nucleon and the particle type coming from Linac 3. The $\dot{B\rho}$ is the same at those two cycle times.

2. t = 0.75 s, which defines the start of the ramp function towards flat top. The beam rigidity at flat top is fixed in LEIR regardless the particle type.

3. t = 2.2 s to guarantee that the integral of the $\dot{B\rho}$ function along the cycle is 0.

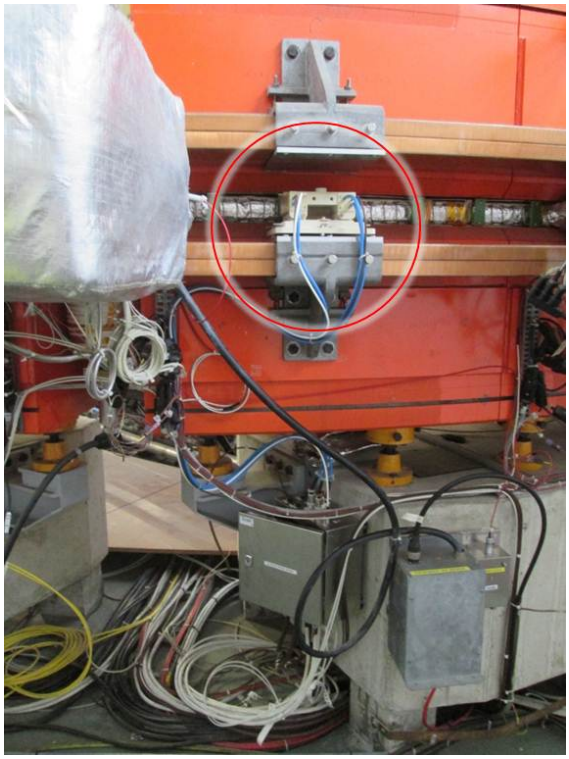

(a)

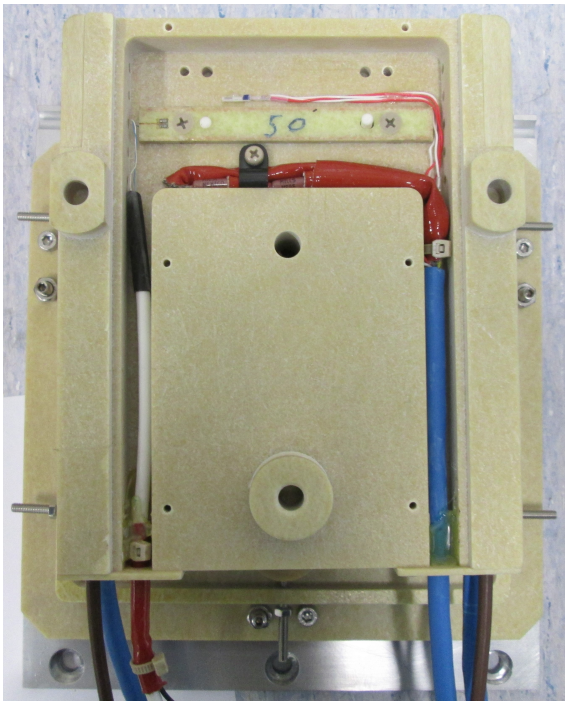

(b)

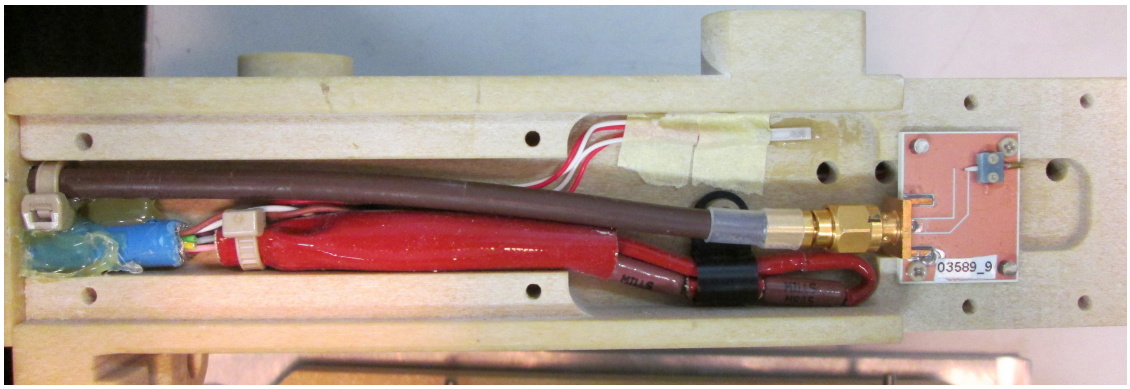

(c)

Figure 21: LEIR B-train sensors.(a) The new B-train sensors installed on the BHN20 (spare) and BHN30 (operational) magnets. It includes the sensors support placed on the side of the vacuum pipe and the front-end RF equipment box placed below the magnet. (b) The search coil on top of the sensor support. (c) FMR markers on each side of the sensor support. Close to each sensor, a heating resistor and a PT100 temperature sensor are installed for the temperature regulation.

The rest of the points are fixed and they are the same for any LEIR cycle. On top of this, other conditions are imposed:

- The beam rigidity at the beginning of the cycle is set to $(B\rho)_0 = 0.6$ Tm to cope with hysteresis issues.
- Such that two consecutive cycles have smooth transition, the following condition is

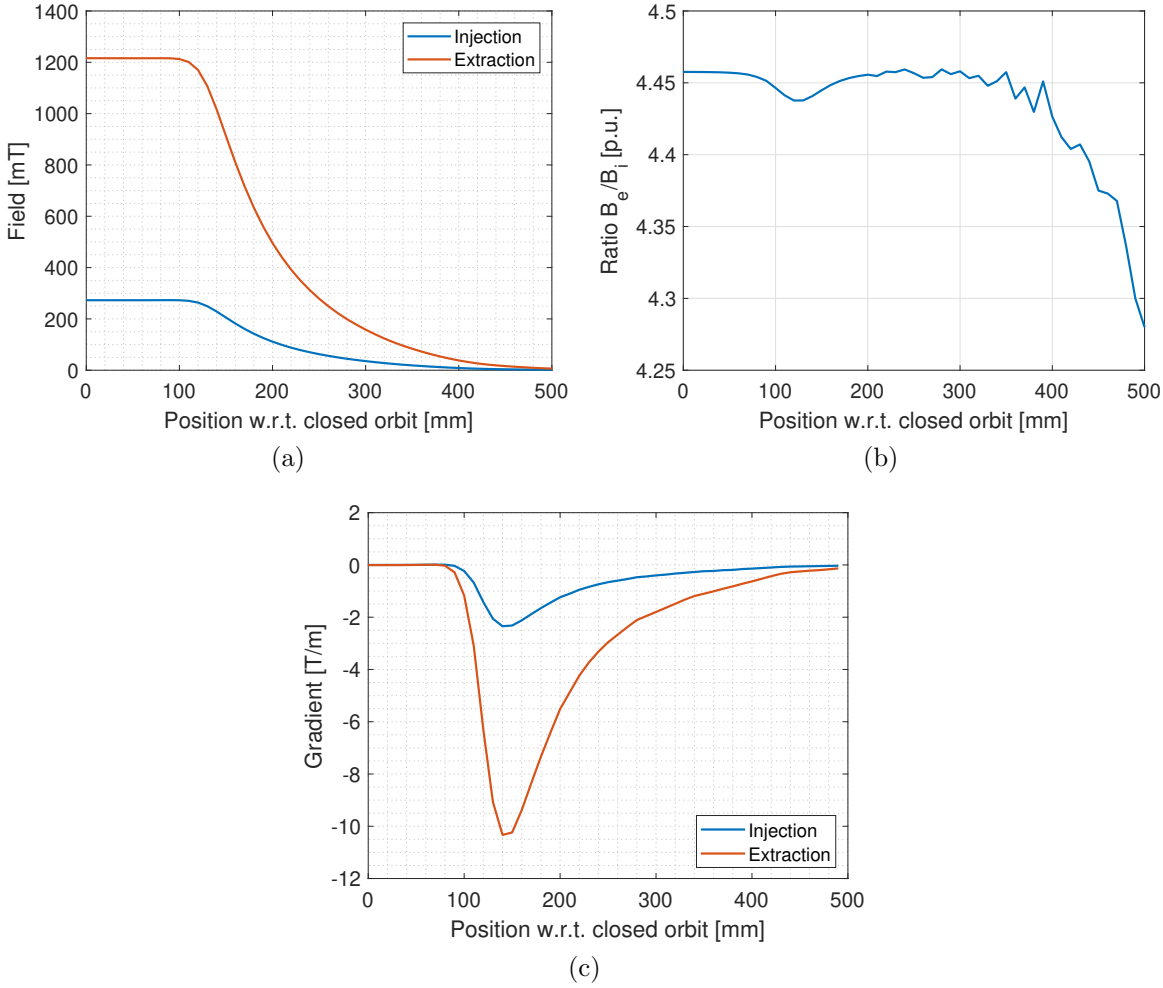

Figure 22: FE simulation of LEIR main dipole simulation. (a) Vertical field vs. outwards radial distance from the beam closed orbit, at injection (blue curve) and at extraction (red curve). (b) Ratio between the field at extraction B_e and injection B_i. (c) Radial gradient vs. outwards radial distance from the beam closed orbit, at injection (blue curve) and at extraction (red curve).

imposed:

$$(\dot{B\rho})_0 = (\dot{B\rho})_{n-1} = 0\ Tm/s \tag{2}$$

where $t_0 = 0$ s is the start of cycle, and t_{n-1} is the last point of the cycle [3]. Therefore, $(B\rho)_0 = (B\rho)_{n-1} = 0.6$ Tm.

- To ensure that the function sent to the main power converter starts and ends at the same magnetic field, the integral of $\dot{B\rho}$ over the whole function must vanish. To this end, $(\dot{B\rho})_{n-2}$ (at t = 2.2 s (+ delay) in Tab. 3) is not programmed, but computed to ensure above condition.

- The maximum requested voltage should be within ±500 V.

[3] In the LEIR case the total number of points has been fixed to 18, therefore, n = 18 and n-1 = 17 is actually the last point of the cycle in Tab. 3

	time (s)	$\dot{B\rho}$ **(Tm/s)**	$B\rho$ **(Tm)**
0	0	0.0	0.6
1	0.02	$(\dot{B\rho})_1$	
2	0.12	$(\dot{B\rho})_2$	
3	0.14	0.0	$(B\rho)_{inj}$
4	0.65 + delay	0.0	
5	0.75 + delay	$(\dot{B\rho})_5$	
6	1.3 + delay	5.417	
7	1.55 + delay	5.32	
8	1.65 + delay	-0.6	
9	1.66 + delay	-0.35	4.836
10	1.675 + delay	-0.2	
11	1.692 + delay	-0.1	
12	1.7 + delay	-0.069	
13	1.71 + delay	-0.03	
14	1.8 + delay	-7.7	
15	2.2 + delay	$(\dot{B\rho})_{15}$	0.0
16	2.29 + delay	-6	
17	2.4 + delay	0.0	0.6

Table 3: Discrete times for which the time derivative of the magnetic field is predefined. The *delay* parameter is 0 s for the EARLY cycle and 1.2 s for the NOMINAL cycle to shift the beginning of the ramp at the end of the injection plateau. Predefined values for the beam rigidity are given. The $(B\rho)_{inj}$ is as well predefined, but depends on the particle type and the kinetic energy from Linac 3.

- The maximum of the ratio $(\dot{B\rho})/B\rho$ should be a compromise between the reduction of induced eddy currents and the energy increase against space charge effects.

Table 3 compiles the $(\dot{B\rho})$ fixed values and indicates the values that have to be calculated by the algorithm, i.e. $(\dot{B\rho})_1$, $(\dot{B\rho})_2$, $(\dot{B\rho})_5$ and $(\dot{B\rho})_{15}$. The table also shows the imposed $(B\rho)$ values. The *delay* parameter is 0 s for the EARLY cycle and 1.2 s for the NOMINAL cycle to shift the beginning of the ramp after the injection plateau.

2.7.2 Calculation of $(\dot{B\rho})$ at 0.02 s and 0.12 s

$(B\rho)_1$=$(B\rho)_2$ are determined by the $B\rho$ at t_0 and at the injection plateau t_3, which in turn is defined according to the particle type and the kinetic energy per nucleon from the Linac 3, 4.2 MeV/nucleon. For $^{208}Pb^{54+}$ the injection $B\rho$ is 1.127 Tm. The beam rigidity $(\dot{B\rho})_k$ corresponding to the discrete time t_k, can be calculated as follows:

$$(B\rho)_k = (B\rho)_0 + \sum_{i=1}^{k}(t_i - t_{i-1})\frac{1}{2}((\dot{B\rho})_i + (\dot{B\rho})_{i-1}), \tag{3}$$

with $(B\rho)_0 = 0.6$ Tm, $(B\rho)_3$ corresponds to the injection rigidity $(B\rho)_{inj}$, $(\dot{B\rho})_{0,3} = 0$, $(\dot{B\rho})_{1,2}$ are values to be found, and $(t_0,\ t_1,\ t_2,\ t_3) = (0,\ 0.02,\ 0.12,\ 0.14)$ s, as shown in Tab. 3. Replacing all those values in the Eq. 3 we get

$$(\dot{B\rho})_1 = (\dot{B\rho})_2 = \frac{2 \cdot ((B\rho)_3 - (B\rho)_0)}{(t_2 + t_3) - (t_0 + t_1)} = 4.417 \text{ Tm/s}, \tag{4}$$

for $^{208}\text{Pb}^{54+}$case.

2.7.3 Calculation of $(\dot{B\rho})$ at 0.75 s

To calculate $(\dot{B\rho})$ at 0.75 s, corresponding to $(\dot{B\rho})_5$ in Tab. 3, Eq. 3 is again used for $k = 9$, which corresponds to the flat top value fixed in LEIR to $B\rho = 4.836$ Tm regardless the particle type. If Eq. 3 is developed up to k=9, $(\dot{B\rho})_5$ can be expressed as a function of known values as

$$(\dot{B\rho})_5 = \frac{-(-2((B\rho)_9 - (B\rho)_0) + A + B + (t_5 - t_4)(\dot{B\rho})_4 + (t_6 - t_5)(\dot{B\rho})_6)}{(t_6 - t_4)}, \tag{5}$$

where A and B are, respectively,

$$A = \sum_{i=1}^{4} (t_i - t_{i-1})((\dot{B\rho})_i + (\dot{B\rho})_{i-1}), \tag{6}$$

$$B = \sum_{i=7}^{9} (t_i - t_{i-1})((\dot{B\rho})_i + (\dot{B\rho})_{i-1}). \tag{7}$$

Introducing the known values of Tab. 3 into the equations above, the value of $(\dot{B\rho})_5$ for $^{208}\text{Pb}^{54+}$ is

$$(\dot{B\rho})_5 = 1.963 \text{ Tm/s}. \tag{8}$$

2.7.4 Calculation of $(\dot{B\rho})$ at 2.2 s

As explained above, $(\dot{B\rho})_{15}$ is not programmed, but computed to ensure that the function sent to the main power converter starts and ends at the same magnetic field, making the integral of $\dot{B\rho}$ over the whole function zero. Once more Eq. 3 is used to compute $(\dot{B\rho})_{15}$. In this case, $(B\rho)_k = (B\rho)_{17} = (B\rho)_0 = 0.6$ Tm, and Eq. 3 reduces to

$$0 = \int dt(\dot{B\rho}) = \frac{1}{2} \sum_{i=1}^{n-2} (t_{i+1} - t_{i-1})(\dot{B\rho})_i, \tag{9}$$

and the expression to calculate $(\dot{B\rho})_{15}$ is

$$(\dot{B\rho})_{15} = \frac{-(A + B + (t_{15} - t_{14})(\dot{B\rho})_{14} + (t_{16} - t_{15})(\dot{B\rho})_{16})}{(t_{16} - t_{14})} = -7.205 \text{ Tm/s}, \tag{10}$$

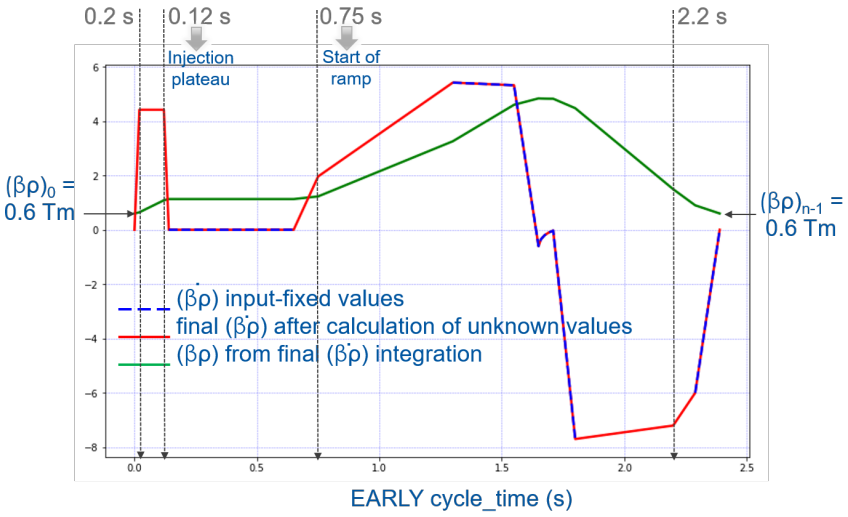

Figure 23: Dotted-blue line: $\dot{B\rho}$ pre-defined input values; red line: $\dot{B\rho}$ as a result of the calculation of the missing values; green-line: $B\rho$ final function after integration of $\dot{B\rho}$.

where

$$A = \sum_{i=1}^{14}(t_i - t_{i-1})((\dot{B\rho})_i + (\dot{B\rho})_{i-1}), \tag{11}$$

$$B = (t_{17} - t_{16})((\dot{B\rho})_{17} + (\dot{B\rho})_{16}). \tag{12}$$

Figure 23 shows in dotted-blue lines the initially fixed $\dot{B\rho}$ values which are independent of the LEIR cycle. The red curve shows the $\dot{B\rho}$ function after calculation of the missing values. Finally, the green curve shows the $B\rho$ function obtained from the $\dot{B\rho}$ integration.

2.7.5 Voltage across BHN dipole circuit

One of the requirements to obtain a valid $\dot{B\rho}$ function is to check that the required main dipole circuit (BHN) voltage is between the limit of ±500 V. For this, the algorithm calculates the voltage function V using the equation

$$V = R_{BHN}\,[I_{BHN-offset} + (I \rightarrow B\rho)_{calibration} \cdot\ B\rho] + L_{BHN} \cdot\ (I \rightarrow B\rho)_{calibration} \cdot\ (\dot{B\rho}), \tag{13}$$

where $R_{BHN} = 0.030\ \Omega$, $L_{BHN} = 0.1\ H$ and $I_{BHN-offset} = 2.5$ A. The calibration constant is defined as

$$(I \rightarrow B\rho)_{calibration} = \frac{\frac{707\text{ A} + 702\text{ A}}{2}}{0.2468\text{ T} \cdot 4.20\text{ m}}, \tag{14}$$

and it is computed taking into account that two different fields, and therefore currents, are achieved if walking through the hysteresis curve from below (707 A) or above (702 A). Figure 24 shows the derived voltage from the calculated $\dot{B\rho}$ and $B\rho$ functions for $^{208}Pb^{54+}$after applying Eq. 13.

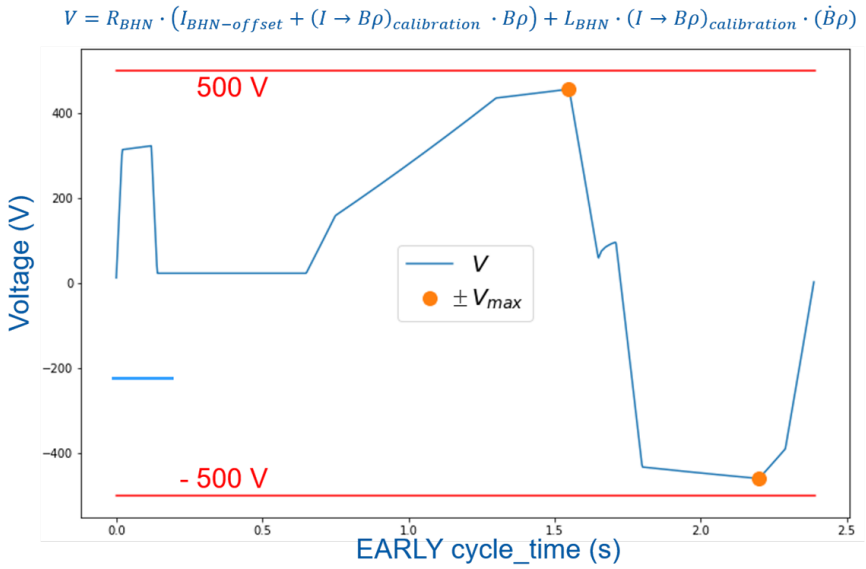

Figure 24: Derived voltage from the calculated $\dot{B\rho}$ and $B\rho$ functions after applying Eq. 13.

2.7.6 LSA generation

The final step once the $\dot{B\rho}$ is calculated is to introduced the discrete points of Tab. 3 into the beam process type table as indicated in Fig. 25. This table will be used by LSA to generate the $B\rho$ function, using as integration constant the $(B\rho)_0$ value, also explicitly indicated in the table.

2.8 Injection septa high level parameters in LSA

The high injection efficiencies achieved in LEIR with multi-turn injection in the three dimensions are possible thanks to the combination of a magnetic septum, ER.SMH11, providing a large deflection of 175 mrad and installed sufficiently far upstream in order not to reduce the available aperture, followed further downstream by a very thin (blade with effective thickness of a few tenths of a mm) inclined electrostatic septum ER.SEH10. Up to 2018, the control of the deflection angles of both septa were done by directly trimming the low level parameters current and voltage. In 2018 new high level parameters were introduced in LSA to steer the devices trimming the deflection angles and not any more the low level parameters.

2.8.1 Electrostatic septum ER.SEH10

A detailed description of the device can be found in (5). The ER.SEH10 is rotated 30° in the XY-plane, so the device applies, effectively, horizontal and vertical deflection angles because the electric field E has two components (E_x, E_y) as shown in Fig. 26. The horizontal bending angle, α_x, given by the horizontal electric field component E_x, has been chosen as the LSA high level parameter to be trimmed (logical.ER.SEH10/KICK (rad)) because it is the angle defined in the MAD-X optics file for the transfer line from Linac 3 to LEIR. Therefore, at generation level, LSA takes the value of the angle directly from the optics. In the MAD-X element file the septum is defined as

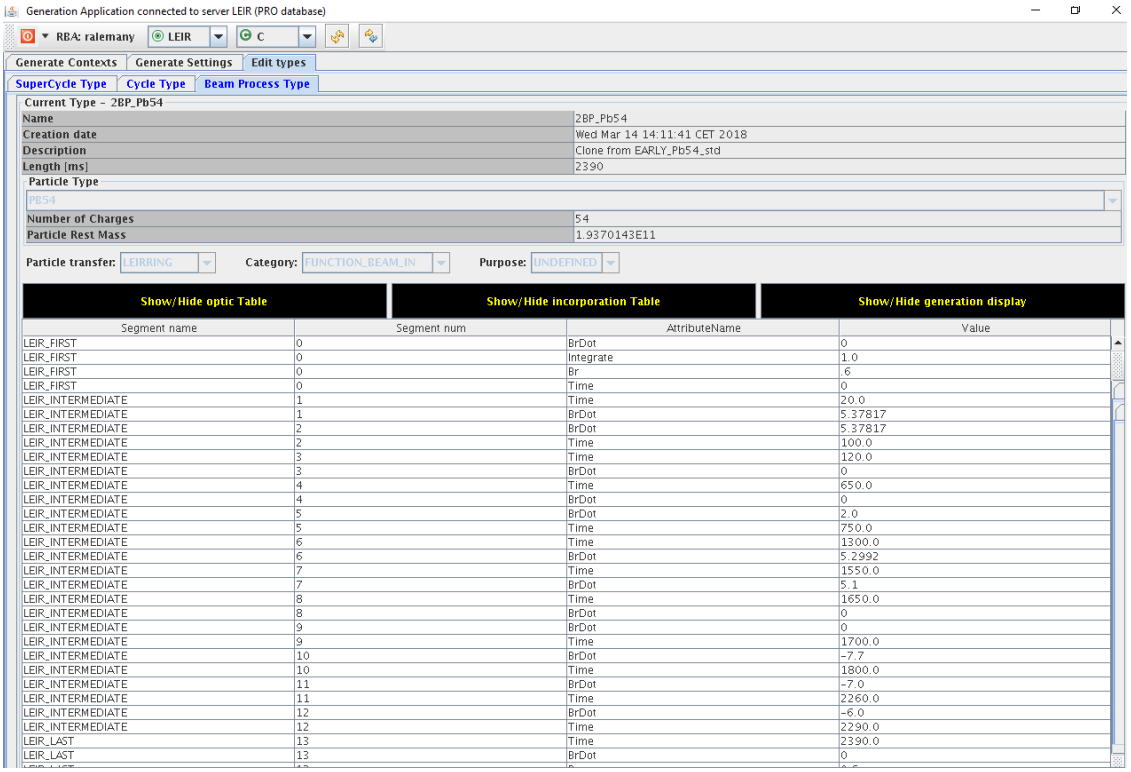

Figure 25: LSA generation table to be filled up with the calculated $\dot{B}\rho$ values.

$$
\begin{aligned}
&LERSE = 0.720; \text{(Electrostatic septum cathode length in m)}\\
&ER.SEF : SBEND;\\
&L = LERSE \cdot \frac{DERSEF}{\sin(DERSEF - IERSE) + \sin(IERSE)};\\
&ANGLE = DERSEF;
\end{aligned}
$$

where $DERSEF = 0.025$ rad, corresponds to the LSA high level parameter α_x and it is defined in the MAD-X strength file together with the definition of the nominal cathode inclination in the XZ-plane $IERSE = 0.006$ rad (called *angle* in the XZ septum view of Fig. 26). Applying the formula above, the cathode effective length is $L = 0.72003$ m. This value has been introduced in the LSA database and it is used in Eq. 15 as l_{eff}.

On top of this, the gap between the cathode and the septum foil, the position of the foil with respect to the circulating beam and the XZ angle of the septum with respect to the circulating beam orbit along the z direction (IERSE in MAD-X), can also be trimmed. Those parameters are depicted in Fig. 26 and the corresponding LSA parameters that can be trimmed via the trim editor can be seen in Fig. 27. Table 4 compiles the nominal values for the parameters listed above.

The parameters α_x and gap define the septum voltage according to

$$V = \frac{p_{LSA}^2 \cdot Q \cdot gap \cdot \alpha_x}{e \cdot \gamma_{rel} \cdot m_0 \cdot l_{eff} \cdot \cos 30^\circ}, \tag{15}$$

gap	40 mm
position	55 mm
angle	4 mrad

Table 4: Additional trimmable electrostatic septum parameters together with their default values in LSA.

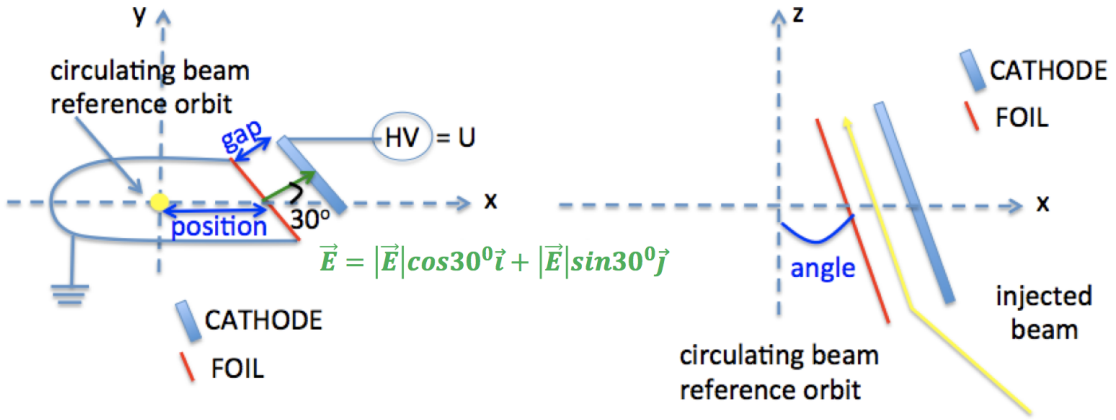

Fig. 1: XY septum view

Fig. 2: ZX septum view

Figure 26: ER.SEH10 septum parameters. Gap, position and angle are parameters that can be trimmed as shown in Fig 27

where p_{LSA} is the momentum per nucleon multiplied by the atomic mass A, and divided by the number of charges Q, e is the elementary charge, γ_{rel} is the relativistic gamma, m_0 is the ion rest mass and l_{eff} is the effective length previously defined. The particle charge and rest mass come from the fields "Particle Type" in the beam process type. p_{LSA} is derived from the Attribute BRHOd defined in the beam process type DISCRETE_LEIRInjection. Figure 28 shows the relationship between the parameters used to calculate the voltage (in unit of kV), using the Make Rule called *K2VoltageMakeRule.java*.

2.8.2 Magnetic septum ER.SMH11

A detailed description of the device can be found in (5). The magnetic septum deflection angle can be trimmed using the high level parameter logical.ER.SMH11/KICK (rad), shown in Fig. 29. The Make Rule *LeirTransferK2CurrMakeRule.java* calculates the corresponding current (A) using the p_{LSA} (derived from LEIRInjectionBEAM/BRHO parameter) and the calibration factor, calib_factor. The parameter hierarchy is shown in Fig. 30. The calibration factor for the ER.SMH11 is:

$$\frac{B \cdot \ l_{eff}}{I} = calib\_factor = 1.886 \cdot \ 10^{-4} \ Tm/A \tag{16}$$

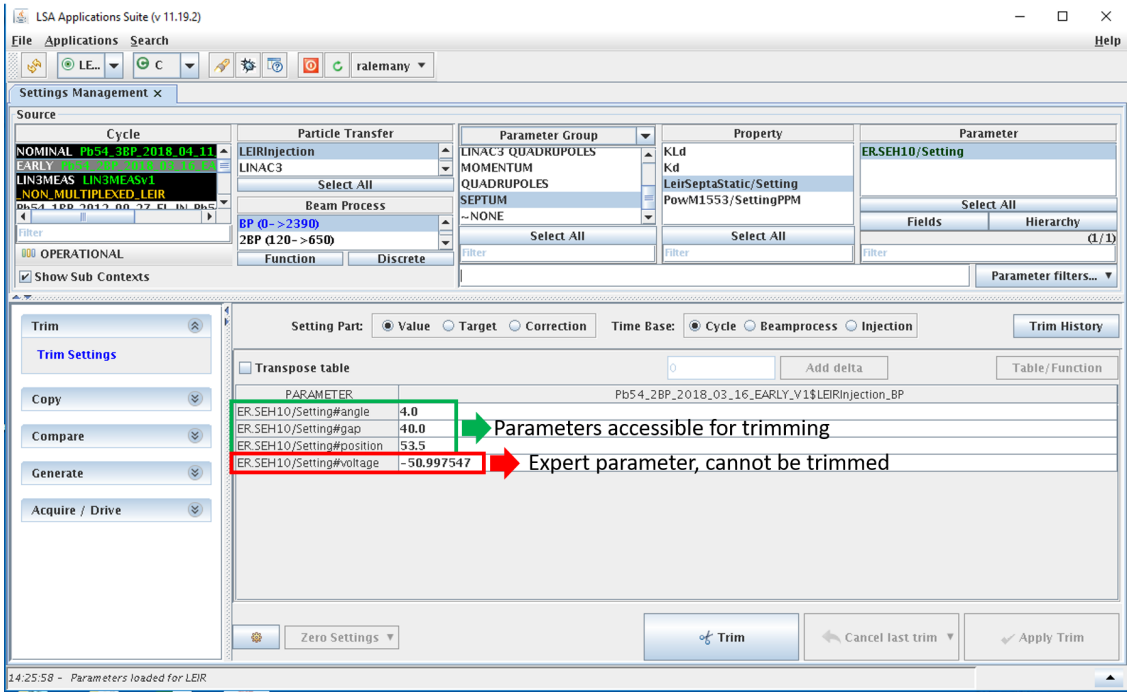

Figure 27: ER.SEH10 septum schematic drawing. Gap, position and angle are parameters that can be trimmed.

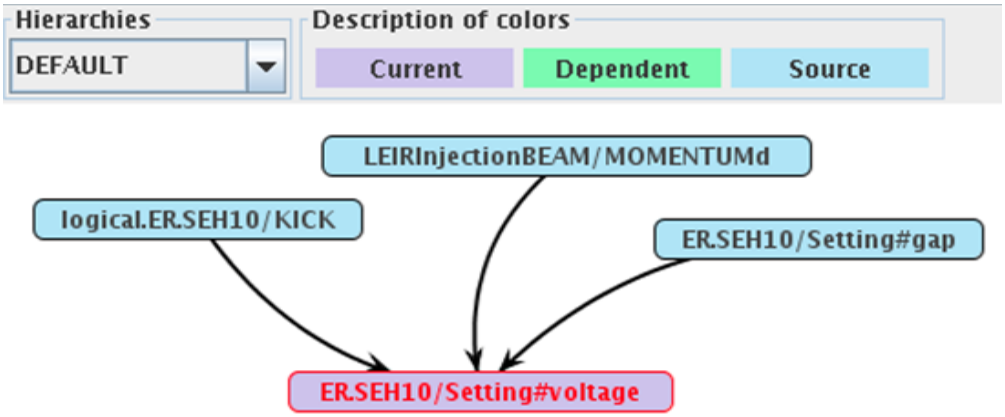

Figure 28: Parameters hierarchy used to calculate the voltage (in units of kV), using the Make Rule called *K2VoltageMakeRule.java*. Whenever the kick, gap or momentum are changed (because of a different particle type) the new voltage is automatically calculated.

2.9 Upgrade to FGCs

During YETS 2017-2018 several quadrupole and dipole circuits in the Linac 3 to LEIR transfer line underwent an upgrade of the power converters (PC) control. The old system was Maxidiscap (+1000 V, +320 A) power converters based on MIL-1553 control system operated with 100 ms pulse spacing since 2016 in the framework of the LIU-IONS project. In order to increase the reliability and standardize the control the circuits listed in Tab. 5

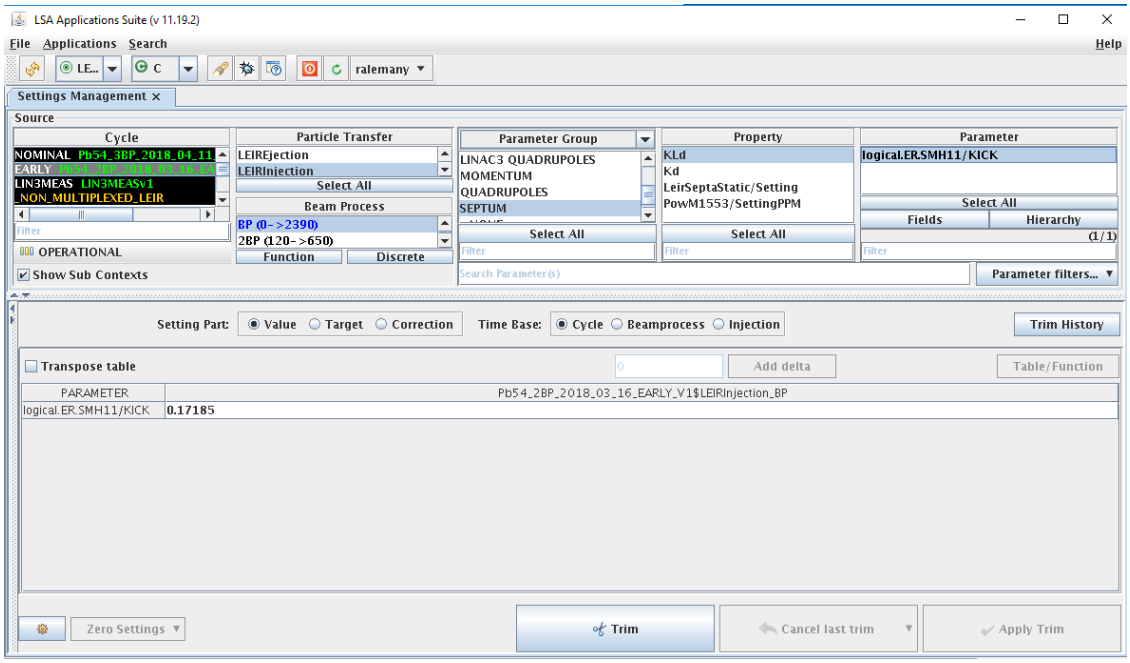

Figure 29: LSA high level parameter logical.ER.SMH11/KICK representing the deflection angle in units of radians.

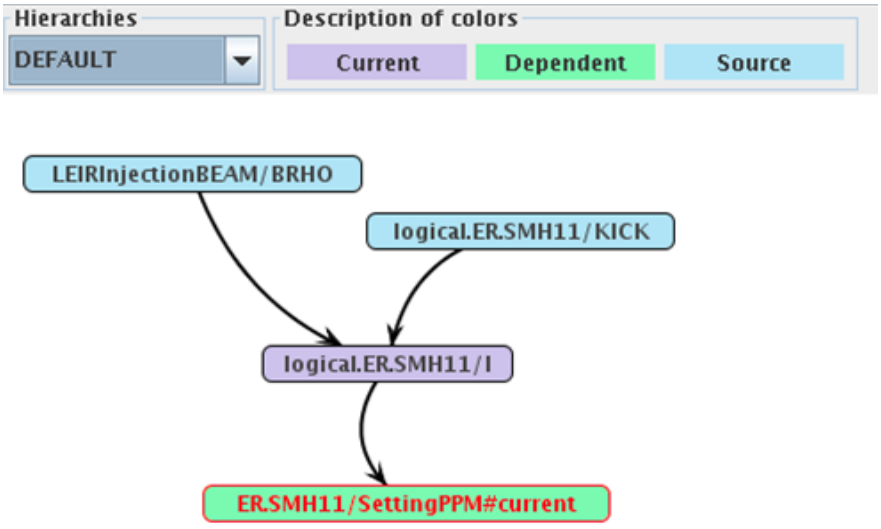

Figure 30: Parameters hierarchy used to calculate the current (in unit of A), using the Make Rule called *LeirTransferK2CurrMakeRule.java*. Whenever the kick or the $B\rho$ (because of a different particle type) is changed the new current is automatically calculated.

were upgraded to FGC3 based electronics (18), and use the FGC_{62} class.

The converters could be commissioned starting in February 2018. When testing them with the LSA/Working set and knobs, the following issues had to be addressed (as a reminder for future upgrades to FGCs):

- For RBAC, FGC devices are protected by location, and therefore usable computers

Line	Circuit name	Alias
ITF	RPAFX.351.ITF.RQFN04	ITF.QFN04
	RPAFX.351.ITF.RQDN05	ITF.QDN05
	RPAFX.351.ITF.RQFN06	ITF.QFN06
	RPAFX.351.ITF.SPARE1	
	RPAFJ.351.ITF.RDVT03	ITF.DVT03
	RPAFJ.351.ITF.RDHZ04	ITF.DHZ04
	RPAFJ.351.ITF.RDHZ03	ITF.DHZ03
	RPAFJ.351.ITF.RDVT01	ITF.DVT01
	RPAFJ.351.ITF.RDVT04	ITF.DVT04
	RPAFJ.351.ITF.RDHZ01	ITF.DHZ01
	RPAFJ.351.ITF.RDVT02	ITF.DVT02
	RPAFJ.351.ITF.RDHZ02	ITF.DHZ02
ITH	RPAFX.351.ITH.RQDN08	ITH.QDN08
	RPAFX.351.ITH.RQFN09	ITH.QFN09
	RPAFX.351.ITH.RQDN10	ITH.QDN10
	RPAFX.351.ITH.SPARE1	
ITE	RPAFX.150.ITE.RQFN01	ITE.QFN01
	RPAFX.150.ITE.RQDN02	ITE.QDN02
	RPAFX.150.ITE.RQDN04	ITE.QDN04
	RPAFX.150.ITE.RQFN05	ITE.QFN05
	RPAFX.150.ITE.SPARE1	

Table 5: Circuit names upgraded to FGC control electronics.

must be correct associated with the same location.

- The synchronization of pulsed converters with the beam needs to be independently checked, and it would be good practice to provide a trigger like IX.SEJ to facilitate verifying the synchronization locally.
- OASIS signals need to be available for commissioning (when made available there were issues with sampling rate and synchronization that had to be addressed).
- The operation of the controls needs to be verified in PPM, and with different pulsing structures for Linac 3/LEIR, including that the correct settings are applied on the correct cycle, and that multiple pulses occur.
- MIN and MAX values, as well as the TOLERANCES for displaying them in red in working sets, need to be set and checked to be working.

3 RF overview in 2018

In 2018 the low level (LL) RF experienced a series of improvements. Though not affecting the beam performance, they were important to improve the system performance and the compatibility with other CERN machines.

3.1 Fixed frequency LLRF clock implementation

The LLRF clocking scheme was upgraded from sweeping to fixed frequency before the start of the run. The previously-used sweeping frequency clocking scheme was set to harmonic h = 64 of the revolution frequency whilst the fixed-frequency clocking scheme was set to 122.7 MHz. The upgrade required modifications of the firmware, DSP (Digital Signal Processor) code, and FESA class changes, but no hardware modifications. The main reason for the upgrade was to align the LEIR LLRF to the new standard for this LLRF family, thus easing maintenance and software support. The fixed frequency clocking scheme had already been successfully validated in ELENA in the 2017 run, and will be used in the PSB and AD after LS2. The fixed frequency clocking scheme grants a signal-to-noise ratio higher than the sweeping frequency scheme; however, this improvement is not measurable for LEIR as the beam signals are already strong. Owing to this change, the previous archives for all the users were no longer valid as the phase rotation parameters are different.

3.2 Optimisation of the numerical implementation of the frequency formula

The frequency program was also upgraded before the start of the 2018 run. The upgrade consisted of optimising the numerical implementation of the formula that converts the B-train to a frequency value. This change was due to a quantisation problem discovered in ELENA caused by the very low magnetic field at extraction. In LEIR such quantisation existed but was negligible as it amounted to 2 Hz at injection energy (low energy, worst case). The main reason for the upgrade was to align the LEIR LLRF DSP code with what was deployed in ELENA. The frequency program code in the PSB was upgraded as well, before the PSB restart in 2018 for uniformity and ease of maintenance. The new DSP implementation grants a sub-Hz resolution in the frequency program calculation over the whole B-train range, by changing the order of the operations and the parameters scaling (19).

3.3 DSP-based implementation of the frequency offset modulation

The frequency offset modulation was moved from a LabView program to a DSP-based implementation in the LLRF frontend before the 2018 run. This was obtained by adding two FGCs and deploying new, dedicated DSP code and FESA classes. The effect on the beam was equivalent to that obtained in the previous LEIR run but the upgrade allowed an easy archiving of all input parameters and easier control of them. This frequency offset modulation scheme was used operationally in 2018.

3.4 Integration of the new WR B-train

The LLRF was interfaced with the new WR (White Rabbit) B-train in the 2018 run (see Sec. 4). There was a difference between the values measured by the WR B-train with respect to what was measured by the Bupdown system[4]. As a result the radial loop contribution is higher for operation with the WR B-train. However, the LLRF managed to successfully capture, accelerate and synchronise the beam when receiving the WR B-train as input. A reliability run was carried out when the beam was sent to LHC for collisions. A new set of diagnostics was deployed in the LLRF to allow the B-train team to log LLRF data on B-train operation. Finally, in November the firmware interfacing with the B-train was upgraded to the new version developed for the PSB, where reliability problems in the LLRF−B-train interfacing were discovered. A communication problem at power-up was still present after the upgrade and affected LEIR, too. A software workaround exists and BE/CO is committed to solve the problem during LS2.

3.5 Interface with the transverse feedback and orbit systems

In 2018 it was observed a systematic discrepancy between the beam position measured by YASP at the interpolation between pickups UEH31 and UEH32, and the radial position measured by the RF low level radial loop system, which uses the same pair of pickups. The operational configuration of the radial loop uses the average position of both devices. Tests were done using only one of them, alternatively, and comparing the results to the YASP measurement. It was seen that the Transverse Pick-Up (TPU) 31 (also referred as UEH31) provided wrong measurement compared to TPU32 and YASP. The issue was traced back to a bad connector in the transmission of the Delta signal from the orbit to the LLRF crate. It was solved by replacing the cable. Additionally, the calibration factors for the two TPUs (UEH31 and UEH32) used by the LLRF were found to be inverted following a cable re-organisation. That was solved and finally the two radial positions measured by the LLRF were compatible with the corresponding YASP values.

The LLRF interface to the orbit system was completed during the 2018 run by adding the possibility for the LLRF to read the orbit position measured by the orbit system in real-time over optical fibre. This value was also made available as LLRF Oasis signal. It was possible to close the radial loop on the orbit position and MD sessions were carried out. The orbit signal was slower than the radial position measured by the LLRF, due to the long averaging time in the orbit system, hence the radial loop response time was longer than for standard operation.

3.6 Cavity limits management

The handling of the cavity limits in the LLRF and the general high level (HL) RF operation were improved during the 2018 run. The PLC program was debugged and the proven dependencies between the two cavities (elements CRF41 and CRF43 in the ring) minimised.

[4]The B-UP and B-DOWN (Bupdown) are redundant signals of 24 V amplitude separated 1 μs. Each pulse represents a step of + 0.1 Gauss (B-UP) or - 0.1 Gauss (B-DOWN) in the measurement of the main dipole magnetic field.

Problems still existed at the end of the run in the remote control of the two HLRF systems but they were much rarer than before.

3.7 Future development plans

There will be some changes in the LEIR RF system during LS2. First, the operating system running in the LLRF frontend will be upgraded to CC7. The FESA classes will also be upgraded to FESA v7.0.0. The FESA classes for the ALLVXSTIM (FESA class in charge of the timing signals) and ALLVXSGFAS (FESA class in charge of the function generation) will be replaced with new, equivalent classes, in synergy with SPS developments. The LLRF firmware will be modified to receive inputs from the WR B-train only and not also from the Bupdown. The WR B-train diagnostics will be fully deployed.

On the HLRF side, the Scheinder PLC will be replaced by a new one (Beckoff). It is also hoped that EPC consolidates the HLRF remote control part. If so, studies could be carried out before LEIR restarts to ascertain the results.

4 New LEIR B-Train reliability run results

4.1 Introduction

The legacy B-train system, based on VME acquisition electronics and incremental 24 V-pulse field distribution, has been in operation since the early 2000's, but is now being phased out due to obsolescence of the Lynx front-end computer's operating system. In the frame of the CERN-wide consolidation project, a new B-train system based on PCIe electronics and White Rabbit serial distribution of the measured field has been installed to replace it. Below, we report the results of a series of test runs in 2018 to commission and qualify the new system.

4.2 Preliminary B-train comparison

Some preliminary tests were carried out during the summer of 2018 to directly compare the performance of the old and new B-trains:

- Operational EARLY cycle (12 June 2018): measurement of field, radial beam position and frequency correction of the RF radial loop, beam intensity
- Clone of NOMINAL cycle (08 August 2018): tomoscope measurements

Since the two B-train systems are independent they can run simultaneously, which allows a continuous comparison of the respective outputs. These were fed alternately to the LLRF and the beam current transformer (BCT) in order to evaluate any possible impact on beam behaviour.

4.2.1 Measured Field

The two field measurements are shown as a function of time in Fig. 31a, while their difference $\Delta B = B_{\text{new}} - B_{\text{legacy}}$ is in Fig. 31b. The peak difference is about -1.3 mT (i.e. about 10^{-3} of the peak field) and is observed at the time of maximum $\frac{dB}{dt}$ on the ramp-up. This suggests that the difference is mainly due to edge eddy currents being closer to the new sensor location than the center of the gap, where the legacy coil is installed (see Sec. 2.6 for details). A zoomed-in comparison of the two B-trains at injection is given in Fig. 31c, which clearly shows how the switch to White Rabbit distribution improves the effective resolution from ± 10 μT to ± 0.2 μT. The 50 μT offset between the two curves is due to the absence of a field marker in the legacy system, leading to a calibration error.

The correlation of new to legacy B-train is plotted in Fig. 31d and is given by the following linear relationship

$$B_{\text{new}} = 0.9997 B_{\text{legacy}} - 0.94 \text{ mT} \tag{17}$$

with a RMS residual of about 50 μT, well above measurement noise. While the large offset difference is fully expected, due to the lack of a field marker in the legacy system, the correlation factor < 1 suggests that the gain of the acquisition chain of the new B-train is underestimated and should be adjusted accordingly.

The transfer function of the dipole magnet, i.e. the ratio between the field measured by the new B-train and excitation current, is represented in Fig. 32. On the up-ramp, instead

of the common high-field drop due to saturation, we can observe a uniform decrease of about -0.8% between injection and extraction. This decrease, observed in other strongly curved magnets (such as ELENA's bending dipoles (20)), may be attributed to a combination of factors including error on the gain and offset of the measured field, or a staggered onset of saturation in different parts of the magnets.

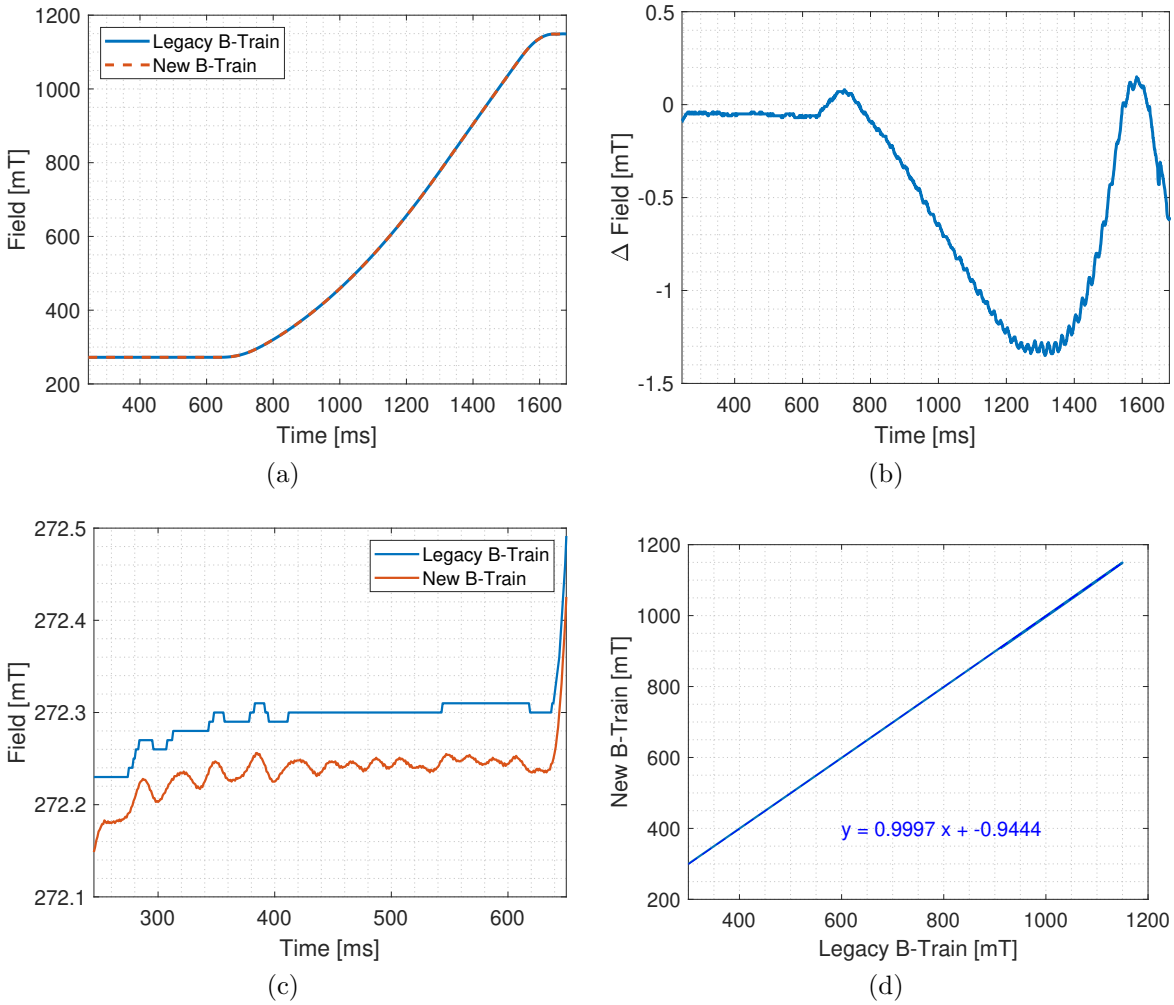

Figure 31: LEIR B-train systems difference on EARLY cycle. (a) B field measurements as a function of time, (b) difference $\Delta B = B_{\text{new}} - B_{\text{legacy}}$, (c) zoomed-in comparison of the two B-trains at injection, (d) correlation of new to legacy B-train.

4.2.2 Radial Position

The impact of the new B-train on the overall beam performance is best evaluated via the mean radial position and the frequency correction contribution of the radial loop, shown respectively in Figs. 33a and 33b. The largest frequency correction is about -2.0 kHz at 1.3 ms into the cycle, which corresponds to a field error of -1.7 mT at 800 mT. This is about four times as high as the correction with the legacy B-train, however it remains well within

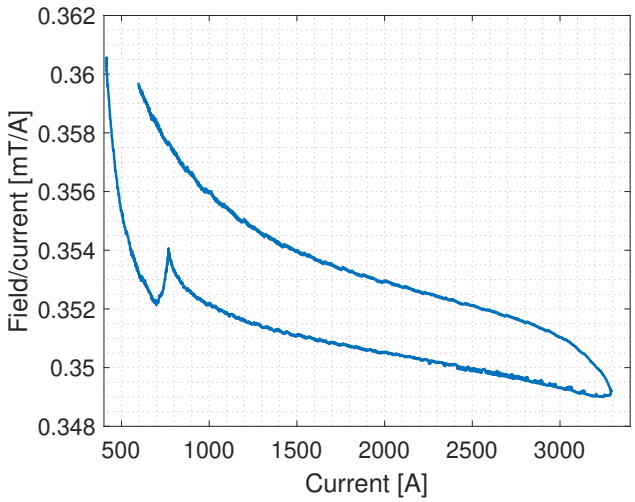

Figure 32: LEIR main magnet (BHN30) transfer function.

the nominal capability of the radial loop i.e. ± 5 kHz. A few milliseconds before extraction the frequency correction drops in magnitude down to 500 Hz, which corresponds to 0.5 mT at 1150 mT.

Despite the field error, the mean beam radial position appears substantially more stable with the new B-train, with a systematic difference of 0.2 mm and the RMS noise level dropping from 0.37 to 0.10 mm, likely due to the improved resolution of the new B-train. Overall, the mean radial position remains well within ± 1 mm.

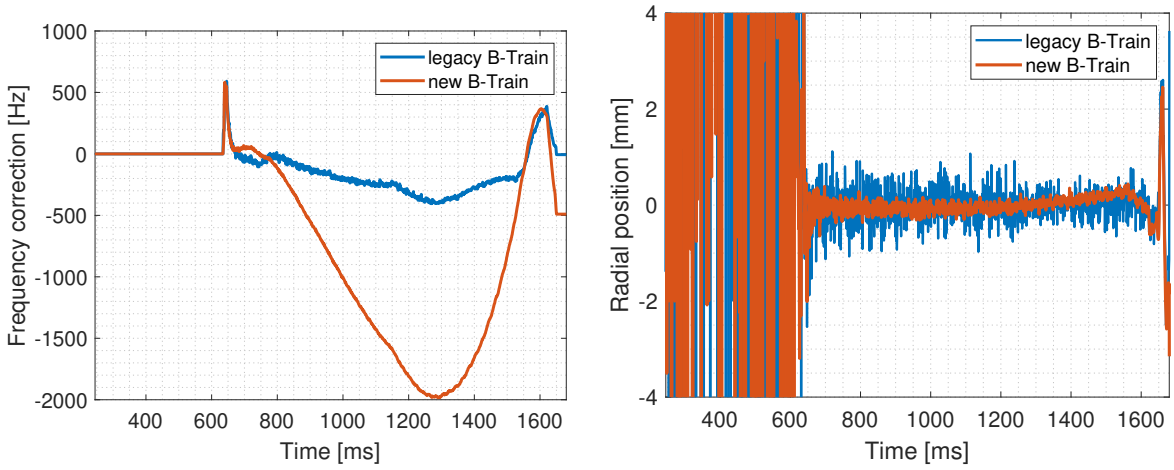

(a) (b)

Figure 33: Radial beam position on EARLY cycle. (a) frequency correction contribution of the radial loop between legacy and new B-train, (b) mean beam radial position from the radial loop pickups.

4.2.3 Beam intensity

The number of circulating particles with the legacy and the new B-train is plotted in Fig. 34. The difference during injection is less than 10%, which is consistent with routinely observed fluctuations due to Linac 3 intensity and beam losses. This measurement also validates the transmission performance of the new White Rabbit B-train to the BCT, which uses it to compute the relativistic β factor to normalize the measured beam current.

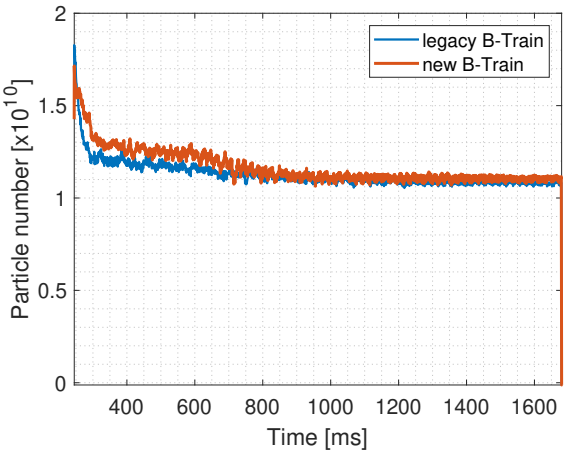

Figure 34: Particle count from BCT. The different intensity during injection is less than 10% and consistent with cycle-by-cycle fluctuations.

4.2.4 Beam profiles

Figure 35 shows beam phase space profiles measured on a NOMINAL cycle at extraction on 8 August 2018 by the tomoscope with the legacy and the new B-train. No appreciable impact of the new B-train on the structure of the beam can be detected.

4.3 Reliability run results

A reliability run including a total of 68286 cycles was performed from August to December 2018, in order to validate on a statistical basis the sensors, electronics, controls and transmission parts of the B-train system for the post LS2 period of operation. All measurements were carried out in a dedicated cycle (Pb54_2BP_2018_03_16_EARLY_V1_Clone_for_BTRAIN, a clone of the operational EARLY cycle). Figure 36 shows the corresponding magnetic cycle. The accumulated number of cycles is plotted in Fig. 37, where one can see a pause between early September and mid-October that was due to various operational constraints. Such a long run was possible thanks to a sufficient number of available machine development slots and, crucially, to the possibility of switching between the legacy and new B-train systems on the fly using the so-called Pulse-to-Pulse Modulation (PPM) function, which allows to set independent configuration parameters to each cycle type.

On top of the dedicated cycle for the reliability run, whenever the super-cycle sequence allowed, a special calibration cycle without beam (*Pb54_3BP_2018_04_11_NOMINAL_B_TRAIN_CALIB*) was inserted to carry out offset and gain correction of the PCIe

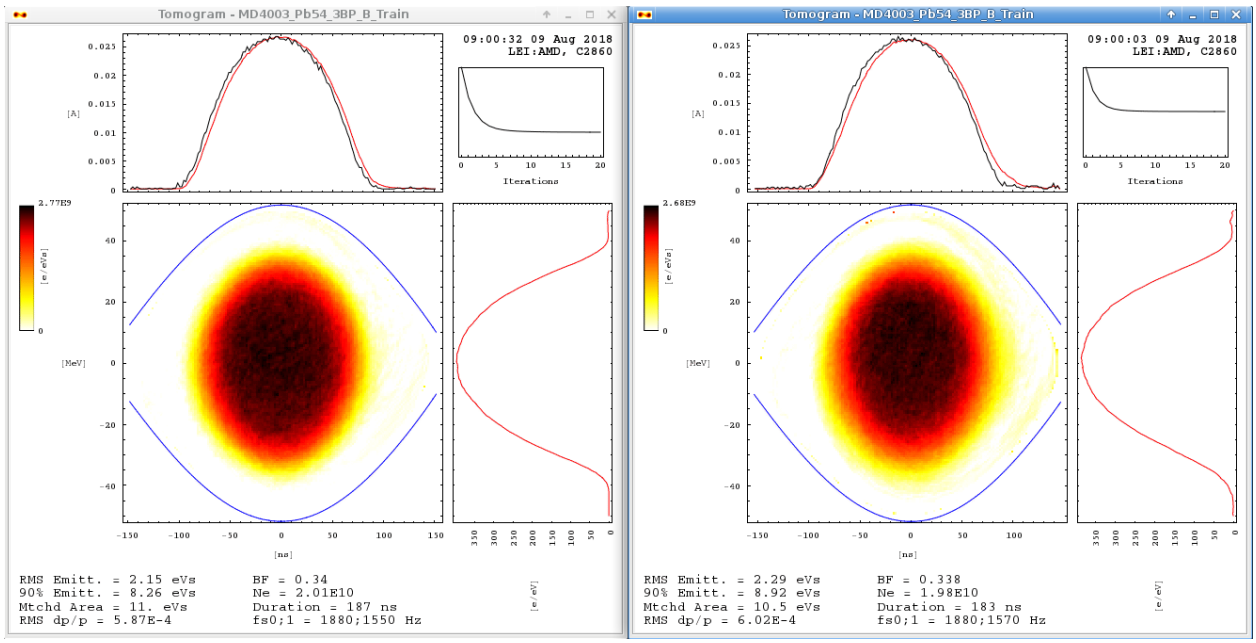

Figure 35: LEIR tomoscope legacy versus new B-train. (left) Legacy system (right) new operational system.

integrator by applying a sequence of reference voltages (i.e. −8.75 V, 0 V and +8.75 V) to its input.

The overall stability of the new B-train system was satisfactory throughout the run. The only major interruption happened when the B-train was restarted without any calibration cycle, which generated large errors due to a high uncorrected voltage offset. This problem has now been fixed and, after a system restart, no output will be generated until offset calibration has been performed.

A summary of the comparison between the old and the new B-train, including both the new operational and spare chains, is given in Tab. 6. The differences and stability of the three systems are discussed in detail in the sections below.

4.3.1 Stability at injection

On the EARLY cycle, injection begins at $t_{\mathrm{inj}} = 245$ ms into the cycle, when the magnetic field attains a nominal value of 272.1 mT. The field measured by the new operational B-train at $t = t_{\mathrm{inj}}$ over the whole set of cycles is plotted in Fig. 38a, which shows an overall peak-to-peak variation of about 300 μT and a standard deviation of 40 μT, well within the tolerance of the machine. The standard deviations of the legacy and new spare B-train are closely comparable, 30 and 52 μT respectively.

The air temperature in the vicinity of the magnet gap is plotted in Fig. 38b alongside the temperature of the B-train electronic racks. The temperature variations are higher on the racks, which are installed in building 150/R-031 outside the concrete walls of the bunker, next to the hall door, hence more exposed to the external environment. The measured field is strongly correlated to the gap temperature, via a mechanism that is not clear at the moment. The correlation is especially evident in the well-visible daily periodic fluctuations, which

Parameter	N. of cycles	Mean	Min.	Max.	Range	St. dev.
T_{mag} (C)	68286	24.2	16.9	29.0	12.1	2.5
Bud_{i}	68285	272.20	272.16	272.28	0.12	0.03
Bwr_{i} (mT)	68286	272.1036	271.9480	272.2510	0.3030	0.0397
$BwrSP_{\mathrm{i}}$ (mT)	36272	272.1151	271.9810	272.2380	0.2570	0.0524
Bud_{e} (mT)	68285	1149.39	1148.78	1150.27	1.49	0.39
Bwr_{e} (mT)	68286	1148.6851	1142.4530	1149.6160	7.1630	0.3697
$BwrSP_{\mathrm{e}}$ (mT)	36273	1148.5021	1142.4370	1148.7710	6.3340	0.1303
$BwrSP_{\mathrm{i}} - Bwr_{\mathrm{i}}$ (mT)	36272	0.0023	-0.1560	0.1340	0.2900	0.0655
$BwrSP_{\mathrm{e}} - Bwr_{\mathrm{e}}$ (mT)	36273	-0.3622	-1.0810	0.2420	1.3230	0.5227
$Bwr_{\mathrm{i}} - Bud_{\mathrm{i}}$ (mT)	68285	-0.0978	-0.2550	0.0260	0.2810	0.0430
$Bwr_{\mathrm{e}} - Bud_{\mathrm{e}}$ (mT)	68285	-0.7057	-1.3700	-0.0850	1.2850	0.2355

Table 6: B-train field summary for the legacy and the new systems, both the operational and the spare. A lower number of cycles applies to the spare new system, due to development work going on in parallel with the tests. T_{mag} is the temperature of the BHN30 magnet, Bud is the field measured by the legacy system, Bwr and $BwrSP$ are the field measured by the new operational and spare systems, and the subscripts i and e denote respectively injection and extraction times.

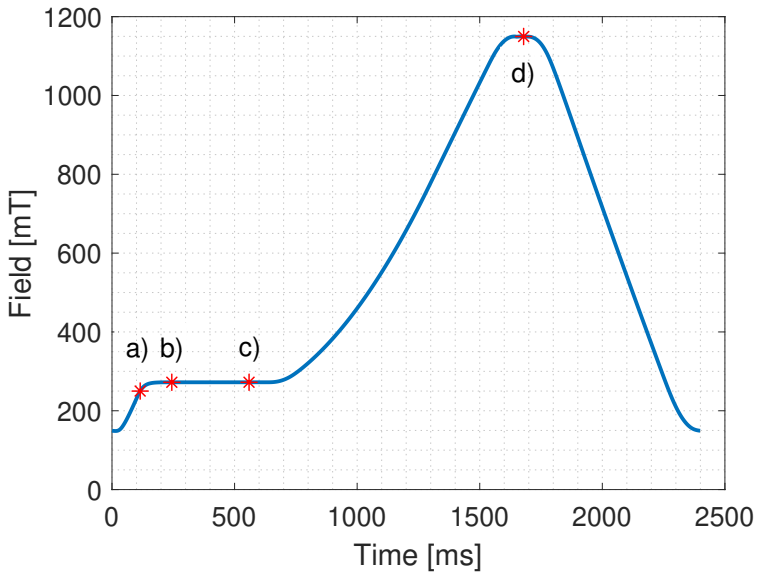

Figure 36: LEIR EARLY cycle clone used for the reliability run, a) is the resonator sensor marker at t=116 ms. b) is the beam injection at t=245 ms, B=272.1 mT, c) is the LLRF loops closure at t=560 ms and d) is the beam extraction at t=1680 ms, B=1.1497 T.

correspond to sequences of about 2500 cycles. This temperature effect at injection is not visible with the legacy B-train, since the system was started with a preset software marker. The correlation of field and temperature is shown in Fig. 38c. The correlation coefficient is 19 μT/°C (or, in relative terms, 70 ppm/°C), in contrast with the value of -10 ppm/°C that would be expected from the thermal expansion of the magnet gap; this excludes any possible thermal effect on the geometry of the magnet, which at any rate could not follow such rapid variations due to its large mass. The correlation is much stronger with the gap temperature

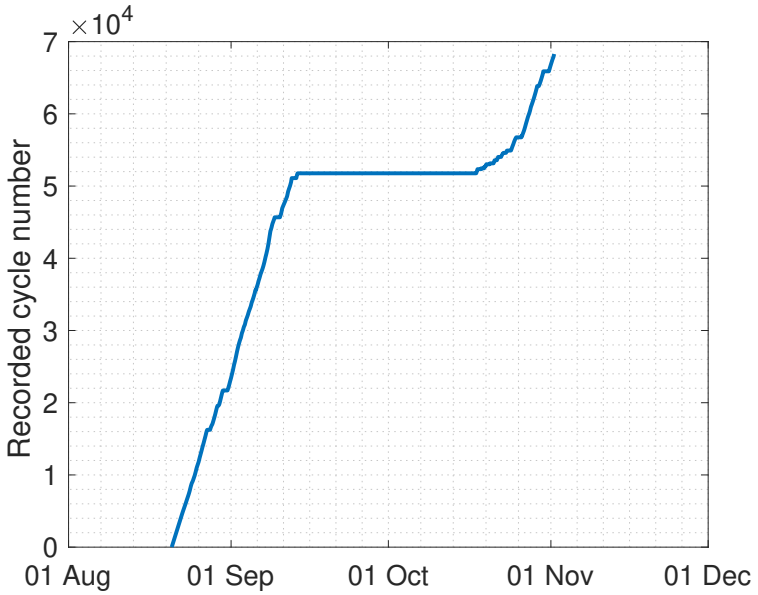

Figure 37: Accumulated reliability run cycle count.

than with the temperature measured in the acquisition racks, which is also plotted in Fig. 38b; this excludes any thermal effects on the acquisition electronics (which actually includes a temperature-stabilized voltage reference). We recall that the sensor assembly is thermally stabilized, which excludes a direct influence of ambient temperature on the readings. A possible error source may be related to small thermally-induced deformations of the sensor support, for example any rotation around the radial direction, to which the resonating YIG sample is extremely sensitive (about 368 μT/°C) measured in a dedicated calibration setup. Whatever the cause, if temperature correlation is subtracted from the data, the residual is essentially random noise with a standard deviation of 38 μT i.e. 1.41×10^{-4} relative to peak field (see the histogram in Fig. 38d).

A subset of the test data has been analysed separately to derive indications on the reproducibility of the FMR marker, as well as the correlation to the correction applied by the radial RF loop. The subset includes 1515 cycles within a narrow temperature range i.e. 24.3 ± 0.5°C, in order to eliminate as much as possible the influence of thermal effects (this particular temperature was chosen to obtain a large subset). The field measured by the new operational B-train at injection and the relative histogram are represented in Fig. 39. The standard deviation is 15.6 μT (5.7×10^{-5}), which can be considered as an upper bound for the reproducibility of the FMR marker, neglecting excitation current ripple, timing jitter, mechanical vibrations and other perturbations. This result is consistent with the reproducibility measured under strictly controlled conditions in building 311 on a dedicated FMR test bench, i.e. 14 μT (15).

4.3.2 Stability at extraction

At extraction ($B = 1.1424$ T at $t = 1680$ ms), the average difference between the new operational and the legacy B-train is about 600 μT; based on the measured correlation (Fig. 31d), this can be attributed to a combination of gain and offset error. In particular,

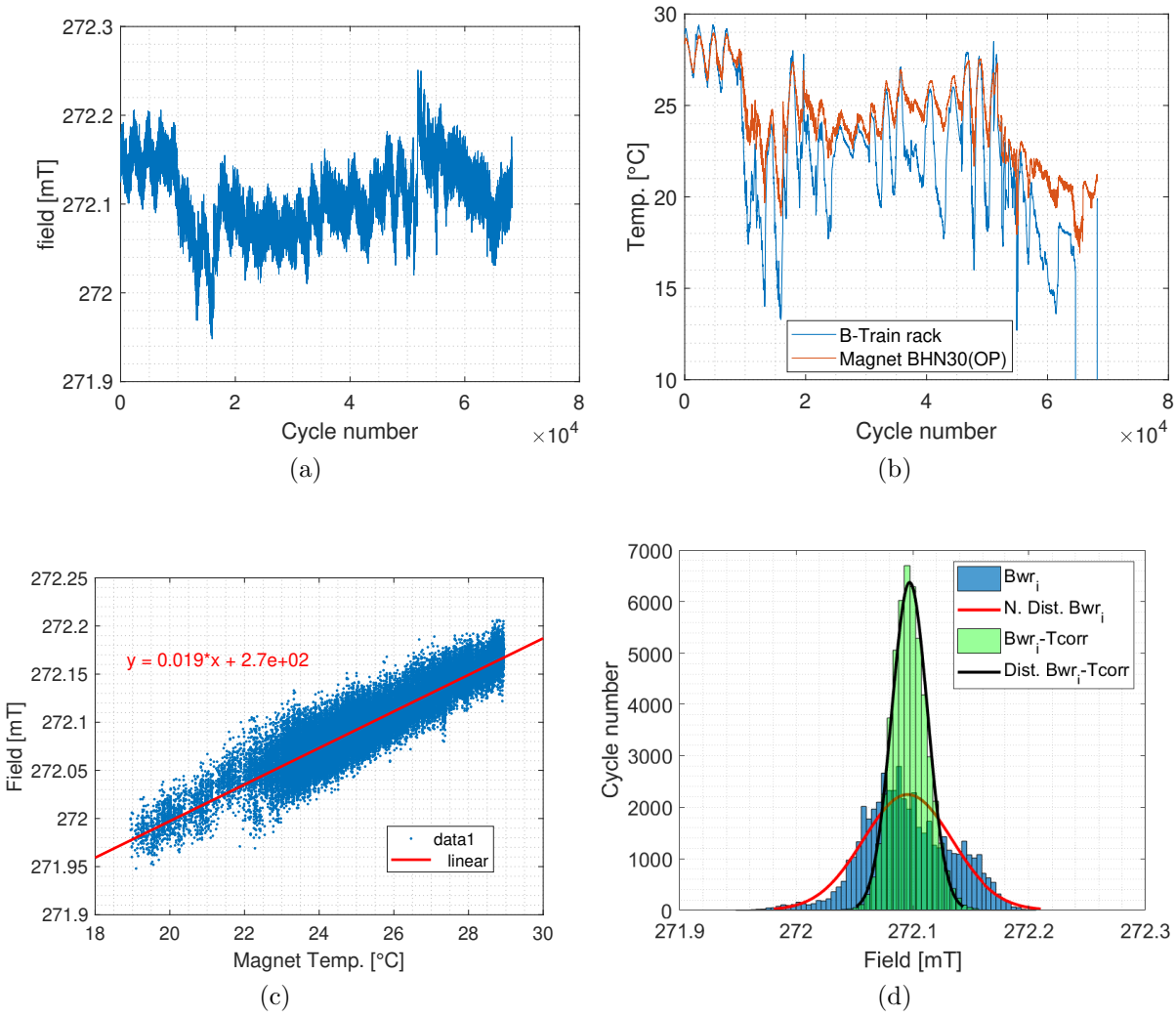

Figure 38: Field stability at injection. (a) Field value at injection for all cycles. (b) Temperature in the B-train rack (blue) and the magnet close to the B-train sensors (red). (c) Correlation between the temperature and the injection field. (d) Distribution of the field at injection: raw data (blue), residual of the linear correlation (green). The bin size is about 10 μT. The continuous curves represent the best-fit to a Gaussian distribution.

the fixed offset of the legacy system may be a significant source of error, due to magnetic hysteresis effects being ignored. The stability of the two measurements is 370 μT and 390 μT respectively, i.e. one order of magnitude worse than at injection. The stability may be affected by the following error sources:

- **integrator drift**: this is normally the dominant error source in fluxmetric measurements. After each periodic re-calibration, the voltage offset is expected to have a zero average and vary randomly, independently for each acquisition channel. The similarity between the stability of the two systems therefore suggests the presence of a different, underlying systematic cause.
- **timing jitter**: this is typically well below one microsecond, and since the mean ramp

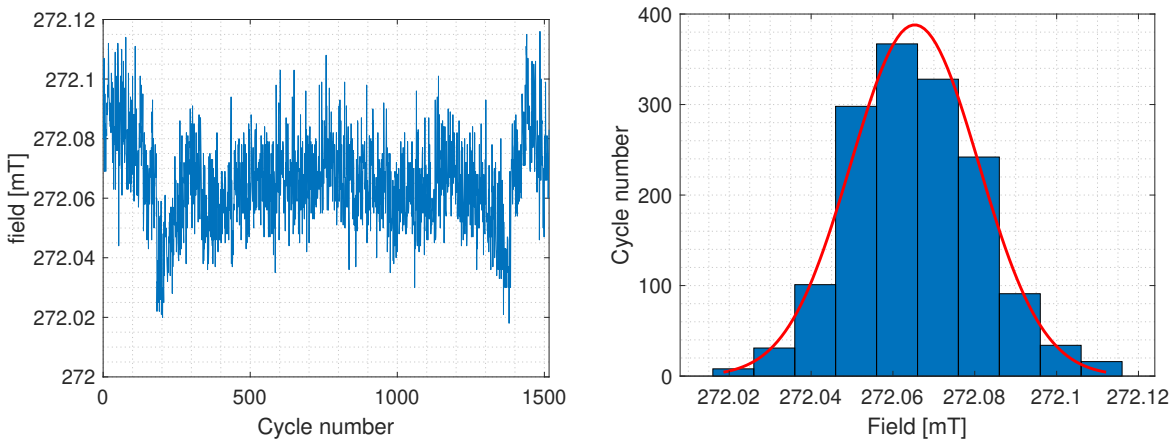

(a) (b)

Figure 39: Field stability at injection and 24.3°C. (a) Field at injection with a temperature of 24.3°C for 1515 cycles. (b) The corresponding distribution with a bin size of 10 μT; the red curve is its Gaussian best-fit.

rate is about 1 T/s this leads to negligible field errors $<$ 1 μT.

- **current ripple**: a zoom-in of the excitation current on the injection plateau is plotted in Fig. 40. The measured standard deviation is 0.1 A which, taking into account the transfer function i.e. 354 μT/A, corresponds to an uncertainty equal to 35 μT. This value, which is already very low, seems to be overestimated because of the low resolution of the current measurement.

- **magnet gap temperature**: this appears indeed to be the dominant factor, as can be derived from Fig. 41.

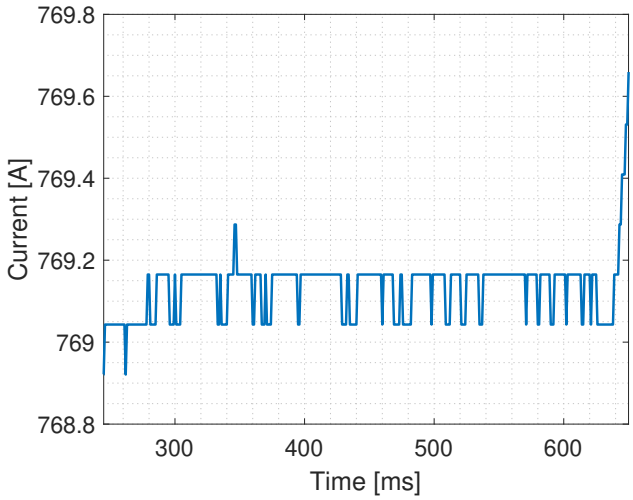

Figure 40: LEIR current at injection EARLY cycle.

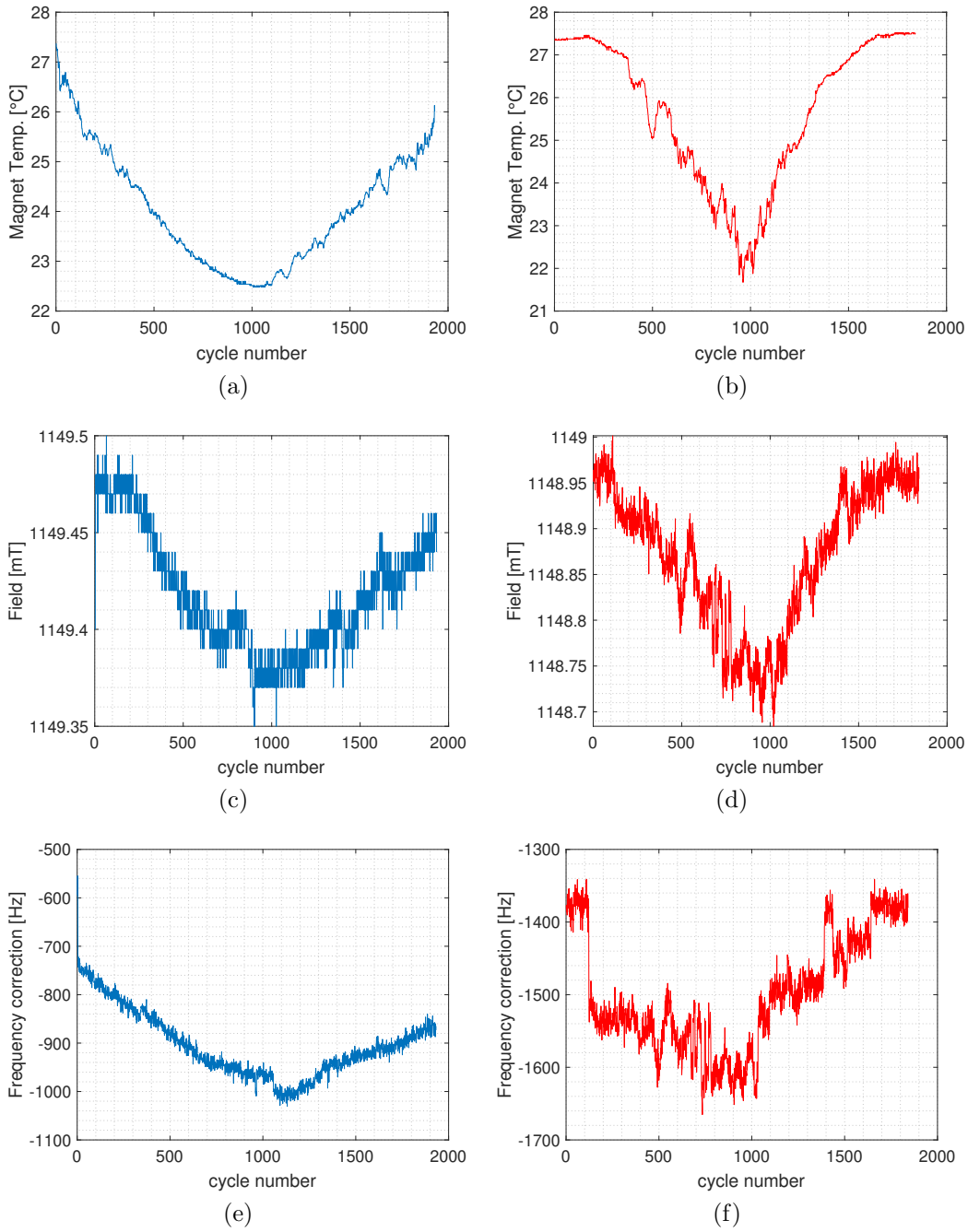

Figure 41: LEIR reliability run radial loop legacy versus new B-train at extraction during one day (∼1930 cycles). The blue curves (left) are measurements taken the 28-29th August 2018 with the legacy B-train system as source for the LLRF. The red curves (right) are measurements taken the 11-12th September 2018 with the new B-train system as source for the LLRF, (a) and (b) are the temperatures of the BHN30 magnet, (c) and (d) are the B-fields, (e) and (f) are the LLRF radial loop contributions.

The measurements shown were taken by feeding alternately the new operational and the legacy B-train to the RF on two different days, during which the thermal excursion was

respectively about 6°C and 4°C. The new B-train shows a greater variability, due to its finer resolution. Some of the wider, abrupt variations (e.g. after 100 cycles and 1400 cycles) are an artefact due an integration re-calibration error, which is in the process of being corrected.

Both B-trains exhibit a clear positive correlation with the temperature, respectively about 50 μT/°C and 25 μT/°C. The relative correlation coefficient for the new B-train is 44 ppm/°C, which is comparable to the coefficient at injection; this suggests that the same underlying mechanism (i.e. thermal deformation of the sensor support) may be responsible. The impact on the legacy B-train is lower, but the cause is less clear: in fact, the measuring coil is supposed to be in thermal equilibrium with the iron yoke, rather than the surrounding air. Unlike the new B-train, however, the legacy acquisition electronics is installed next to the LEIR control room in an open rack, hence is exposed to variable ambient conditions.

The RF radial loop correction is shown in Figs. 41e and 41f. The average value is about -1.5 kHz and -0.9 kHz for the new and legacy B-trains respectively. Since the radial loop correction depends upon many beam parameters beside the magnetic field, the equivalent field differences i.e. -1.5 mT and -0.9 mT, can be considered in absolute value as an upper bound for the field measurement error.

The frequency correction is also positively correlated with the gap temperature, and the correlation coefficients for the new and legacy B-train are 50 Hz/°C and 75 Hz/°C respectively. The equivalent coefficient in terms of field error for the new B-train is 50 μT/°C, which coincides precisely with the observed correlation. Such correspondence supports the hypothesis that the temperature does not affect the magnetic field, but only the measurement; the systematic component of this error could therefore be compensated by subtracting from the measurements the linear temperature contribution. The equivalent coefficient for the legacy B-train is 75 μT/°C, which is instead three times as high as the coefficient of the measured field. This may be linked to the initial offset of the legacy measurement, which may contain some temperature dependency that is not included in the measurements because of the fixed offset applied.

	B-train source to the LLRF	
	Legacy	New
Temperature variation BHN30 (°C)	4.77±0.18	5.15±0.11
Field variation (mT)	0.1±0.01	0.192±0.015
Radial loop contribution average (Hz)	-900±20	-1550±50

Table 7: LEIR difference between B-train sources during one day.

4.3.3 Comparison of OPERATIONAL and SPARE new B-trains

Overall, both the operational and spare new systems perform equally well in terms of reliability and noise. The correlation of the two new systems is plotted in Fig. 42 for a single EARLY cycle taken as an example. The linear regression is given by

$$B_{\text{new,OP}} = 0.9986 B_{\text{new,SP}} + 0.05 \text{ mT}. \tag{18}$$

For the cycle considered, the difference between the two systems is essentially due to the gain, since the offset of the correlation is comparable with the uncertainty of the field marker and can be safely neglected. This finding is consistent with the statistics over the whole set of measurements shown in Tab. 6, where the B-train field measured by the operational system is essentially the same as the spare at injection ($BwrSP_{\mathrm{e}} - Bwr_{\mathrm{e}} = 2\ \mu\mathrm{T}$) but becomes much higher at extraction ($BwrSP_{\mathrm{e}} - Bwr_{\mathrm{e}} = -362\ \mu\mathrm{T}$). The gain error of the spare derived from these figures is 317 ppm.

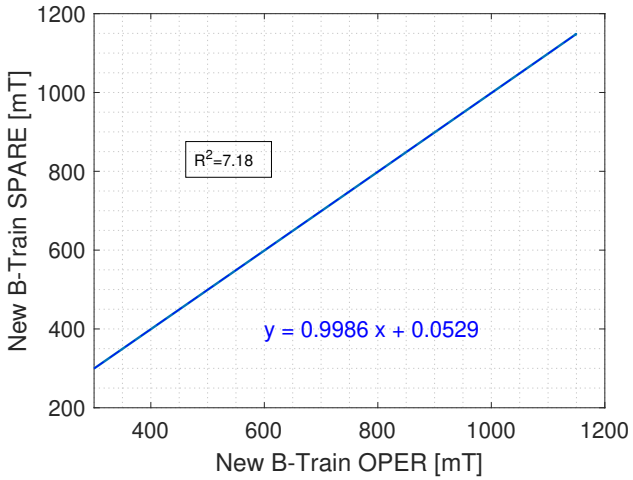

Figure 42: LEIR B-train OPERATIONAL vs SPARE systems correlation.

4.4 B field drift along the injection plateau

During the year a significant B field drift at flat bottom was observed in LEIR (21). Figure 43 shows the acquired Schottky spectrum for a single injection with advanced capture in order to observe the revolution frequency change for 1.25 s along the injection flat bottom. The measurement was done with and without radial loop (RL) correction in place. One can observe that the radial loop tries to correct the revolution frequency of the beam that otherwise would down-shift by about 250 kHz, corresponding to a momentum offset of 0.6 ‰.

This is also visible from the orbit measurements as shown in Fig. 44 where the beam is observed to drift towards the outside the machine by about 6 mm, from the moment of capture and after 1.25 s, compatible with the dispersion of 10 m in straight sections 1 and 3 (where the radial loop pickups are located). The time constant of the process is very large: a coarse analysis shows several hundreds of ms.

The effect was also observed in 2017 (see e.g. LEIR e-logbook on 14-07-2017) and it suggests the B field is decaying along the injection flat bottom. One of the possible explanations is the presence of thick magnetic spacers installed in the first and last module of each bending magnet to correct the total magnetic length and to allow, at the time of LEAR, the installation of pole face windings. In order to confirm or exclude the plates as source of the issue, additional B field probes will be installed during LS2 in the first and last modules of the bending magnets, in addition to the ones used by the White Rabbit B-Train at the centre of the magnet.

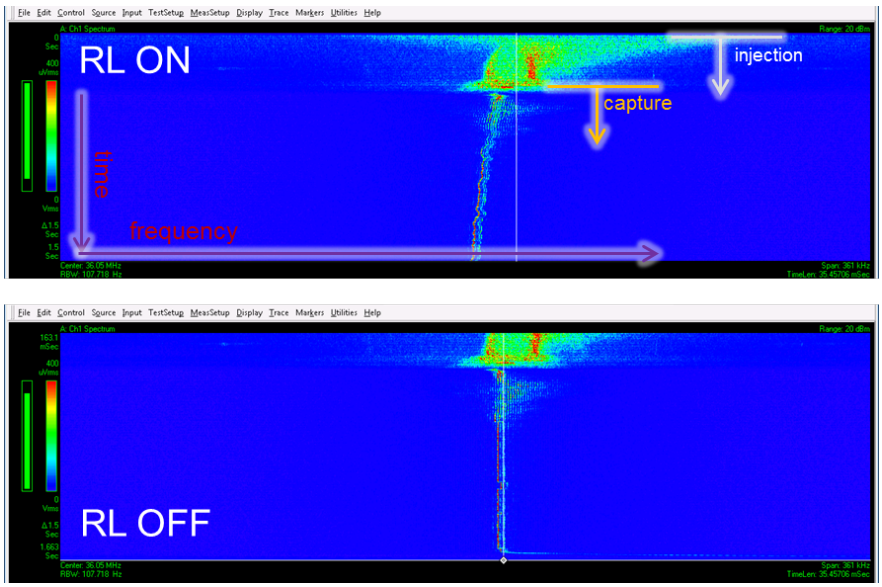

Figure 43: Schottky spectrum of a single injection with advanced capture. After capture, the beam circulates at constant injection energy for 1.25 s. Switching on the radial loop (RL) the beam frequency is changed to minimize the position offset at the radial loop pickups.

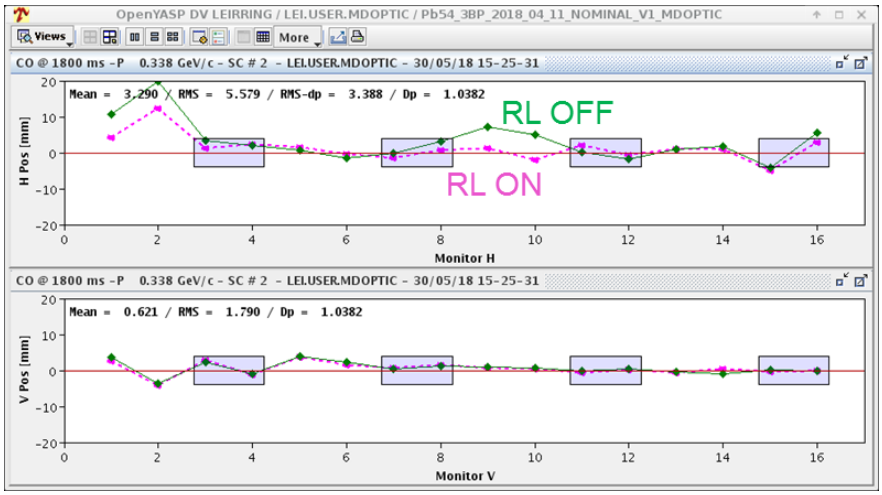

Figure 44: Difference in orbit when the radial loop (RL) is switched on/off: 6 mm drift is measured between the moment of capture and after 1.25 s.

This effect can be significantly disturbing for operation as the injection efficiency strongly depends on position and angle of the horizontal injection bump. Figure 45 shows an example of how the injection efficiencies can be *equalized* correcting for the drift on the horizontal injection bump amplitude function.

4.5 Summary and next steps

The results of the reliability run show that the new LEIR B-train system is an effective replacement of the legacy system, which will be decommissioned before the 2021 run. Among

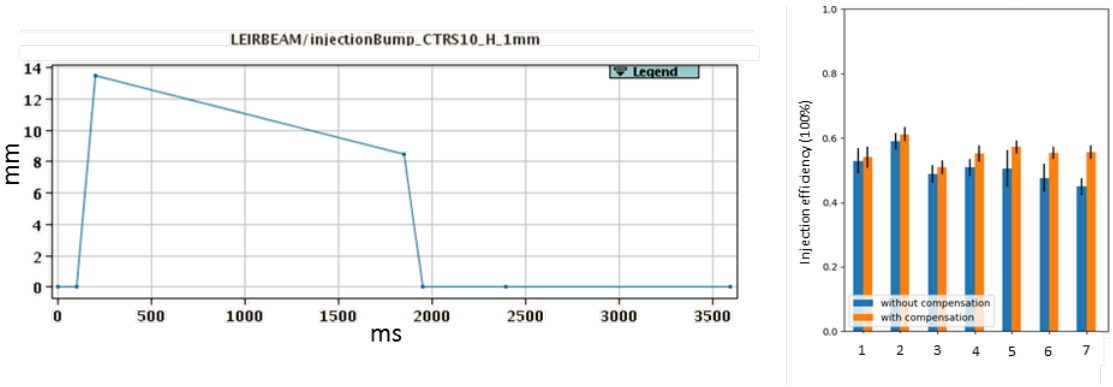

Figure 45: Effect of B field drift compensation: the horizontal injection bump is progressively decreased along the flat bottom (left) and the efficiency of the 4^{th} to 7^{th} injections is improved and made more equal to the first one.

many others, the new system offers three key improvements:

1. easily accessible measurement coils, preventing the risk associated with the only surviving legacy coil,
2. introduction of field markers to track magnetic hysteresis effects,
3. improved resolution from 10 μT to 0.2 μT.

On the down-side, the location of the sensors in the fringe field region exposes them to effects linked to eddy currents, saturation and temperature. A peak error of 1.7 mT, as derived by the amplitude of the radial loop correction neglecting any other possible contribution, is observed in the middle of the up-ramp. This error is within the correction capabilities of the radial loop by more than a factor of 2 and does not noticeably degrade appreciably the quality of the beam; however, if necessary it could be substantially reduced by adjusting the calibration of the new system so as to minimize the peak difference with respect to the legacy B-train, rather than the RMS average. Additional mitigation strategies, such as the subtraction in real-time of a correction proportional to dB/dt, could be built in a future revision of the acquisition system.

The stability of the new B-train at injection and extraction is 40 μT and 370 μT respectively, very closely comparable to that of the legacy system. Temperature has been established to play a major role, which is hardly surprising since the LEIR ring and the surrounding area are the most exposed to changing ambient conditions, among all five measured B-train systems. Even if the mechanism by which the temperature affects the measurement is not fully clarified, real-time numerical compensation may be investigated as a means to improve the stability, by more than a factor two in both cases.

The results show also a peak difference up to about 1 mT between the new operational and spare acquisition chains. Such difference can be drastically reduced by adjusting the calibration gain and offset, with the goal that the two systems should be transparently interchangeable during operation.

The next actions planned include:

- geometrical survey of the external sensor assembly over a few days (with and without magnet powering) to ascertain the extent of thermally-induced deformations,
- based on recorded data, re-calibration of the new operational system to better match the legacy, and of the new spare to match the operational,
- verification and adjustment of the final calibration according to beam behaviour during the next machine restart.

Last but not least important, a decay of the B field along the injection plateau was observed, probably induced by eddy currents in the first and last modules of the LEIR main dipoles: new probes are being installed for further diagnosis at the machine restart.

5 Beam commissioning

Three different phases can be identified during the LEIR beam commissioning: accumulation of 7 Linac 3 pulses, capture and acceleration to extraction. Each of the three phases in the operational cycle could be further divided into a series of commissioning steps which are explained in the following subsections. Figure 46 shows the typical performance of a NOMINAL beam in LEIR during 2018 operation after following the different commissioning steps.

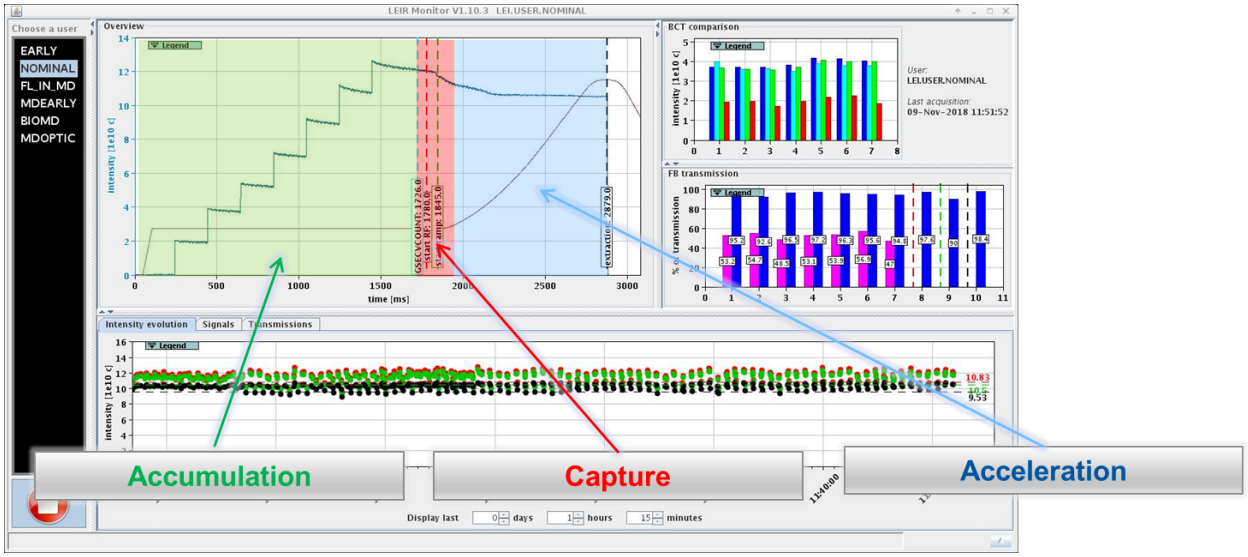

Figure 46: Typical performance of a NOMINAL cycle as observed with the LEIR Monitor application. Accumulation of 7 Linac 3 pulses, capture and acceleration to extraction phases are highlighted.

The step by step commissioning of a high intensity NOMINAL beam can be summarised as follows:

1. First injection setup (Sec. 5.1),
2. First turn (Sec. 5.2),
3. Linac 3/LEIR energy matching (Sec. 5.3),
4. Orbit correction (Sec. 5.4),
5. Acceptance optimization (Sec. 5.5),
6. Injection optimization (Sec. 5.6),
7. Orbit along the ramp (Sec. 5.7),
8. Extraction (Sec. 5.8),
9. Tune/Chromaticity setup (Sec. 5.9),

10. Cooler setup for high intensity (Sec. 5.10),
11. Accumulation (Sec. 5.11),
12. Injected pulse energy distribution optimisation (Sec. 5.12),
13. RF-modulated capture (Sec. 5.13),
14. New transfer line optics from LEIR to PS (Sec. 5.14).

5.1 First injection setup

The first step in the commissioning phase is the steering of the beam from Linac 3 to LEIR through the transfer line. In 2018 the first injection in LEIR was performed importing past settings from the 2016 $^{208}Pb^{54+}$run and optimising, with screens and SEM grids, the beam trajectory through the transfer line to be able to reproduce the reference positions and inject into the machine. For the 2021 restart, LEIR ITE to EI lines equipped with 9 BPMs, as it was shown in Fig. 4, will allow both position and pulse quality to be checked, also for low beam (4μA) current(22).

In 2018 it was, nevertheless, possible to use some of the injection BPMs of Fig. 4 during beam commissioning. Several issues due to electrode saturation (23), as explained in Sec. 2.2 prevented the BPMs from workimg in the foreseen low frequency mode. Instead, high frequency operation at 101 MHz was proved to be optimal in order to get reliable position readings of the incoming Linac 3 pulses. As shown in Fig. 7, the position traces over the 200 μs pulse can be calculated and used to steer the first beam coming from Linac 3, which is usually mono-energetic, i.e. the ramping cavity is set to a constant phase.

When the Linac 3 ramping cavity is active and the beam pulse energy increases along the 200 μs, the trace (for example in the horizontal plane from the EI.BPMI30) will look like the one reported in Fig. 47 where we can appreciate the dispersion effect due to the lower energy particles in front, and higher energy at the tail of the pulse, with respect to the average beam momentum.

This kind of behaviour is expected for other BPMs in the transfer line according to the dispersion model shown in Fig. 48. For example, for a ramping rate of $\simeq \pm 0.2\%$ the beam displacement is in agreement with $D_x = 1$ m as in the model.

In summary, with the available BPMs readings, in 2018 it was possible to reliably measure the trajectory in horizontal and vertical planes. This is shown for the 7 injections of Linac 3 in Fig. 49, and it will be used as a reference measurement for the next commissioning in 2021.

5.2 First turn

The high efficiency of the LEIR injection process relies on multi-turn injection with beam accumulation in longitudinal and transverse planes (5). The 200 μs pulse from Linac 3 is ramped from a negative offset $\Delta p/p = -2 \cdot 10^{-3}$ to a positive offset $\Delta p/p = +2 \cdot 10^{-3}$. The low energy part of the pulse comes first from the transfer line and travels on the inner circumference in the machine; the high energy part travels towards the outer circumference.

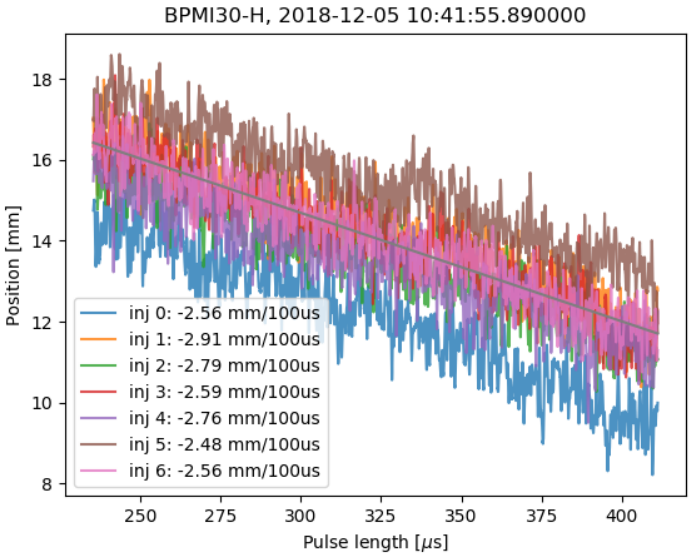

Figure 47: Horizontal position along the pulse at the EI.BPMI30 for 7 consecutive Linac 3 injections. Note the descending slope consequent to the energy ramping of Linac 3. Low energy particles are in front (right in the picture), high energy at the tail of the pulse (left in the picture).

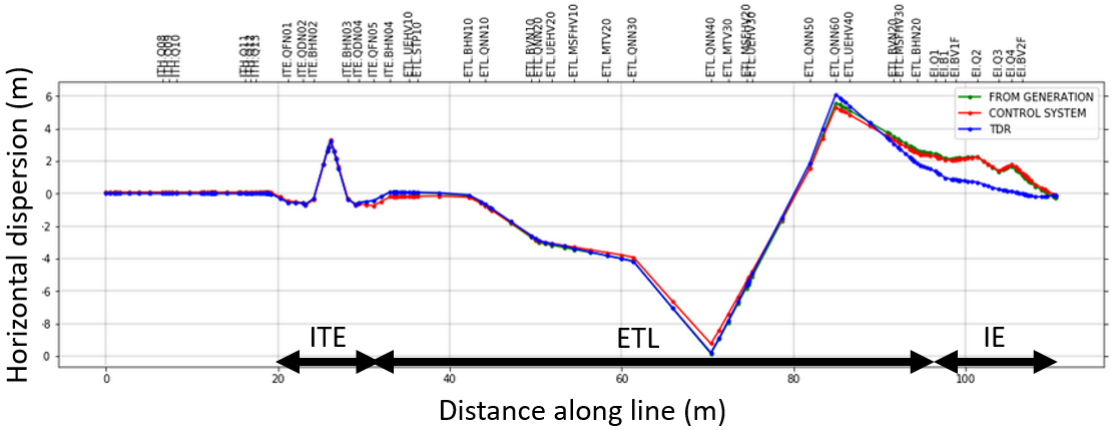

Figure 48: Dispersion along the injection line from present models (generation, control system, TDR).

Collapsing the fast injection bump (overall duration of 200 μs) allows the momentum dependent horizontal orbit of the injected beam to be kept constant during the whole injection process and minimises emittance growth (24). A schematic representation of the multi-turn injection process in the horizontal plane is shown in Fig. 50. The horizontal axis represents the 200 μs duration of the injection of a single Linac 3 pulse. The vertical axis represents the evolution of the horizontal position of the injected beam, which has an orbit given by the sum of the fast horizontal bump, x_b, and the dispersive orbit, $D_x \cdot \frac{\delta p}{p}$. The resulting orbit is x_{co} represented by a green line in the picture.

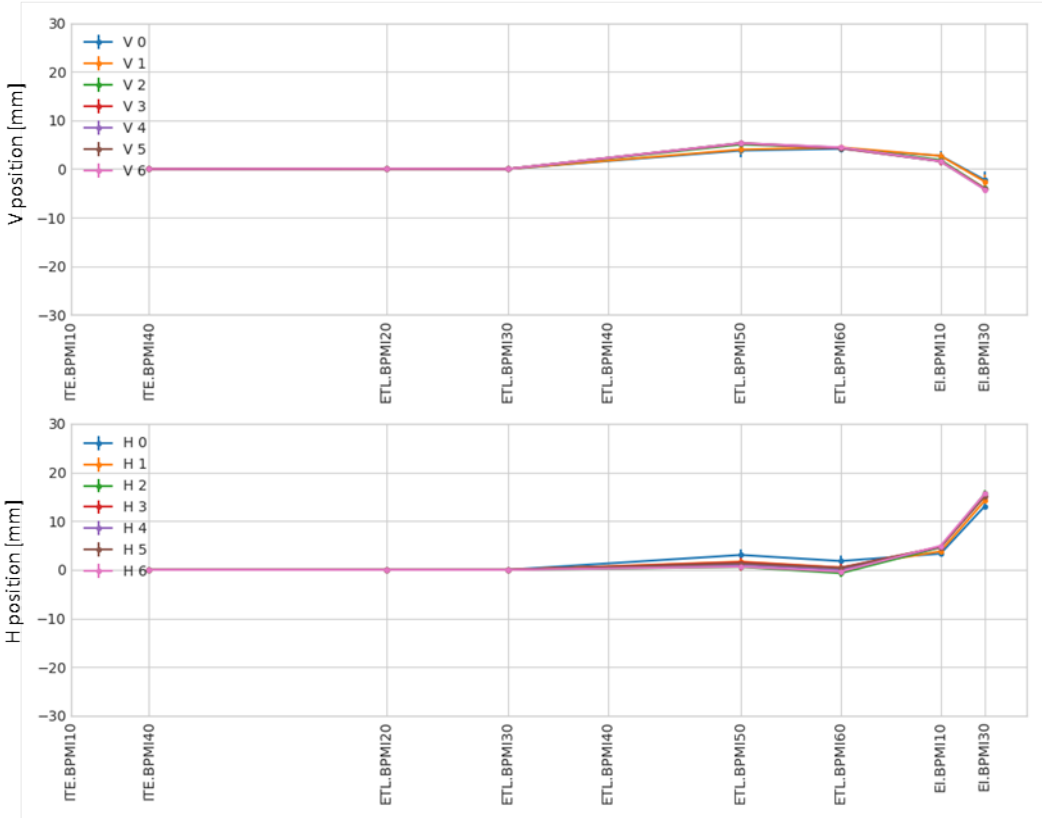

Figure 49: Horizontal and vertical trajectories along the injection line. The first three BPMs were not working and position is set to 0.

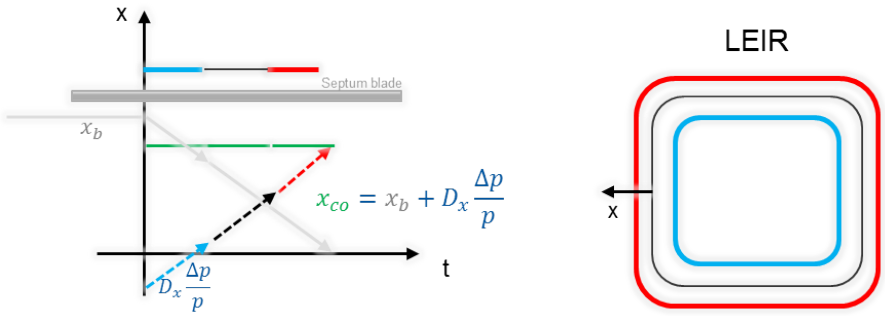

Figure 50: On the left: LEIR injection bump scheme for a Linac 3 pulse ramped from negative (blue) to positive (red) momentum error. The fast collapsing horizontal bump is located in the dispersive injection region and collapsed to maintain a constant closed orbit, x_{co}, position. On the right: orbit corresponding to particles on momentum (black) and particles with negative (blue) and positive (red) momentum error.

The injection efficiency is determined by the injected beam transverse position at the septum, the mean energy and energy spread of the Linac 3 pulse, the closed orbit injection bump settings and the transverse tunes in the machine (Q_x, Q_y). The complexity of the optimisation can be naturally handled by automatic machine parameter optimisers. Never-

theless, this cannot be done at the commissioning stage when the beam intensity is too low and the orbit in the machine is still uncorrected.

The new orbit acquisition system allows for acquisition in debunched mode, as described in Sec. 2.4.1 and shown in Fig. 12. This new mode of operation of the orbit system will be available for the first turn observation in 2021 (it was only tested at the end of 2018). It will only give indicative positions of the debunched beam passage as the signal to noise ratio is very small.

Once the beam is circulating, the fast bumpers voltage profile and fast BCT traces can be crosschecked in OASIS as shown in Fig. 51. The OASIS monitoring is often useful to crosscheck eventual mis-functioning of the injection fast bumpers that should exhibit a function of equal magnitude and time duration.

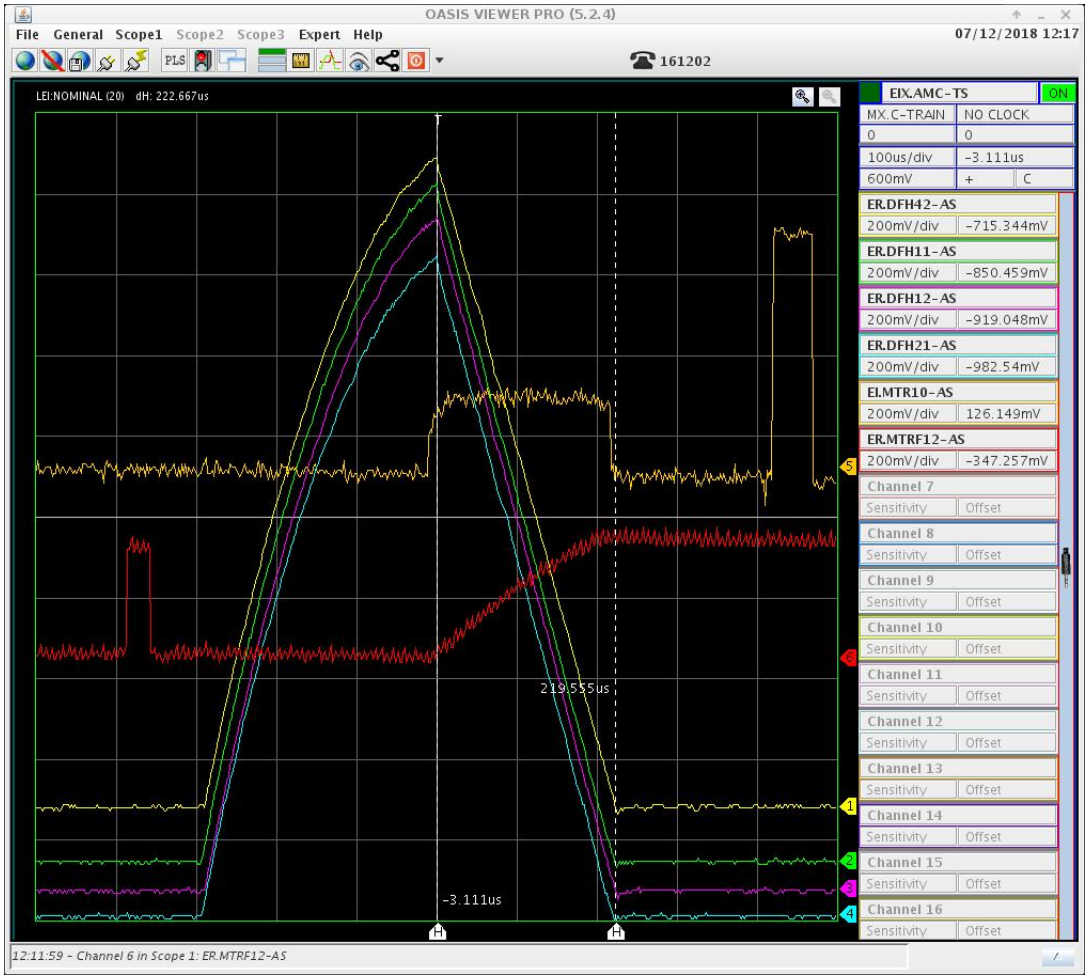

Figure 51: Injection fast bumpers voltage function along the injected pulse (4 triangular curves) together with the transfer line BCT (EI.MTR10, in yellow) and the ring fast BCT (ER.MTRF12, in red).

5.3 Linac 3/LEIR energy matching

5.3.1 Initial Linac 3 setup

As already mentioned, the energy distribution along the Linac 3 pulse is one of the most important ingredients determining the LEIR injection efficiency. All the RF components of Linac 3 and the stripper foil performance (as there is a significant energy loss of the ions when traversing the stripper foil) contribute to the profile of the pulse. The layout of the filter region with Tank 3, ramping and debunching cavities highlighted in blue is shown in Fig. 52.

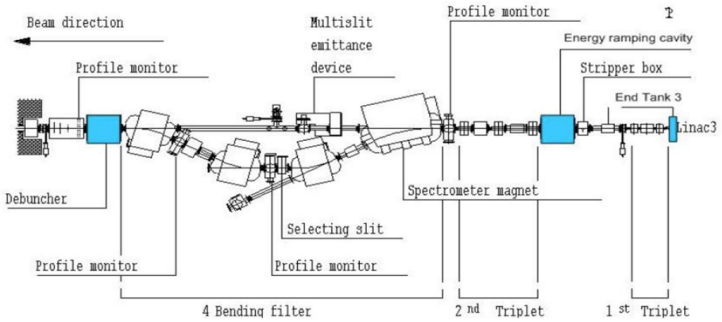

Figure 52: Schematic layout of the filter region, ITF, with Tank 3, ramping/debunching cavities highlighted in blue.

At the beginning, the ramping cavity is set up by making a scan of the cavity phase, while keeping the amplitude constant, and measuring the central momentum variation of the beam using the ITF line. Figure 53 shows the comparison of the 2018 start up against the same measurements in 2015 and 2016. In addition a value for the beam momentum width (green trace in arbitrary units) is shown to verify which of the zero-crossing phases corresponds to the longitudinal focusing phase. The amplitude of the momentum change confirms the cavity amplitude. This method shows that the phase relationship between the beam emerging from Tank 3, and the ramping cavity is the same as the previous year.

The cavity peak voltage gain is calculated from

$$V_{RC} = \frac{2E}{q}\left(\frac{\Delta B}{B}\right)_{max}, \tag{19}$$

where E is the kinetic energy (as $\beta \sim 0.1$ is very low), q the elementary charge, and $\Delta B/B_{max}$ is the amplitude of the sine wave of the magnetic field B of magnet ITF.BHZ11, that centres the beam on the SEMGrid, when changing the ramping cavity phase. In 2018 the following settings were found: $V_{RC} = 195$ kV corresponding to an amplitude setting of 6030 in the working-set.

The debuncher uses a similar technique using the LBS line, but the extended bunch length by the debuncher cavity makes it more difficult to find the mean momentum for some settings. As we cannot easily work out the sine wave amplitude, we should use the gradient at the zero crossing and apply $d(\Delta B/B)/d\phi$ where B is the magnetic field of LBS.BVT10 that centres the beam on the SEMGrid, and ϕ is the cavity phase in radians. Measurements

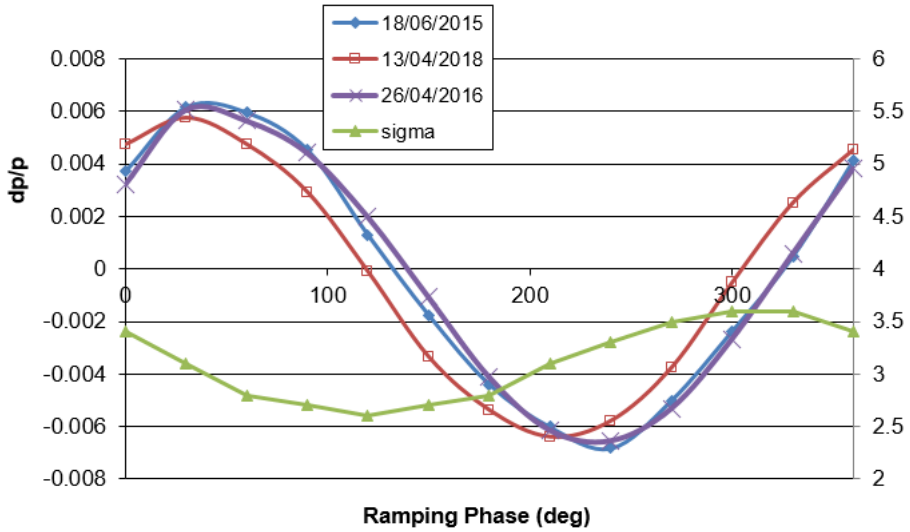

Figure 53: Momentum change of the beam as a function of the setting phase of the RF cavity.

in April 2018 led to a debuncher voltage of $V_{DC} = 113$ kV corresponding to an amplitude setting of 5500 in the working-set.

The setting up of the injection process into LEIR proceeds using the previous years settings of the ramping and debuncher RF (corrected if necessary with the result of the calibration). The two above setup procedures only confirm that the phase and amplitudes are the same as the previous year. While optimizing the EARLY beam injection process, these settings can be run through an optimization process with the help of automatic optimizers as described in Sec. 5.12.

5.3.2 Energy matching in LEIR

Once the beam circulates, the Schottky monitor can be used to check the mean energy of the injected beam, even with low intensity. A simulated Schottky spectrum is shown in Fig. 54 showing on the left the full Schottky spectrum up to the 120^{th} revolution harmonic and, on the right, few selected harmonics (25): as a trade off between signal to noise ratio and bandwidth (which translates directly in signal acquisition time), the 100^{th} harmonic at $\simeq 36$ MHz has been chosen.

The effect of Linac 3 energy ramping is shown in Fig. 55: between the top and bottom picture the energy ramping has been switched on. While in the first picture (top), one can probe the mean momentum deviation and compare it to the nominal value; in the second one (bottom), one can appreciate how large the momentum spread of the injected beam is.

Once the electron cooler is on, the ion beam mean energy (i.e. velocity) is dragged to the electrons mean velocity. For a NOMINAL beam, the electron cooler is set-up such the electron beam velocity is around 2 per mill smaller than the ion beam velocity for a nominal electron current of 335 mA. To achieve these parameters the corresponding control, grid and gun voltages are listed in Tab. 8. It is important to stress that the cooler performance strongly depends on the overlap of the ion and electron beams (see also Sec. 5.10). For a

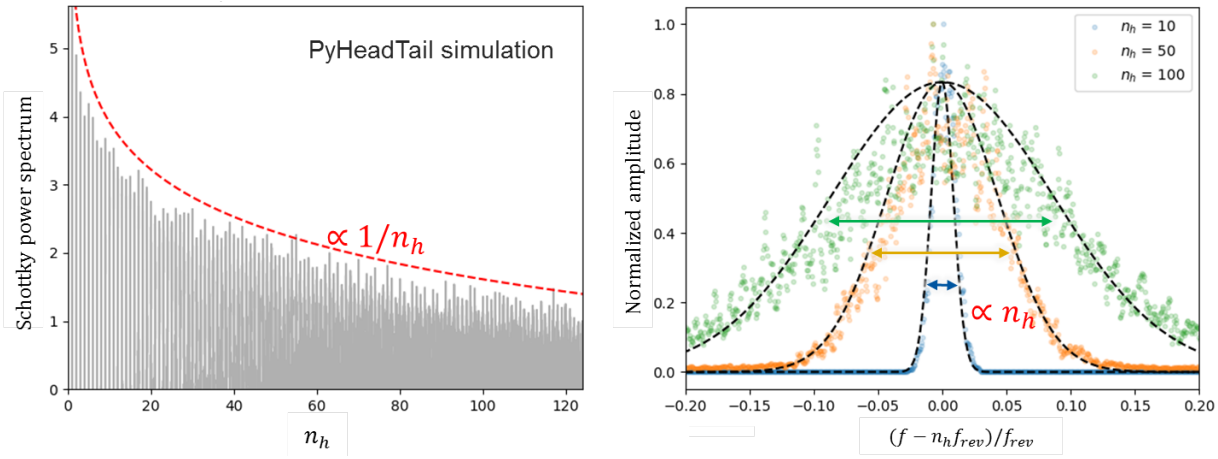

Figure 54: On the left, simulated Schottky spectrum with LEIR parameters in PyHEADTAIL for coasting beams. On the right, the zoomed view at the 10^{th}, 50^{th} and 100^{th} revolution harmonics.

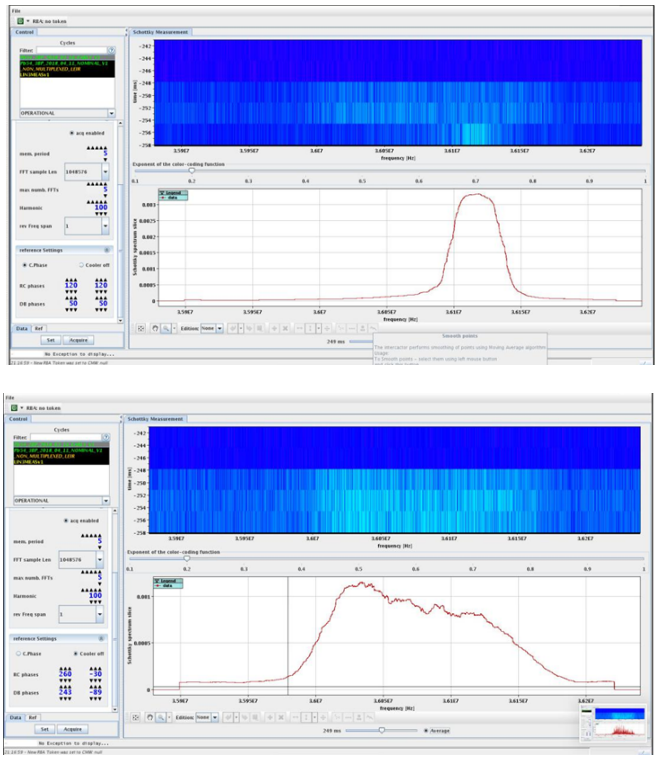

Figure 55: Schottky spectrum of the first injection into LEIR at the 100^{th} revolution harmonic respectively: at the top, without ramping and cooling, at the bottom, with ramping and without cooling.

machine in commissioning stage, especially with low accumulated intensity, the orbit at the cooler might be unknown and the cooling performance difficult to assess.

Parameter	Value
V_{co}	480 V
V_{gr}	1550 V
V_{gun}	2588 V

Table 8: Values of the voltage applied to the control (V_{co}), grid (V_{gr}) and gun (V_{gun}) of the electron cooler for a NOMINAL cycle.

5.4 Orbit correction

One of the most important steps in order to commission a high intensity NOMINAL beam is the correction of the orbit. To decouple from the complex injection bump gymnastics, we can split the injection plateau in two segments, changing the corresponding makerules used by YASP (Fig. 56). The capture needs to be advanced as well in order to use the orbit system for which a bunched beam is needed.

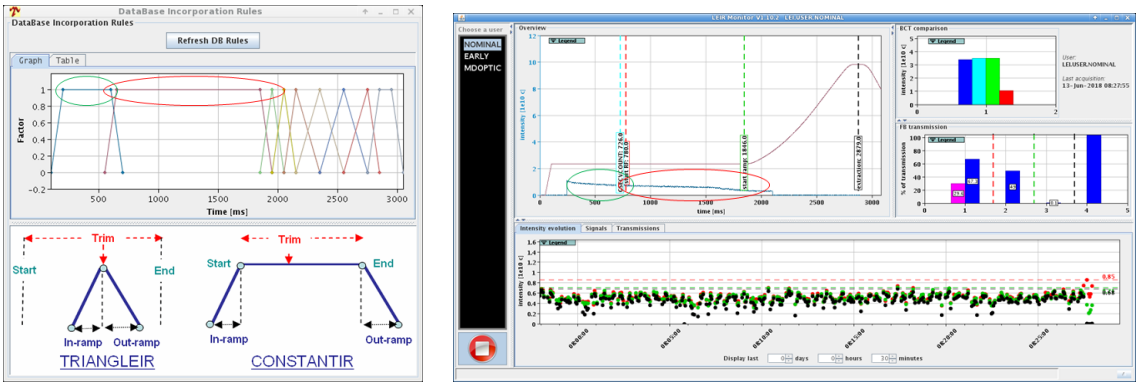

Figure 56: On the left, the modified makerule to disentangle the corrections needed for the injection process optimization; on the right, the corresponding times in the LEIR accumulation plateau as seen from the LEIR Monitor application. The green circle indicates the cycle segment devoted to the injection optimization; the red circle indicates the part of the injection plateau where the closed orbit will be optimized.

The radial loop pickups, UEH31 and UEH32, are highlighted in Fig. 57. Once the beam is captured, the revolution frequency of the beam is given by the RF system and if the beam is captured off-momentum a large error might be seen at the radial loop pickups. This error can be minimized changing the B-Train value received by the RF with the ER.TRAIN/CCV parameter (27217 for a lead NOMINAL cycle in 2018). As an example, Fig. 58 shows the effect of this correction on the revolution frequency immediately after capture.

At this point the orbit can be considered sufficiently on momentum to perform a bare correction using YASP to further reduce dipole errors. As at the radial loop pickups there is no distinction between orbit distortion due to dipole errors or off-momentum, further optimization of the B-Train settings might be needed as shown in Fig. 58.

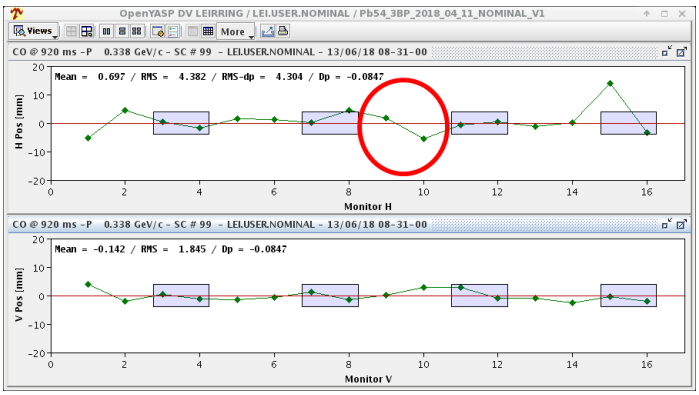

Figure 57: Uncorrected orbit at LEIR injection. The radial loop pickups UEH31 and UEH32 are highlighted.

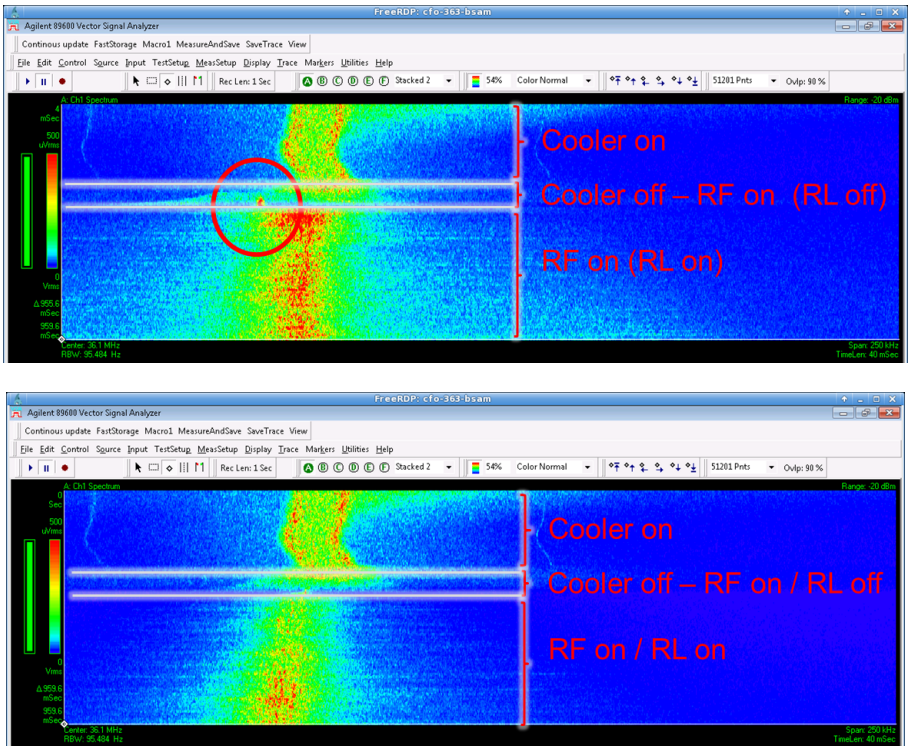

Figure 58: Schottky spectrum of the capture process without (top) and with (bottom) B-Train correction. The red circle in the picture indicates the frequency of the off-momentum captured beam. After applying the necessary correction to the ER.TRAIN/CCV parameter, the beam is clearly captured on-momentum at the bottom picture.

5.5 Momentum acceptance optimization

The LEIR multi-turn injection scheme accommodates the ± 0.2% energy spread of the Linac 3 pulse by means of a large injection bump. The stacked (mono-energetic) beam needs to be lowered in energy as it would be scraped during the injection bump process if placed at the same momentum as the injected beam. This is achieved by further energy dragging by -0.1% with the electron cooler. The momentum acceptance needs to be maximized, centering

the machine working point on the frequency given by the RF. The injected beam can be put slightly off momentum with respect to RF capture frequency (+0.1% mean momentum) trimming the machine $(B\rho)_{inj}$ (see also Sec. 2.7). A schematic illustration of the process is shown in Fig. 59, while Fig. 60 shows the actual implementation in the machine (on the left the dragging of the stacked beam, on the right the beam dragged back to allow centered capture): the RF frequency is centered at 36.047 MHz (considering the 100^{th} revolution frequency seen at the Schottky monitor), the mean of the injected beam is at 36.083 MHz (i.e. 0.1% higher momentum), the center of the stacked beam is at 36.01 MHz (i.e. -0.1%).

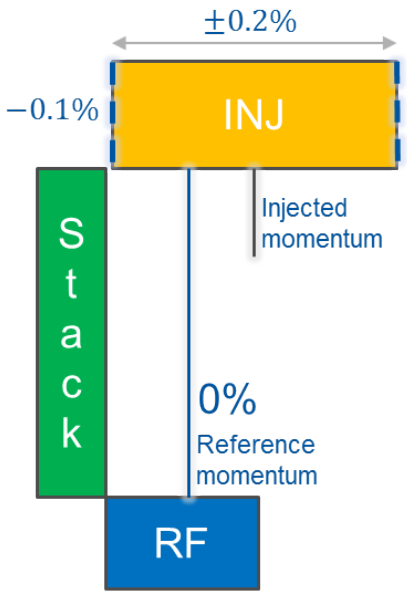

Figure 59: A schematic illustration of the momentum acceptance optimization: the cooled beam (green) experiences an energy dragging by -0.1% with respect to the central frequency, while the injected beam (yellow) is put slightly off momentum with (+0.1%) trimming the machine $(B\rho)_{inj}$.

The final dragging to the frequency expected by the RF can be adjusted by modifying the electron cooler gun voltage. As shown in Fig. 61, higher (lower) voltage increases (decreases) the beam mean frequency.

5.6 Injection optimization

At this point, we can aim for more intensity injected into the ring. This can be efficiently achieved by running the optimizer on the injection line (ETL/EI) and/or the injection bump optimizer (see also Sec. 2.1 for further details): the first will correct the deflection angle given by the ETL.BHN10 corrector which was found to be very efficient in order to steer the trajectory in the injection line to improve the injection efficiency in LEIR; the second will iteratively change the transverse injection bump in order to optimize (x, x', y, y') at the injection septum against the target of the injected intensity into LEIR. An example of the performance of the tool in these two different cases were shown in Fig. 2. In a similar way to the injection bump, it is possible to optimize the EI correctors strength.

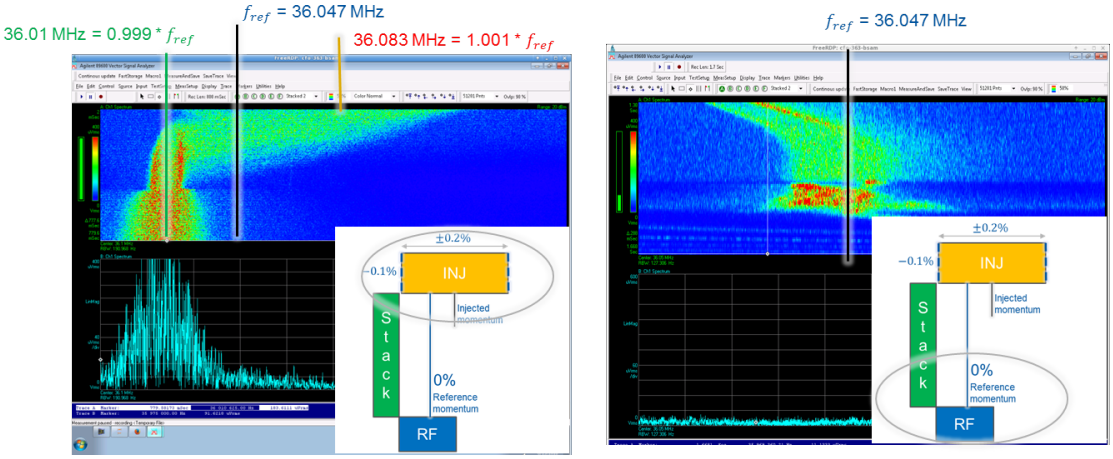

Figure 60: On the left the dragging of the injected beam, on the right the beam dragged back to allow centered capture.

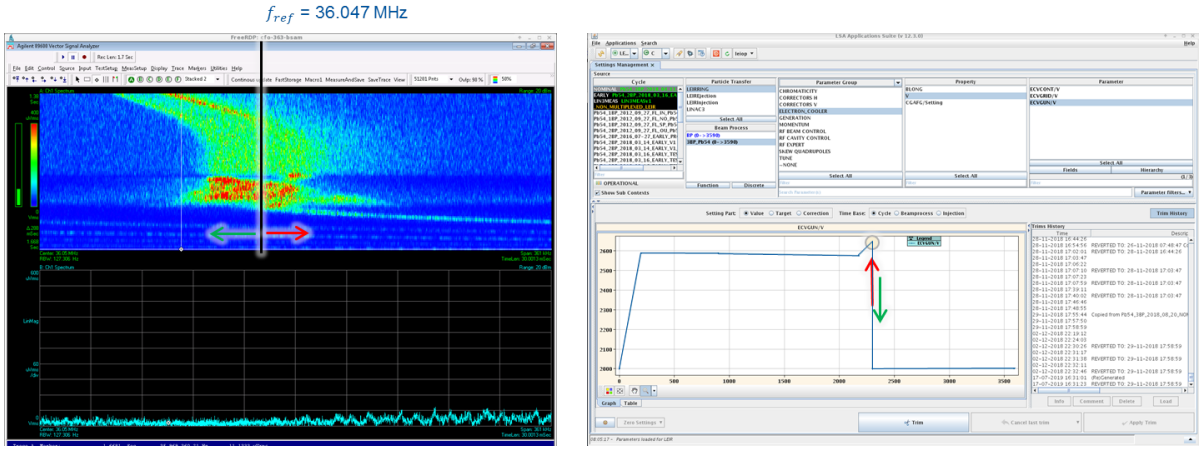

Figure 61: On the left the dragging of the stacked beam towards the RF, on the right the corresponding adjustment of the gun voltage to center the frequency to the one expected by the RF.

With this process, very high injection efficiency was obtained. As shown in Fig. 3, an injection efficiency even above 80% could be obtained, proving the operational importance of the optimization tools.

5.7 Orbit along the ramp

Once the injection efficiency is good enough and the orbit along the injection plateau is sufficiently flat (with exception of the injection bump of course), the orbit along the ramp can be optimized using the skeleton points already available in YASP (see Fig. 56) or adding new ones according to the position in the cycle to be corrected.

Figure 62 shows an example of horizontal and vertical orbits (mean and rms values) together with the deduced momentum deviation from YASP.

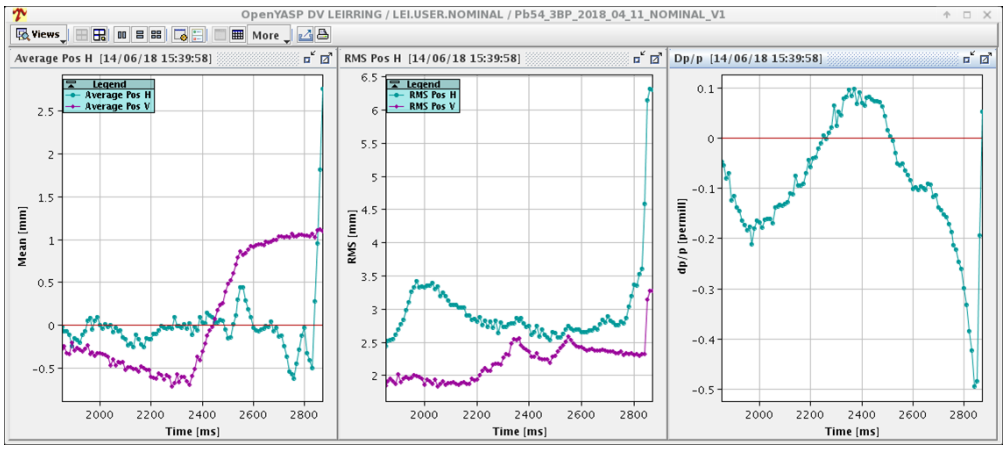

Figure 62: Orbit along the ramp after corrections with YASP.

5.8 Extraction

In order to extract the beam from LEIR, three independent kicker modules are available to kick the beam towards the extraction septum SMH40. The extraction bump can be optimized together with the ETL/ETP lines to extract the beam towards the PS. Figure 63 shows the orbit before extraction: one can note also the extraction bump in straight section 4.

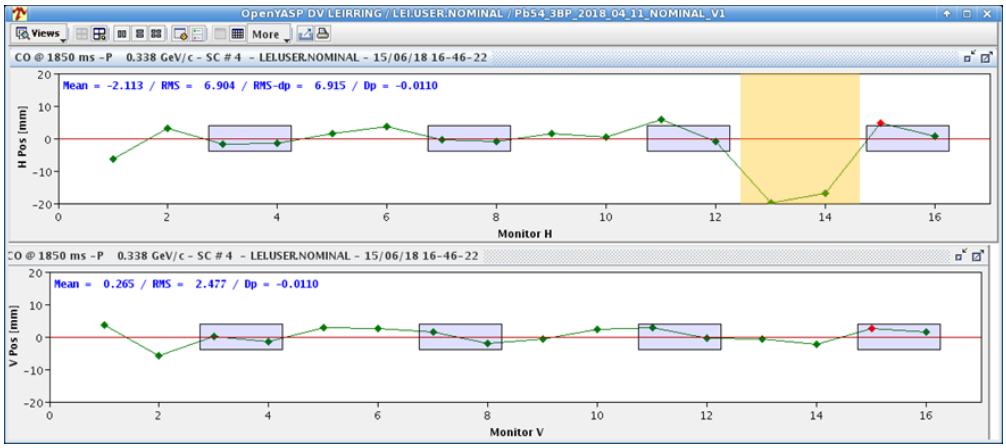

Figure 63: Orbit measured at 2875 ms (i.e. before extraction) with highlighted bump in straight section 4. Note the 4^{th} vertical BPM, the UEV14, was faulty.

5.9 Tune/Chromaticity setup

Using the "Qmeter" and "AutoQ" applications it is possible to correct the tunes to be flat along the cycle at their nominal value (Q_x, Q_y)=(1.82, 2.72) as shown, for example, in Fig. 64 for the vertical plane.

The chromaticity correction is a bit more involved, as the beam needs to be bunched to allow for radial steering. Typically this process was accomplished by advancing the capture

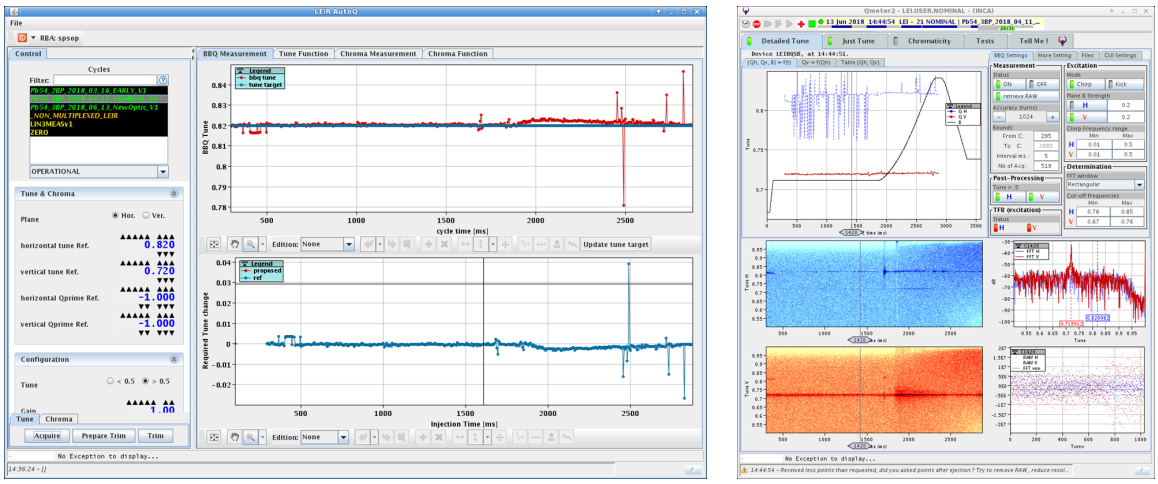

Figure 64: On the left, the AutoQ application, on the right, the corresponding Qmeter measurement after correction in the vertical plane.

and correcting the injection plateau and the ramp separately. Figure 65 shows the result for two different moments in the cycle. The chromaticity is corrected to -1 unit in both planes (the machine operates below transition).

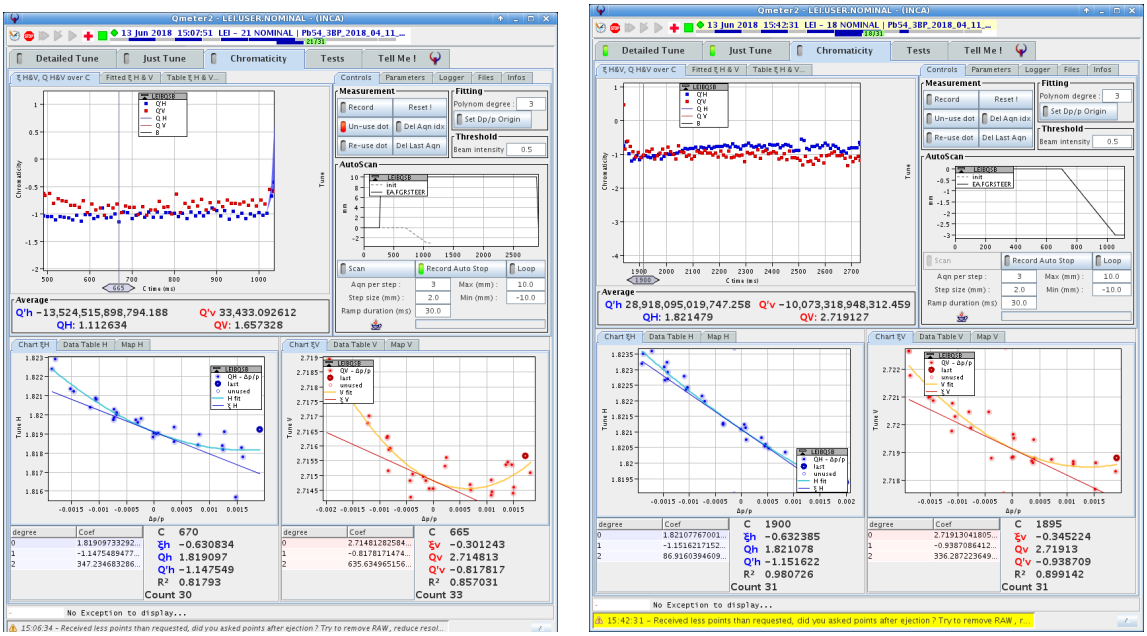

Figure 65: An example of the measured vertical and horizontal chromaticities from 500 ms to 1000 ms (left), from 1900 ms to 2700 ms (right).

5.10 Cooler setup for high intensity

In order to allow for better lifetime and stability margins, the final cooled emittance can be adjusted by changing the orbit bump in the cooler. From the cooling maps performed in 2018/2019 (26), it was observed that the beam experiences maximum cooling when displaced with a flat horizontal offset of 10 mm in the cooler section.

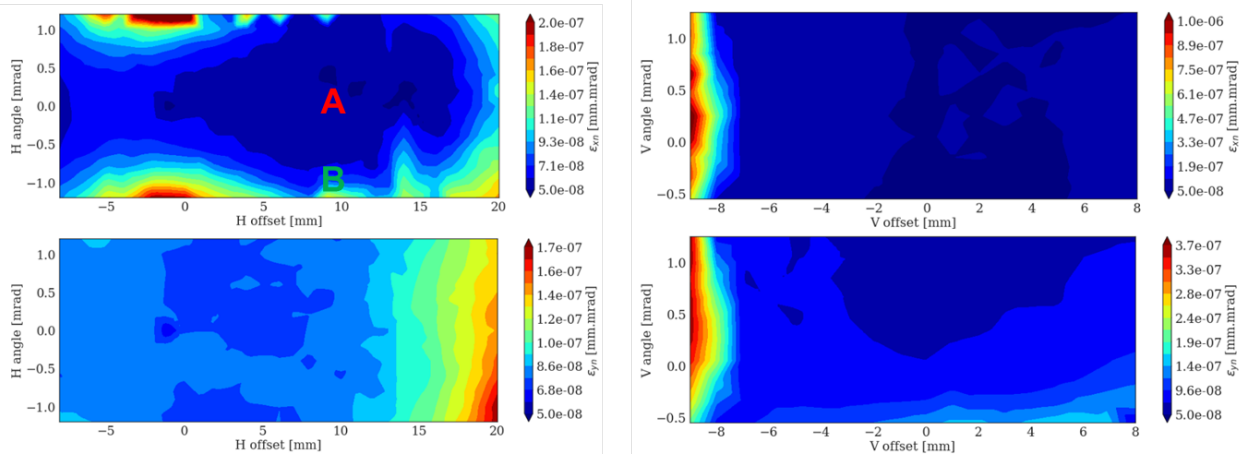

Figure 66: Example of horizontal and vertical cooling maps: the horizontal final emittance is plotted for each (x, x') position on the top left, and for each (y, y') on the top right; the vertical final emittance is plotted for each (x, x') position on the bottom left, and for each (y, y') on the bottom right. A minimum horizontal emittance at x =10 mm, x' =0 mrad is obtained (point A), while the vertical optimum seems wider around y =0 mm, y' =0 mrad.

For example, Fig. 66 shows on the top the horizontal cooling maps obtained for $y = 0$ mm, $y' = 0$ mrad: the horizontal and vertical final emittances (i.e. after cooling) are plotted for each (x, x') position (plots on the left). The minimum horizontal emittance (or, conversely, the maximum cooling effect) occurs at $x = 10$ mm, $x' = 0$ mrad while there is no relevant impact on the vertical emittance. On the other hand, there seems to be a large optimum around $y = 0$ mm and y' slightly positive for the vertical emittance (plots on the right) while keeping $x = 10$ mm, $x' = 0$ mrad.

For stability and lifetime reasons, the maximum cooling, point A in Fig. 66, does not necessarily corresponds to the best operational setting as a small beam size implies large space charge tune shift and small stability margins in longitudinal and transverse planes. The best working point has been found for point B of Fig. 66, i.e. at $x = 10$ mm, $x' = -1$ mrad. A more detailed discussion is given in Sec. 6.6.

5.11 Accumulation

So far, the steps of the NOMINAL beam commissioning have been done with a single injection. In order to accumulate higher intensity, up to 7 injections spaced by 200 ms can be requested from Linac 3 during the injection plateau. Due to the larger intensity in the machine, additional corrections might be needed.

For example, the tune shift versus intensity in coasting beam is expected to be as large as $\simeq 3 \cdot 10^{-4}$ for 10^{10} charges (27).

As shown in Fig. 66, trimming the horizontal angle of the bump in the cooler section changes the final emittance of the beam to allow for larger stability margins and better lifetime.

5.12 Injected pulse energy distribution optimisation

Injection efficiency largely depends also on the beam energy distribution coming from Linac 3. A large mean energy error or large energy tails can potentially give losses due to LEIR momentum acceptance. The distribution can be optimized looking at the last RF stages in Linac 3 shown in Fig. 52: Tank 3 mainly defines the Linac 3 mean output energy, while the ramping and debunching cavities mainly define the energy spread along the injected pulse.

The new Schottky FESA class and automatic optimizers can bring large potential for both, energy distribution optimization and monitoring versus time. An example of the use of the new FESA class is shown in Fig. 67 where a relative phase scan is performed between ramping and debunching cavities. The observed momentum variation complements the one done in the setup phase by the Linac 3 team (see Fig. 53) and allows optimization of the momentum distribution to improve the machine injection efficiency.

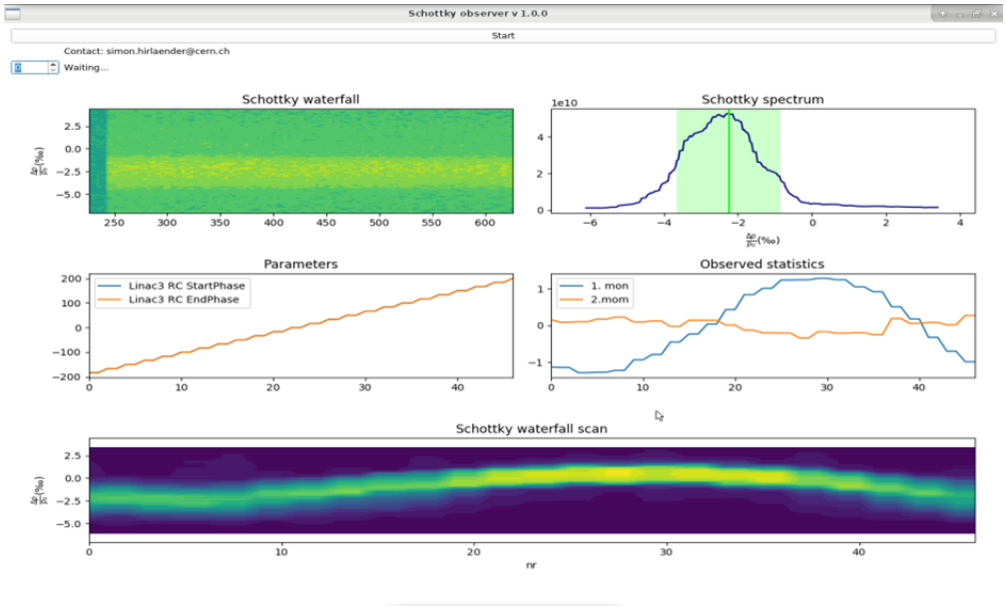

Figure 67: Ramping cavity start and end phase scan. Top left: first injection of an EARLY like beam without electron cooling. Top right: averaged momentum distribution. Center left: phase scan steps. Center right: mean and standard deviations for the different scan values. Bottom: relative error momentum distribution for the different scan values.

5.13 RF-Modulated capture

The space charge tune shift in LEIR can be as large as 0.01 for a NOMINAL beam at $9 \cdot 10^{10}$ charges with a transverse emittance of 0.2 μm (assuming round beam). This large tune shift can bring the working point towards lattice resonances or space charge induced

resonances due to lattice periodicity. While the tune shift can be mitigated acting on the electron/ions overlapping, which determines the final properties of the cooled ion beam, at the moment of capture, significant losses can occur if the line density is not flat enough. As can be seen in Fig. 68, capture in single harmonic h=2 (red and green intensity distributions and tomoscope figures) would give rise to almost 50% beam losses, whereas a flatter capture in h=2+4 (blue) allows achieving a bunching factor of 0.57 substantially reducing the beam losses (28). In order to fill the longitudinal acceptance of the bucket as much as possible, a modulation in frequency and amplitude on the revolution frequency correction has been put in place. The main parameters can be set through LSA via the trim editor for the RF BEAM CONTROL parameter group or through the working-set via the functions EA.FGMODAMPLI and EA.FGMODFREQ. During LS2, part of the LLRF settings will be moved to be better integrated into LSA (29).

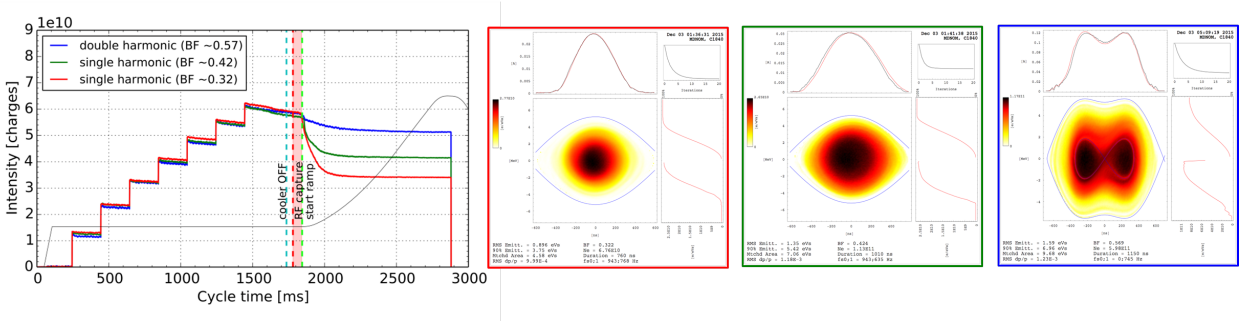

Figure 68: Capture loss dependence on the line density in LEIR. The first two cases, in red and green, are for single harmonic h=2, the last one, in blue, is for double harmonic h=2+4.

Further reduction of the peak line density can be achieved by modifying the longitudinal distribution of the beam. In principle it is possible to capture the beam with an offset between the average energy of the beam and the center of the bucket producing a flat profile and a distribution that is hollow in phase space as shown in Fig. 69. A hollow distribution is effective at reducing the impact of space charge, however it requires very good knowledge of the coasting beam revolution frequency and is sensitive to small variations from cycle to cycle.

Modulating the RF frequency during the capture process causes the bucket to be swept repeatedly through the coasting beam, whilst the voltage is being increased. This has two effects, first the energy spread of the coasting beam is increased and the bucket is uniformly filled as it passes through. The resulting longitudinal beam distribution can be seen in Fig. 70. Second, the sensitivity to small frequency variations is effectively removed (30). Therefore, the reproducibility of the beam is significantly improved and the transmission can also be increased as shown in Fig. 71.

5.14 New transfer line optics from LEIR to PS

In 2015-2016 it was noticed that the trajectory correction along the transfer line from LEIR to PS was difficult if based on the LSA on-line optics model used by YASP. Despite this, 100% transmission efficiencies were obtained. After some investigation, it was found that the

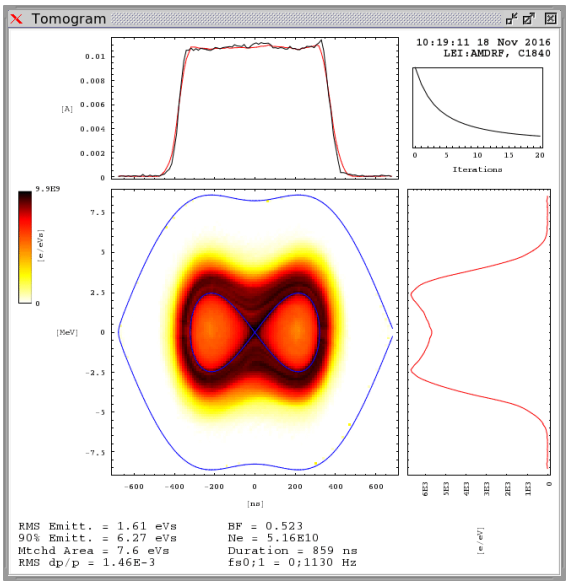

Figure 69: Hollow longitudinal beam distribution produced by offsetting the RF frequency from the coasting beam revolution frequency.

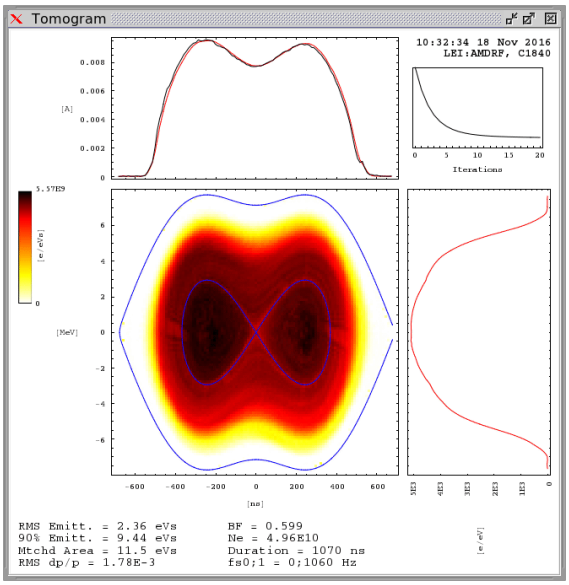

Figure 70: A conventional but large distribution, produced by modulating the RF frequency during the capture process.

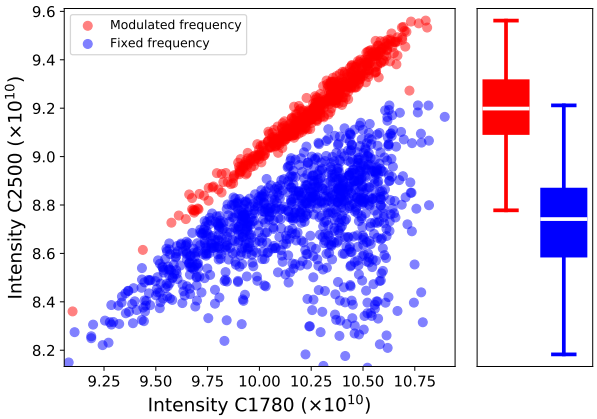

Figure 71: Comparison of the transmission with the hollow distribution and a conventional distribution produced by frequency modulation.

on-line optics model of the line was similar to the design but not matched to the PS periodic solution, as shown in Fig. 72. Additionally, the compensation of the PS main magnet fringe field, extensively studied during the design phase, was not present in the on-line optics. Figure 73 shows the layout of the PS main magnet and the transfer line beam pipe in ETP. The beam pipe, when approaching the injection septum, goes very close to one of the main PS magnets, and even enters inside. The fringe fields generated by the main magnet have a clear influence in the trajectory of the incoming beam. Two solutions were obtained at the beginning of 2000 for the fringe field compensation (31; 32), both giving similar results.

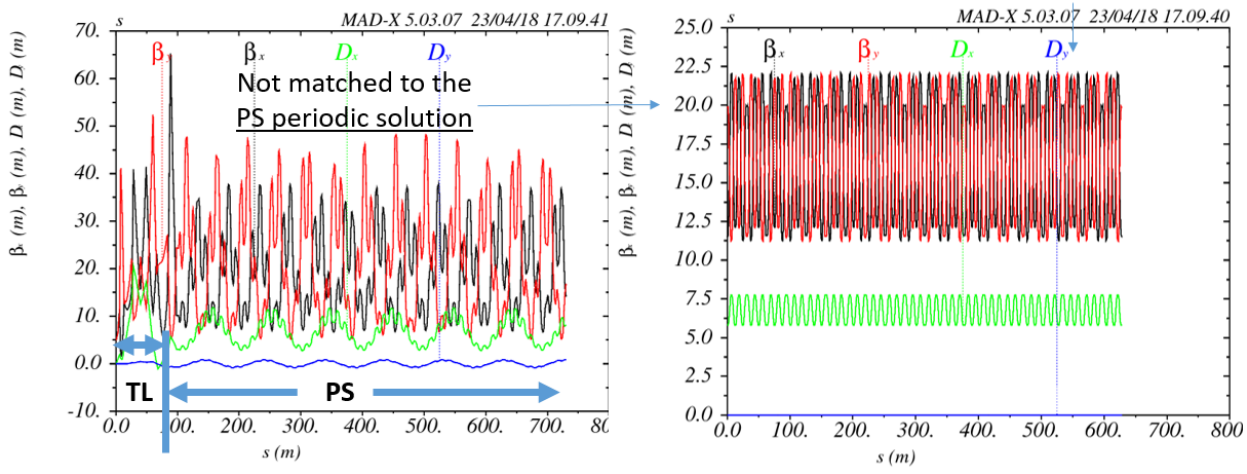

Figure 72: Left: old transfer line optics, not matched to the PS periodic solution and without the fringe field compensation matrix. Right: PS periodic solution.

In order to come out with a new optics for the transfer line matched to the PS periodic solution and including the fringe field compensation, the implementation from (31) has been

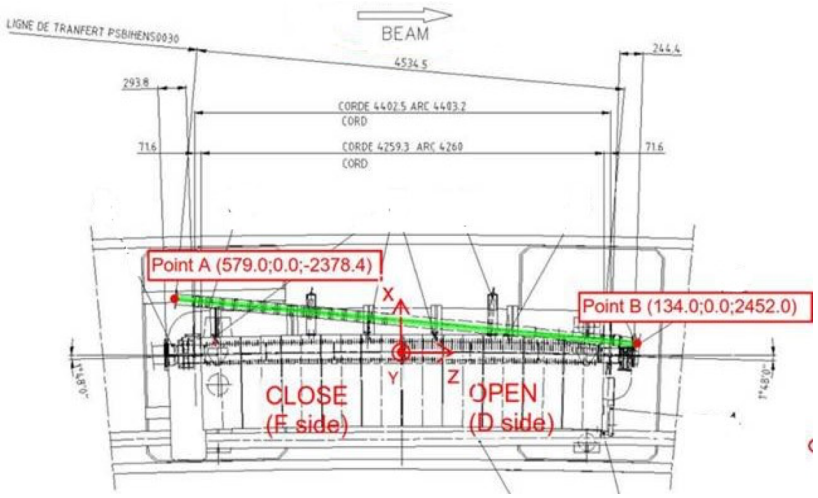

Figure 73: Layout of the PS main magnet and the transfer line beam pipe in ETP. The beam pipe (green line) when approaching the injection septum goes very close to one of the main PS magnets, and even enters inside. The fringe fields generated by the PS main magnet have a clear influence in the trajectory of the incoming beam.

used. The matrix is the following:

$$M_H = \begin{bmatrix} 1.125 & 6.534 & 0.022 \\ 0.0503 & 1.181 & 0.008 \\ 0 & 0 & 1 \end{bmatrix}, M_V = \begin{bmatrix} 0.878 & 5.683 & 0 \\ -0.049 & 0.825 & 0 \\ 0 & 0 & 1 \end{bmatrix} \tag{20}$$

Using the design drawings, a position for this matrix was calculated and inserted in the transfer line sequence and elements of the engineering files of MAD-X. MAD-X was further used to match the transfer line optics to the PS periodic solution. The Twiss parameters of the matching points are given in Tab. 9.

	LEIR-PS matching point	PS septum 26 centre
$\beta_{x,y}$ (m)	20, 14.8	11.47, 19.83
$\alpha_{x,y}$	1.35, -0.57	0, 0
$D_{x,y}$ (m)	2.5, 0	2.16, 0
$D'_{x,y}$	-0.12, 0	-0.02, 0

Table 9: Twiss parameters at the matching points around the fringe field matrix.

The beta and dispersion functions for the new optics are shown in Fig. 74. The matched solution to the PS is shown in Fig. 75, together with the beta beat of the resulting PS beta function, ±2% in horizontal and ±4% in vertical. The horizontal and vertical beam sizes and apertures are presented in Fig. 76 and Fig. 77 respectively, and compared with the design optics presented in (5).

In 2018 the steering of the line from LEIR to PS was done using the new optics. 100% transmission efficiency was obtained and deterministic corrections were achieved: the injection efficiency into the PS was, however, limited to 95%, while 100% was the target because

this had been obtained with the old optics. PS injection bumps scans were performed but it was not possible to bring the injection efficiency to the target. A possible explanation could be a different calibration of the PS Beam Current Transformer as compared to previous years.

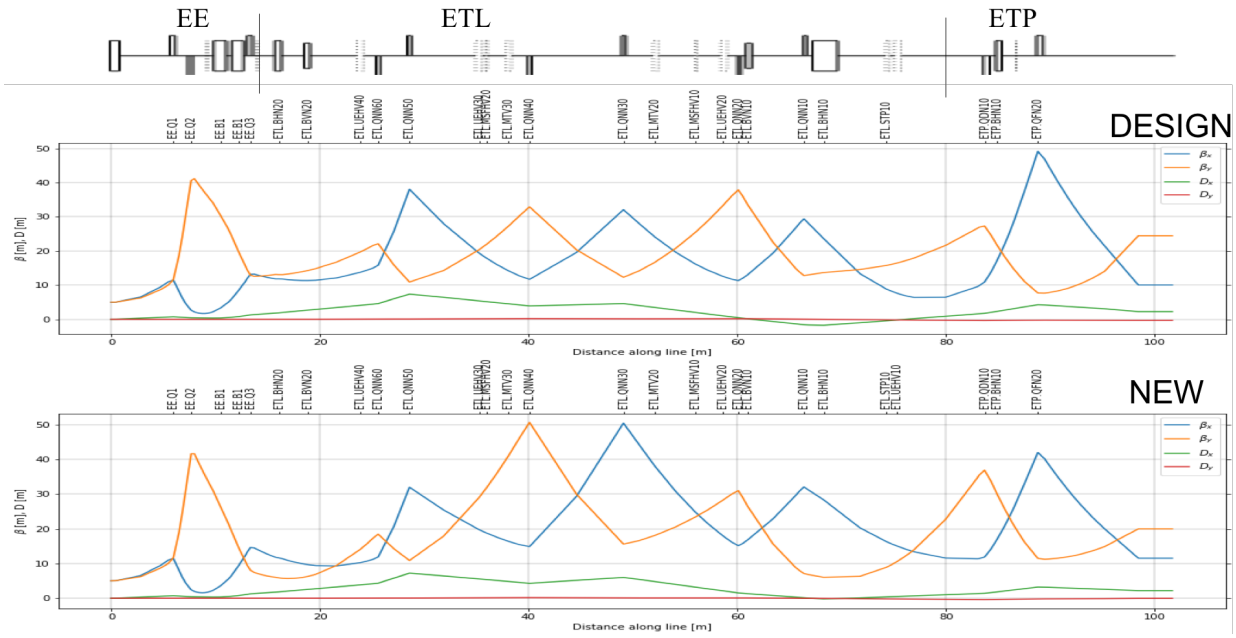

Figure 74: Horizontal (blue) and vertical (orange) beta functions and horizontal (green) and vertical (red) dispersion functions for the new optics along the transfer line from LEIR to PS. Top: optics functions as published in (5). Bottom: solution obtained from the 2018 studies.

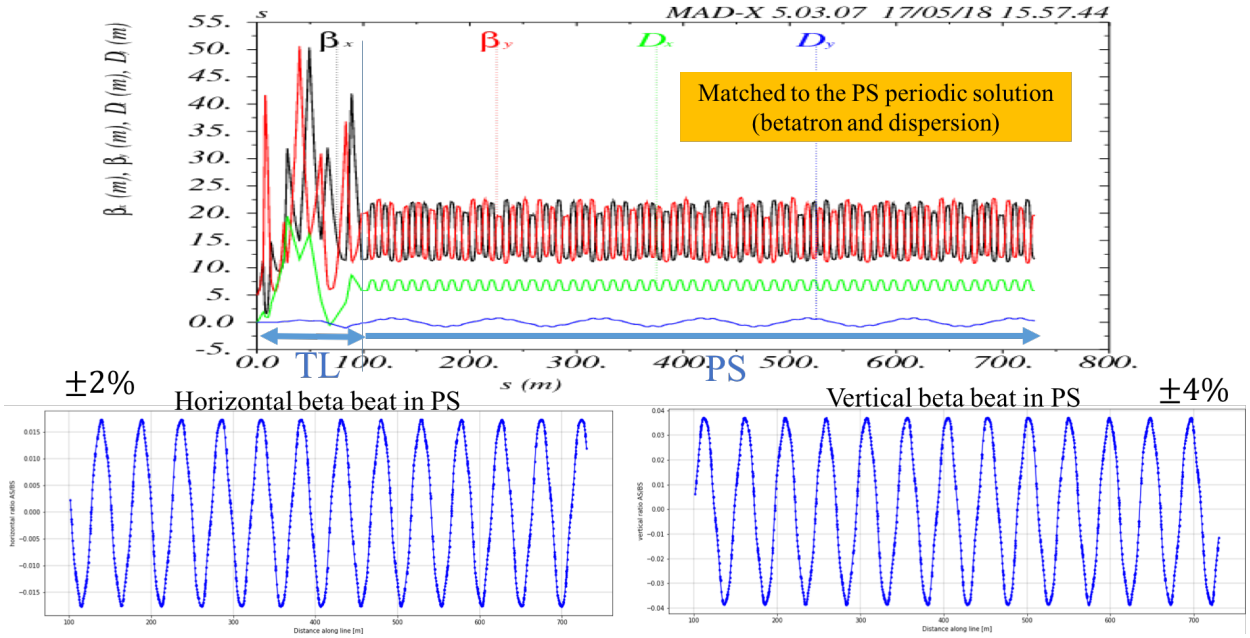

Figure 75: Beta and dispersion functions along the transfer line and PS ring. The bottom plots show the PS beta beating after matching.

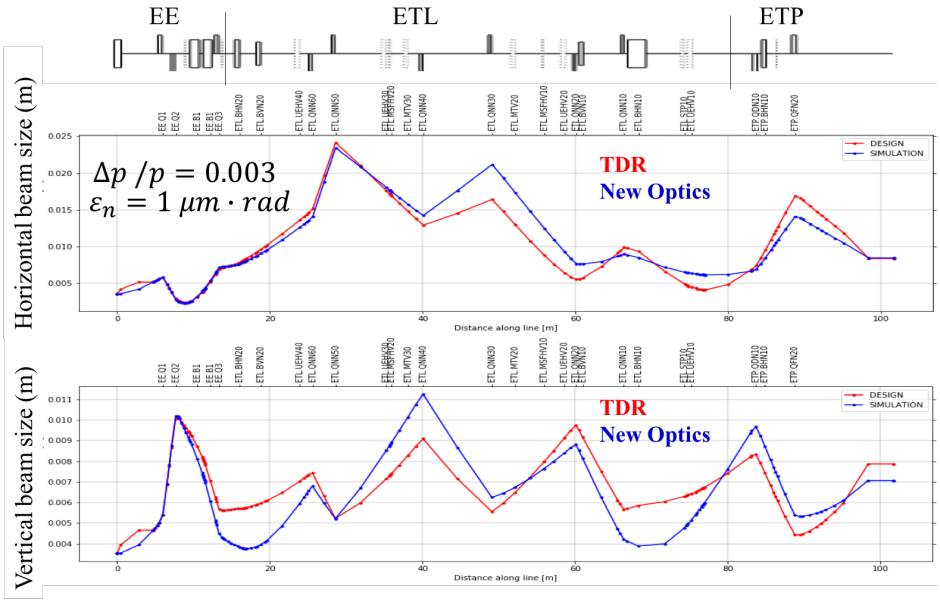

Figure 76: Horizontal and vertical beam sizes with the new optics and comparison with the design optics (TDR (5)).

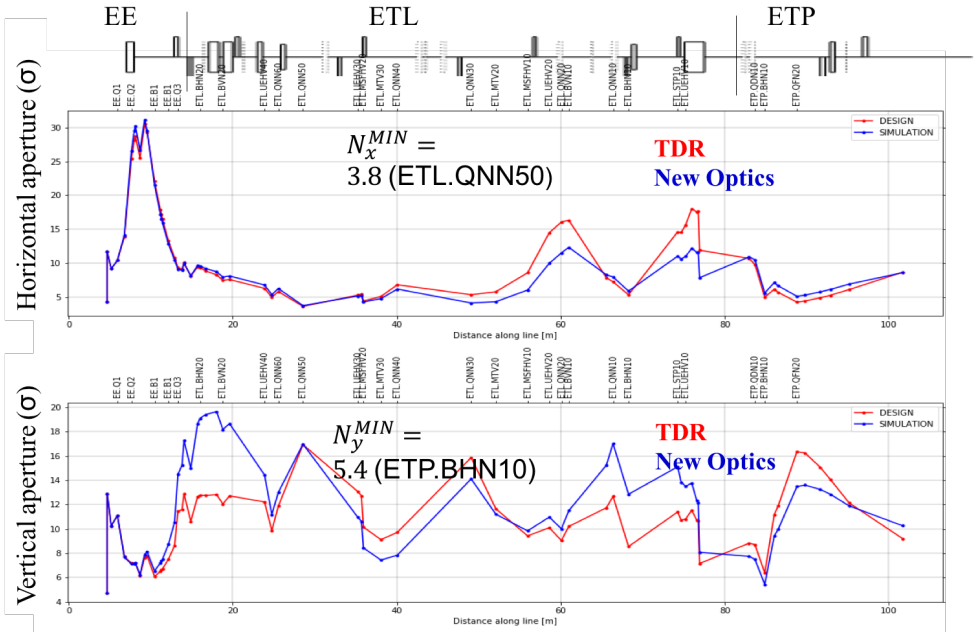

Figure 77: Horizontal and vertical aperture in beam sigmas with the new optics and comparison with the design optics (TDR (5)).

6 Beam performance reach and stability

6.1 NOMINAL beam (100 ns and 75 ns) along the injector chain

In this section the performance achieved during the 2018 LHC ion run is reviewed. The two NOMINAL beams, h = 2+4 (2 bunches extracted, also referred to as 100 ns in the PS) and h = 3+6 (3 bunches extracted, also referred to as 75 ns in the PS) are considered (33; 34; 35). After an initial overview of the performance across the ion injector complex up to the PS, a detailed discussion per machine is given.

Figure 78 shows the overall transmission efficiency from the ITH line to EI, from LEIR injection to extraction energy, from LEIR to the PS, and from PS injection to extraction energy. The performance for the h = 2+4 and h = 3+6 options are quite similar, with a transmission above 90%, excluding the LEIR capture losses of about 15% for the former and 20% for the latter.

Beam losses during the capture process limit the LEIR transmission efficiency, as can be seen in Fig. 79. The accumulated charges at flat bottom before capture (black points) and the extracted intensity (red points) are plotted as a function of the beam current measured for the first injected pulse. Above $9 \cdot 10^{10}$ charges there seems to be a saturation effect for which the gain in output intensity becomes very little in comparison to the increase of injected intensity. Nonetheless, a stable operation at the LIU target intensity could be achieved for a Linac 3 beam current of about 30 μA.

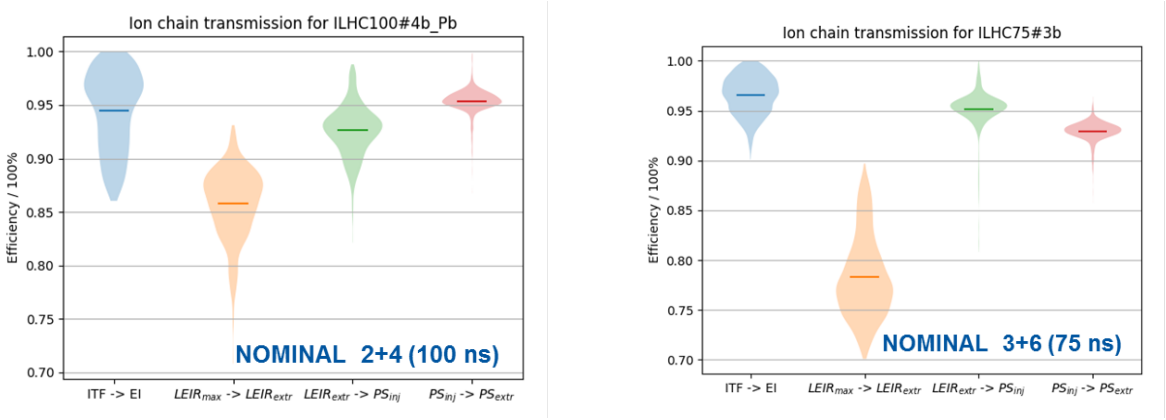

Figure 78: On the left, transmission efficiency along the ion injector complex up to the PS extraction for NOMINAL h = 2+4 (left) and h = 3+6 (right).

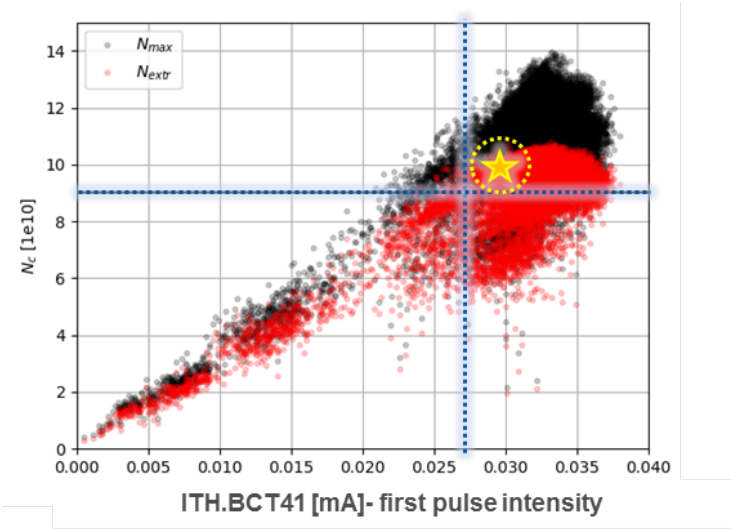

Figure 79: Transmission efficiency of NOMINAL h = 2+4 versus Linac 3 first injected pulse intensity. The black points represent the accumulated intensity at flat bottom before capture, the red points are the measured extracted intensity. Linac 3 pulse current $\geq$ 30μA allows to achieve the LIU target with sufficient operational margin.

6.1.1 LEIR

The performance of the NOMINAL h = 2+4 and h = 3+6 have been analysed considering the data accumulated during the LHC run, i.e. from 4/11/2018 to 3/12/2018. The analysis was done accounting for the Linac 3 performance following 2 criteria:

1. Average (7 injected pulses) current $\geq$ 30 μA.
2. Minimum pulse current $\geq$ 20 μA.

On top of this, the analysis was done accounting for the whole LHC run as well as only for the fills producing luminosity to the LHC experiments.

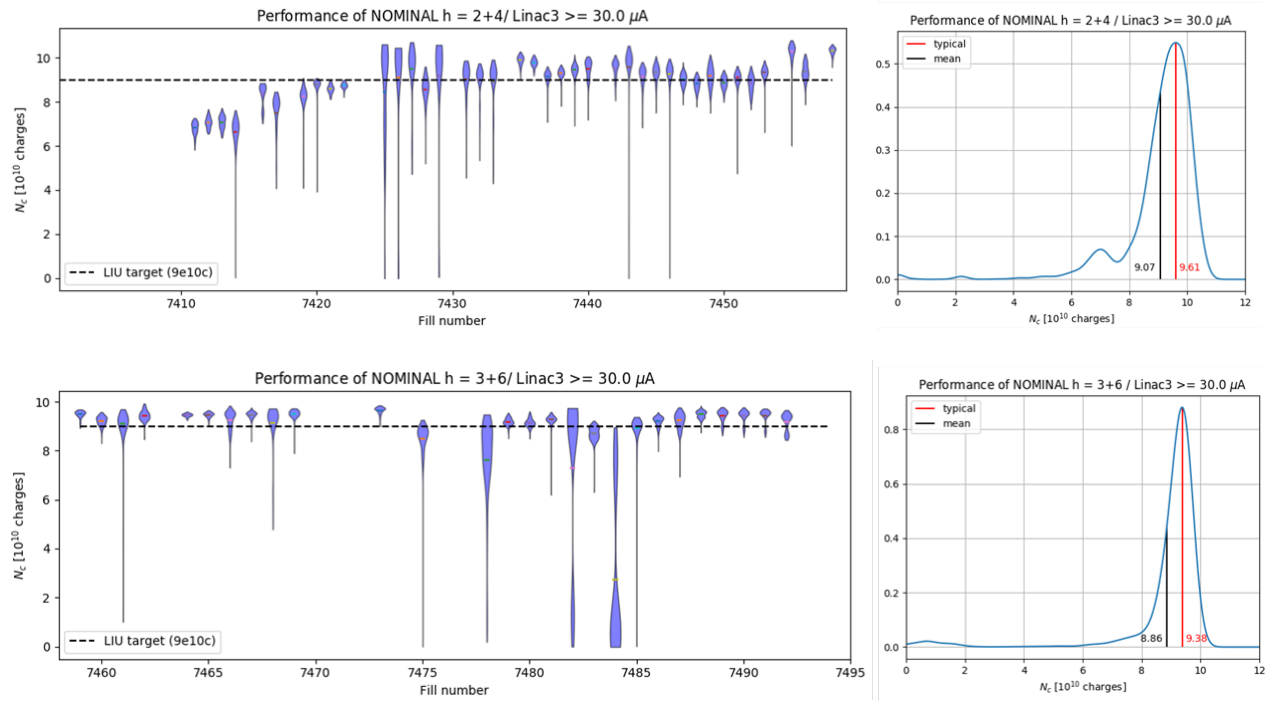

Figure 80: Left: statistics of extracted intensity versus fill number. Right: overall distribution. NOMINAL h = 2+4 is shown at the top, NOMINAL h = 3+6 at the bottom.

Figure 80 shows the extracted intensity statistics versus fill number, together with the overall distribution for the LHC run. The NOMINAL h = 2+4 case, required a first setup time to adapt LEIR operation to the improvements being done on the source setup. Accounting for the full LHC run, the extracted intensity was $9.1{\cdot}10^{10}$ charges on average, with a typical value of $9.4{\cdot}10^{10}$ charges. In the case of NOMINAL h = 3+6, whose operation followed the one of NOMINAL h = 2+4, the performance largely profited from the previous setup allowing for an extracted intensity of $8.9{\cdot}10^{10}$ charges on average, with a typical value of $9.4{\cdot}10^{10}$ charges. Filtering on the LHC fills that were effectively used for luminosity production, the NOMINAL h = 2+4 was extracting $9.4{\cdot}10^{10}$ charges on average, with a typical value of $9.7{\cdot}10^{10}$ charges, while the h = 3+6 was extracting $9.1{\cdot}10^{10}$ charges on average, with a typical value of $9.4{\cdot}10^{10}$ charges. These values have been summarised in Tab. 10.

NOMINAL	Fills	mean (10^{10})	typical (10^{10})	target LIU (10^{10})
2+4	all ion run	9.1	9.6	8.8
	luminosity production	9.4	9.7	
3+6	all ion run	8.9	9.4	
	luminosity production	9.1	9.4	

Table 10: Extracted intensities overview, in units of elementary charges, for NOMINAL h = 2+4 and h = 3+6. Average and typical values are compared to the LIU target (specified only for h = 2+4).

During the LHC run, LEIR operated with an average injection efficiency of $\simeq 50\%$ and

transmission efficiency (from injected pulse to the next pulse 200 ms later) of $\simeq$ 90%, as shown in Fig. 81.

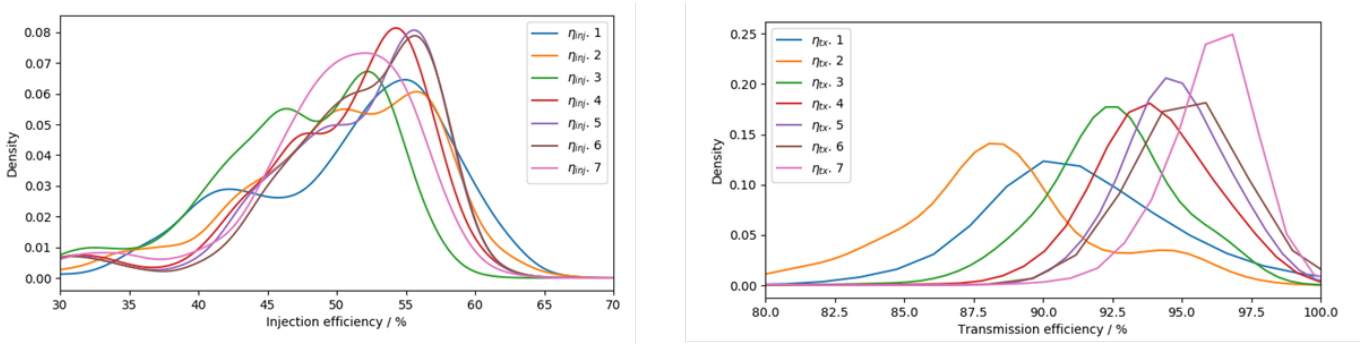

Figure 81: LEIR injection efficiency (left) and transmission efficiency (right) per injected pulse (statistic along the LHC run).

Concerning the capture losses, LEIR operated with an average efficiency between 80% and 95% depending on the total accumulated charge (Fig. 82). The loss mechanism, involving both space charge and IBS, seems to point to a maximum number of accumulated charges close to $11 \cdot 10^{10}$ above which no gain could be obtained by additional injected intensity.

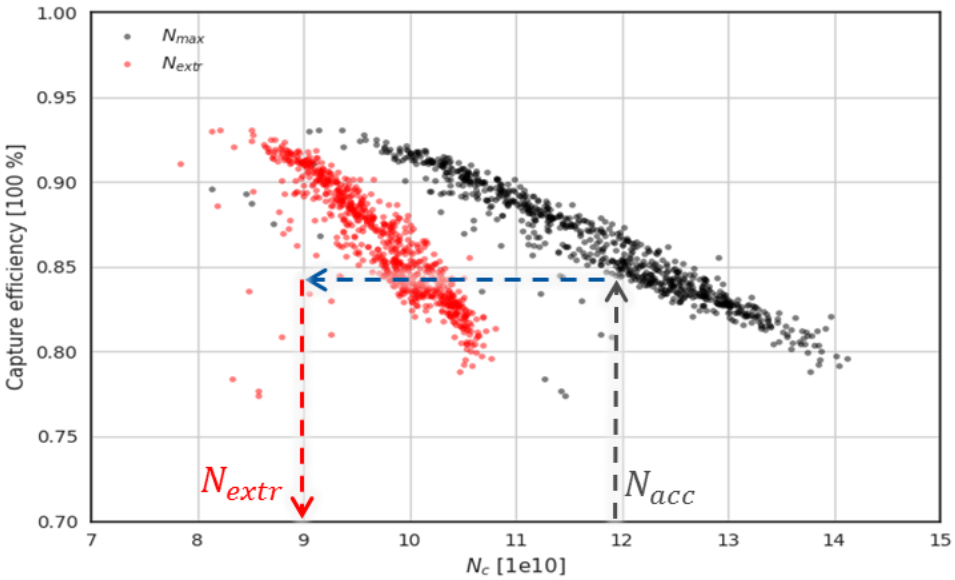

Figure 82: LEIR capture efficiency (statistic along the LHC run). The black points show the accumulated intensity before capture; the red points the extracted intensity towards PS.

6.1.2 PS

The lead ion beams do not suffer from strong intensity limitations in the PS. However, for high bunch intensities the beam becomes unstable just after transition crossing. The

instability is nevertheless suppressed by controlled longitudinal blow-up, with sufficient beam quality for injection into the SPS.

As with protons, the PS RF system offers the possibility of producing different bunch patterns for the LHC allowing the optimisation of the integrated luminosity along the years according to the development of new ideas for increasing the transmitted intensity. In 2015 the PS provided 2 bunches spaced by 100 ns per batch to the SPS, which is the same scheme as in Run 1. With the increased intensity available from LEIR in 2016, bunch splitting at flat top was introduced in the PS to provide 4 bunches spaced by 100 ns per batch to the SPS. This scheme was also used in the first half of the 2018 LHC run. In the second half, a new scheme with 3 bunches from LEIR was introduced with a batch compression at PS flat top, resulting in 3 bunches spaced by 75 ns per batch injected into the SPS. This gave the possibility to increase the number of bunches in LHC as a mitigation scenario in case the SPS slip stacking mechanism does not perform as expected. Figure 83 shows the three different beam production schemes during Run 2.

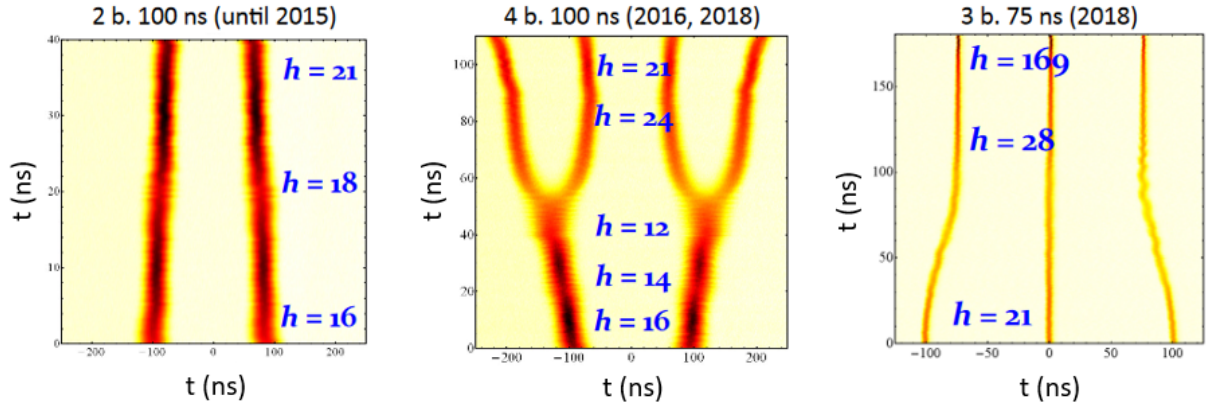

Figure 83: Overview of beam production schemes for lead ions in the PS used during Run 2: the waterfall plots of the wall current monitor are shown at an intermediate energy plateau for the 2 bunches spaced by 100 ns (left) and the 4 bunches spaced by 100 ns (center), while the 3 bunches spaced by 75 ns are obtained by batch-compression at flat-top (right).

The achieved versus target intensity in ions/bunch during 2018 is shown in Fig. 84 across the PS ion injector complex. Operation at 30 μA Linac 3 current per pulse allows the target intensity in LEIR to be exceeded by 10%. The achieved intensity in the PS is perfectly matched with the target one for the 100 ns beam, and exceeded by about 40% with the 75 ns beam, simply due to the missing additional splitting, which is used for the 100 ns beam in the PS.

6.1.3 SPS

The SPS cycles are characterised by a long injection plateau and many PS batch injections due to the rise time of the SPS and LHC injection kickers. Beam degradation along the long SPS flat bottom (tens of seconds) results in a large spread of bunch parameters in terms of intensity, bunch length and transverse emittances. The beam degradation mainly arises from transverse space charge and IBS, and it strongly depends on the intensity per

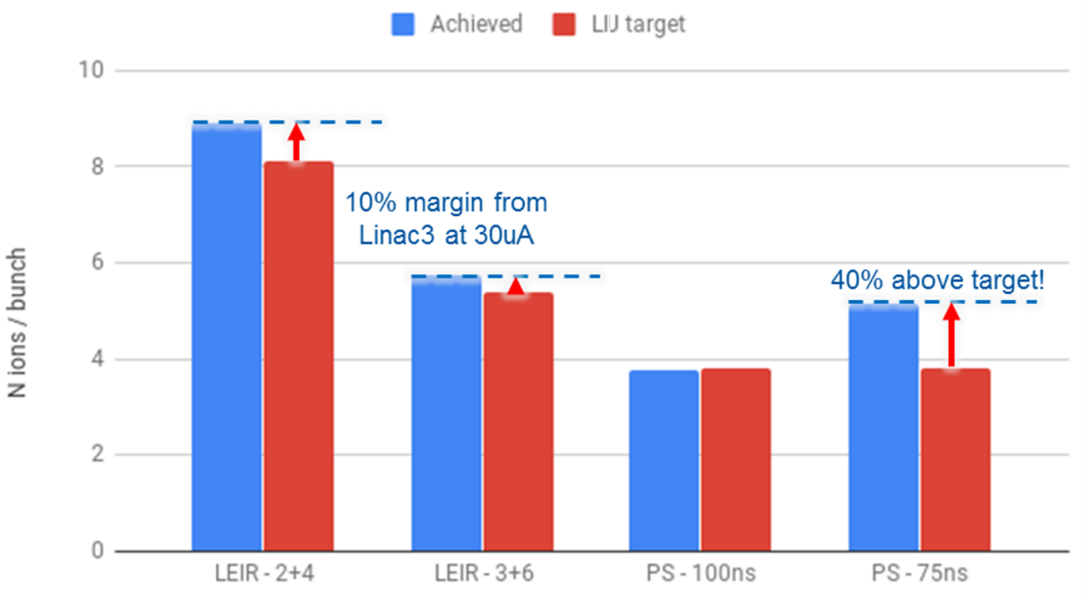

Figure 84: Target and achieved intensities in 2018 up to PS.

bunch. In addition, RF noise is suspected to contribute to losses out of the RF buckets. The number of injections into the SPS is optimised to achieve the best compromise between beam degradation on the SPS flat bottom and luminosity in the LHC. In 2015, 12 batches (with two bunches separated 100 ns each) from the PS were injected into the SPS before transfer to the LHC. In 2016, with four bunches per PS batch, a total of 7 injections from the PS were accommodated in the ion cycle (due to the LHC injection kicker limitations) before transfer to the LHC. Although the number of injections in 2016 was almost half as many as in 2015, the bunch intensity was half too, because of the PS double splitting. Since, in addition, the 2016 cycle length was, correspondingly, almost halved, space charge and IBS destructive effects were considerably reduced allowing more intensity to be extracted than in 2015.

In 2018 two different SPS cycles were created, one for the 4-bunch with 100 ns spacing, and another one for the 3-bunch with 75 ns spacing. The first one accommodated the injection of nine PS batches. Although the cycle was prepared for 12 injections, the LHC abort gap had been already setup for the 3-bunch 75 ns scheme, which limited the number of injections to nine. Despite the restrictions, the 4-bunch 100 ns spacing schema allowed the extraction of around 8% more total intensity than in 2016. The second one, 3-bunch with 75 ns spacing, with a longer flat bottom, could fit the injection of 14 batches and an increase of the extracted intensity of around 40% compared to 2016 was remarkably achieved.

Figure 85 shows, on the left, the two ions cycles implemented for the 100 ns and 75 ns beams delivered by the PS where the improvements brought by the later scheme are already visible. On the right, the corresponding LHC achieved intensity per bunch and total intensity. With 75 ns, $\sim$ 67% of SPS LIU target on total intensity in LHC have been achieved compared to $\sim$58% for the 100 ns case. As visible from the left plot, the transmission lifetime remains the main bottleneck to further increase the intensity.

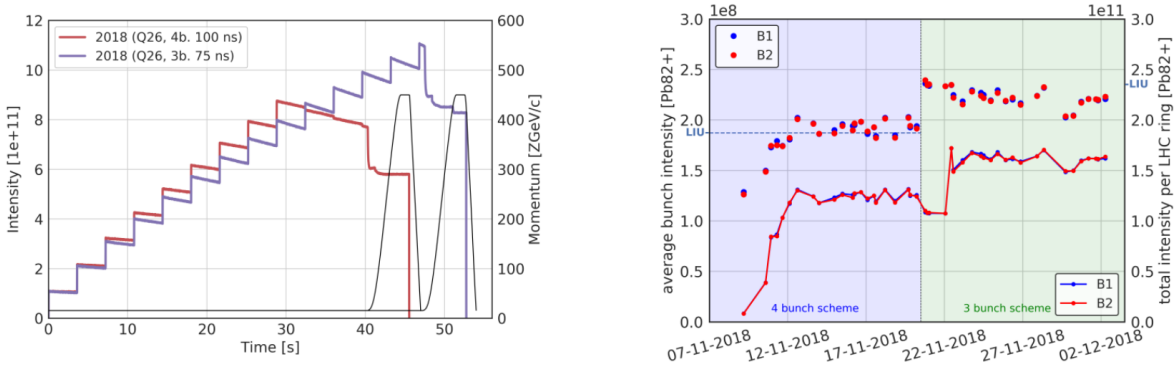

Figure 85: On the left, the two ions cycles implemented for the 100 ns and 75 ns beams delivered by the PS, on the right, the corresponding achieved intensity per bunch (dots) and total (full line) in the LHC compared to the LIU target.

6.2 LEIR injection efficiency sensitivity to Linac 3 settings

LEIR injection efficiency sensitivity (and therefore extracted intensity) to Linac 3 parameters has been subject of extensive studies throughout 2018. As an example, Fig. 86 shows the dependency of injected intensity in LEIR on Tank 1 phase. These parameters, together with Tank 3 and the ramping and debunching cavities settings, were found to be very effective for performance recovery after energy drifts due to, for example, stripper foils performance degradation. At the same time, the constant monitoring of these parameters allowed a deeper understanding of the LEIR injection process. The scans of all the RF parameters are given in (36).

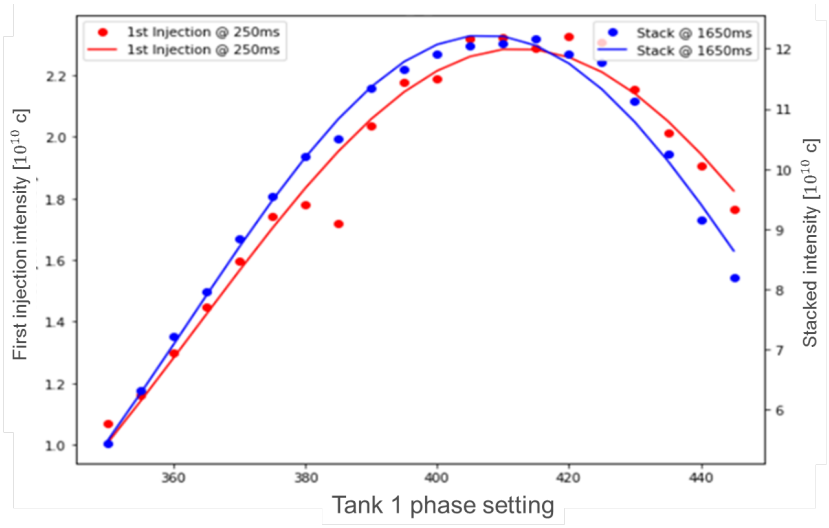

Figure 86: LEIR dependence on Linac 3 settings: first injection intensity and maximum stacked intensity versus Tank 1 phase.

6.3 Temperature drifts

LEIR injection reproducibility was found to be highly affected by temperature variations. Figure 87 shows the effect of temperature (left) on the distortion of the injection trajectory into LEIR as measured from the injection line BPMs and the equivalent distortion made by a programmed kick on ETL.BHN10 (right): given the similarity of the shape and the occurrence mainly in the horizontal plane, the magnet was identified as the main source of the trajectory distortion.

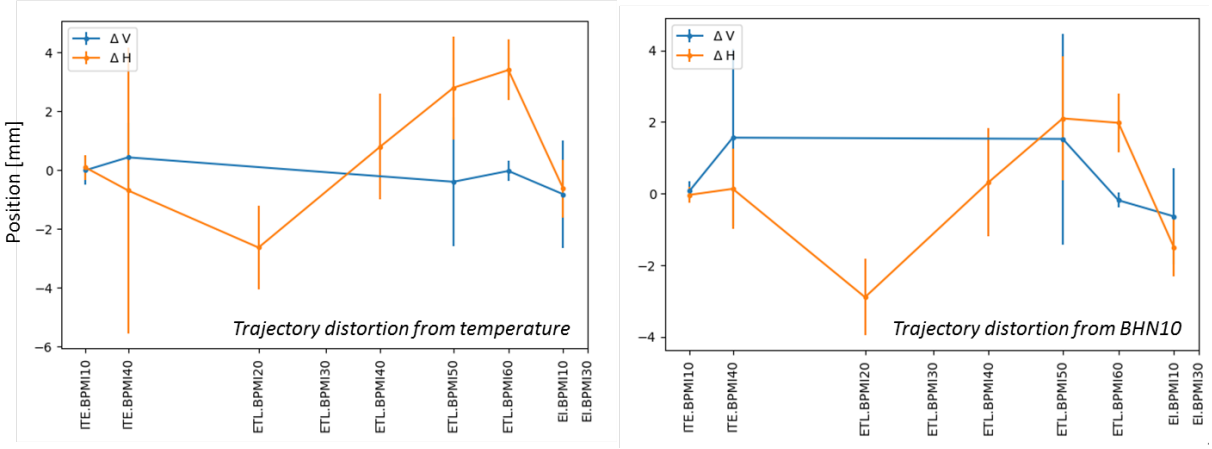

Figure 87: Distortion of the injection line trajectory due to temperature variation (left) and ETL.BHN10 kick (right).

First tests were done changing the reference current card of the magnet, which was suspected to be sensitive to temperature, but were not found to be effective against the temperature variation. Subsequently, the current function of the magnet was changed to mitigate the excursion from 0 A to 70 A. Setting the start current to 65 A (see also Sec. 2.5.2) reduced the current variation to only 5 A as well as the overshoot, mitigating in turn the temperature dependence. Figure 88 shows on the left the temperature dependence of the first injection of an EARLY type beam versus temperature (-10%/°C), and on the right the positive effect of the reduced current excursion.

6.4 Stripper foils

The stripper foils performance was carefully monitored by both Linac 3 and LEIR operation teams. During 2018, different means were put in place in order to be able to monitor the main observables that could be correlated with a mis-functioning of the stripper foil. Figure 89 shows, on the top, the mean and standard deviations evolution over ten days of the injected momentum spread measured on a cycle constantly played in the LEIR supercycle (typically called MDEARLY). In the middle, the ramping rate measured on the ETL.BPMI60: this is the first order fit in mm/100 ms (i.e. the energy ramping rate along the Linac 3 pulse) of the horizontal beam position as a function of the pulse in the ETL.BPMI60 as shown in Fig. 47 for the EI.BPMI30. On the bottom, the pulse current measured by the transformer ITH.BCT41. As can be seen, a significant drift is recorded by all the observables, which

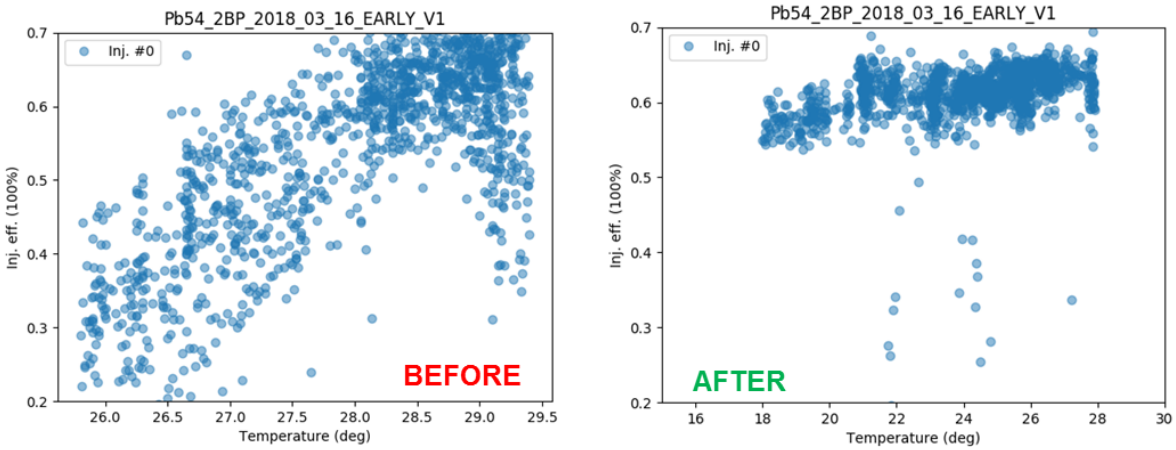

Figure 88: Correlation between the injection efficiency of the first pulse and temperature before (left) and after (right) the correction of the ETL.BHN10 programmed function.

was correlated to a decrease in stripping performance. For example, an increase of current measured by ITH.BCT41 implies higher charge states different from $^{208}Pb^{29+}$ are transmitted in the injection line. Similar measurements were done as well from weekly measurements in Linac 3 ITFS spectroline (dedicated and destructive). The observation triggered the replacement of the stripper foil which ensured better operation afterwards, as indicated in the plot. We let the reader notice that both ITH.BCT41 and the ramping rate embed information of additional charge states propagation, while the mean momentum deviation refers to $^{208}Pb^{54+}$circulating in LEIR.

Based on 2018 observations, the stripper foils will be changed every 2 weeks (interleaved with source refills) to ensure good performance operation (37).

6.5 PS stray fields

Since 2016 operation, the effect of the PS magnetic cycle on the LEIR injection efficiency is known to be important, in particular concerning the PS cycles reaching more than 24 GeV/c (38). A custom Software Interlock System (SIS) algorithm was put in place to correct the beam trajectory of the LEIR cycles during which the PS magnetic field was increased beyond 24 GeV/c. The trajectory was corrected by a fixed amount hard coded in the algorithm by changing the deflection angle provided by the ETL.BHN10 magnet. The correction was proven to be effective during a dedicated test, but the extension to different supercycle compositions was only planned.

In 2018, two new algorithms, the equalizer and the autopilot, were developed to compensate for the stray field effects. Both algorithms work in a similar way. By looking at the injection efficiency of each of the 7 injections during a cycle, the algorithm determines which injection has the highest efficiency. The corresponding beam position at the ETL.BPMI60 for each of the injections is measured. The beam position of the highest efficiency injection is used to derive the required correction to the deflection angle for each of the 6 remaining injections, to bring each one to the same level.

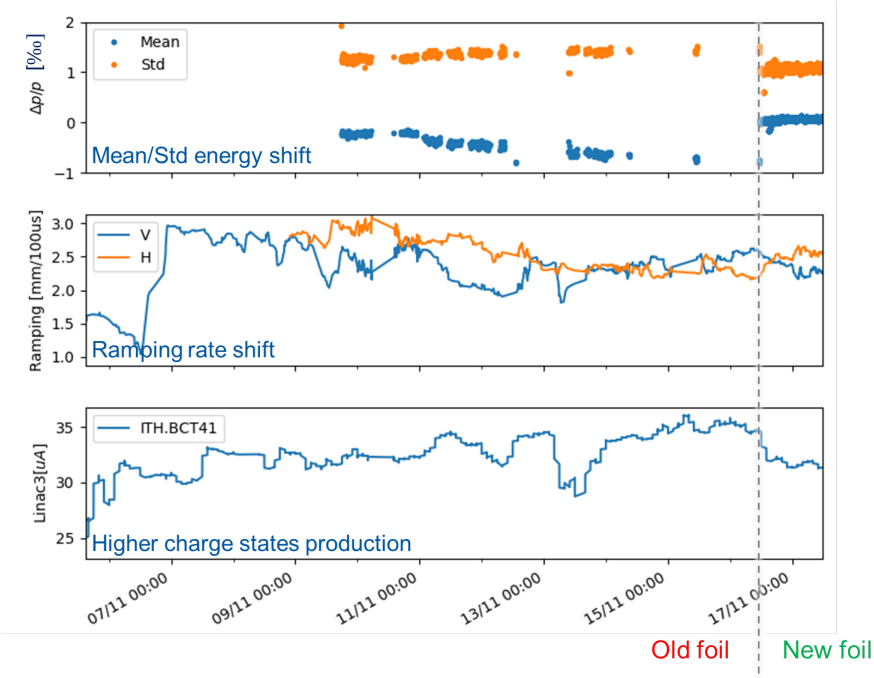

Figure 89: Observables constantly monitored over time to detect sources of performance degradation. Top: mean and standard deviations evolution of the injected momentum spread using the MDEARLY cycle (in unit of ‰). Middle: the energy ramping rate of the 200 μs Linac 3 pulse measured with the ETL.BPMI60. Bottom: pulse current measured by the transformer ITH.BCT41.

The difference between the algorithms is that the equalizer acts on demand, monitors a few super-cycles, performs the calculation and applies the correction once to the desired user, therefore, all the cycles of that user get the same correction. The autopilot, on the contrary, is an online tool working on a cycle-by-cycle basis and in a continuous way, provided the application is up and running, because it is not running in a server.

The equalizer algorithm is executed by running a Python script and the result is illustrated in Fig. 90. The top left plot shows evolution of the beam position at ETL.BPMI60 for each of the seven injections. The bottom left plot shows the injection efficiency of each of the seven pulses for each of the positions above. When the algorithm applies the appropriate correction to the beam position using the ETL.BHN10 function, the right plot shows, for one of the cycles, that the injection efficiencies of each of the seven injections (magenta bars) are pretty much uniform.

The GUI of the autopilot is shown in Fig. 91. The top left plot shows the ETL.BHN10 deflection angle function in radians. The right vertical axis shows the values of the angle for each of the seven injections (as can be seen from the plot, each injection has a different angle); the left vertical axis shows the corresponding measured beam position by ETL.BPMI60 in mm. The right plot shows the evolution of the injected intensity (black dots) over time. As can be seen, one of the cycles in the super-cycle has less injection efficiency than the others, likely suffering from the presence of the PS stray fields. The algorithm, after some iterations, is able to equalize, not only the injection efficiency of each of the injections, but also of all

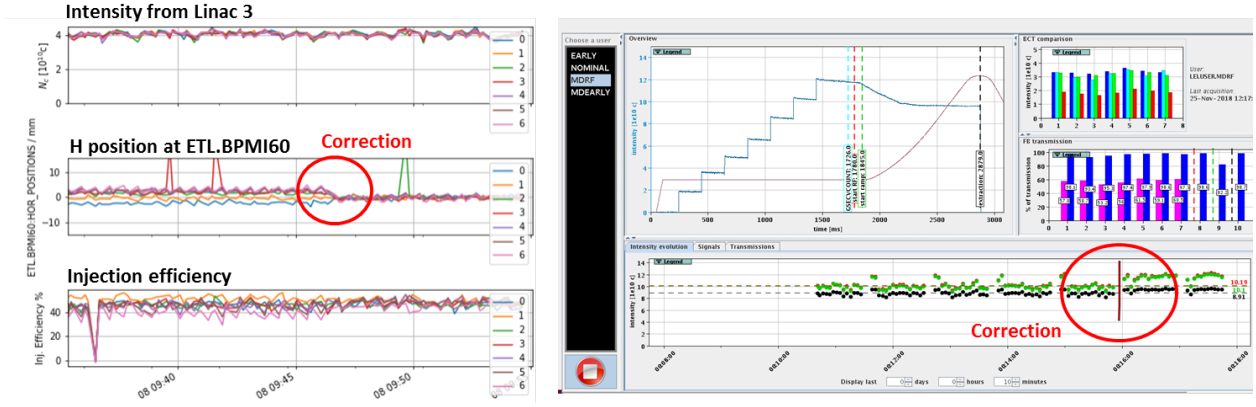

Figure 90: PS stray field correction using the injection equalizer. Left plot, intensity, horizontal position at the ETL.BPMI60 and injection efficiency for the 7 pulses sent from Linac 3; right plot, the "equalized" injection efficiency after the trajectory correction from the LEIR monitor application (see Fig. 3 for details on the LEIR monitor).

the cycles, which might need different corrections depending on the influence of the stray fields.

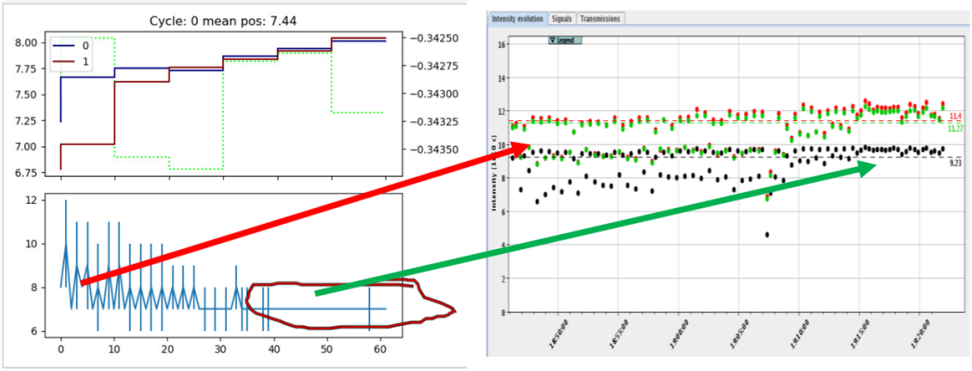

Figure 91: Stray field correction from the PS using the autopilot. At the the top left plot the two last ETL.BHN10 settings for the 7 injections are shown (blue and red curves) together with the last horizontal positions for the 7 injections measured at the ETL.BPMI60 (in green). At the bottom left the monitored mean and standard deviation of the horizontal positions is shown as a function of the algorithm iterations. On the right the extracted intensity has progressively improved (see Fig. 3 for details on the LEIR monitor).

Both tools were proven to be effective in the 2018 LHC run and can, in principle, also act on effects not related to stray fields, like slow temperature drifts. Since the SIS based method did not seem flexible enough (e.g. it is difficult to include the available information of the injection line BPMs) these tools will be maintained and made available for post-LS2 operation. As a significant spread in vertical trajectory has been observed as well, the possibility of introducing a vertical function-based corrector is being investigated (39).

6.6 Beam instabilities

During the 2018 LHC ion run, few occasional instabilities were detected which affected the LEIR beam production during the preparation phase before LHC filling. Figure 92 shows an example of the effect of such an instability, as seen from the LEIR OP-VISTAR monitor during operation on the 9/11/2018: apparently random NOMINAL cycles exhibited large losses at the last accumulation step, first and third cycles in the picture.

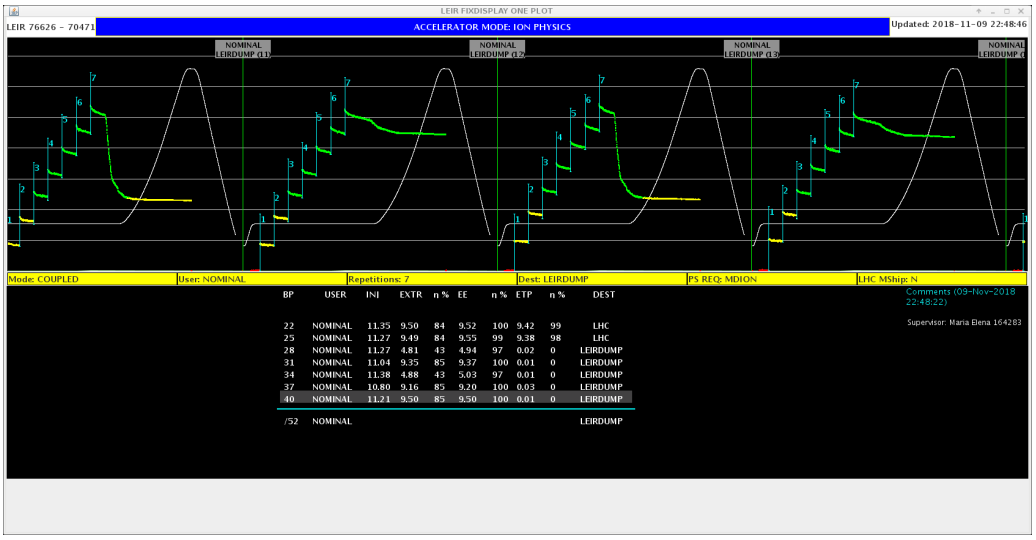

Figure 92: Unstable NOMINAL cycles (first and third from the left) before capture as seen during the LHC run on 9 November 2018.

The observation of the transverse motion at the damper pickups and the voltage sent from the damper kicker can give valuable information on the activity present on the beam. In correspondence with the cycles exhibiting large losses, the traces in Fig. 93 show the vertical (green) and horizontal (yellow) coherent activity together with the damper kicker voltages on the inside (orange) and outside (orange) horizontal plates, and on the bottom (red) and vertical (light blue) vertical plates. One can observe the presence of an instability in the horizontal plane after the 7^{th} injection. Also, while the coherent activity following each of the 7 injections is quickly damped in the vertical plane, this does not seem to be the case in the horizontal plane (e.g. after the second injection) and will be the subject of future investigations at the restart.

The details on the coherent motion are visible in Figs. 94 and 95: on the first, coherent spectral lines are detected between 10 MHz to 25 MHz, on the second, we see how the modulation affects the coasting beam.

A second confirmation can be obtained from the longitudinal Schottky spectrum of Fig. 96 where a side band close to the revolution frequency is visible (white vertical marking lines) and corresponding to an horizontal tune shift of ~ 0.33. This is larger than the expected horizontal tune shift of 0.19 and can be explained by the additional space charge tune shift detected on the Schottky spectrum. For a coasting beam of $9 \cdot 10^{10}$ charges within a normalised emittance of 0.2 μm, the maximum space charge tune shift can be as large as ~ 0.13 (40), filling the remaining shift observed.

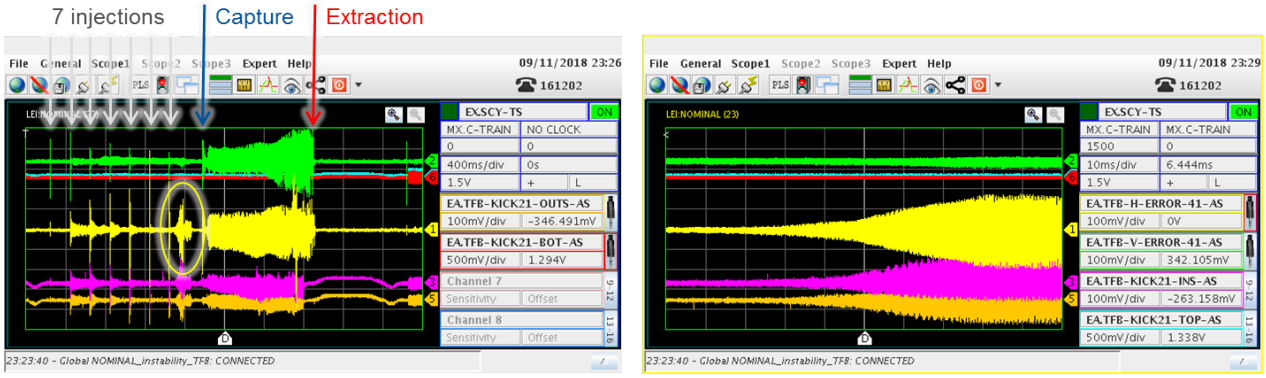

Figure 93: Corresponding coherent activity as seen from the damper pickup and kicker plates voltage: traces correspond to the vertical (green) and horizontal (yellow) coherent activity together with the damper kicker voltages on the inside (orange) and outside (dark yellow) horizontal plates, and on the bottom (red) and vertical (light blue) vertical plates. On the left, activity along the cycle, from injection to extraction, showing the instability highlighted in yellow. On the right, zoom of the horizontal instability.

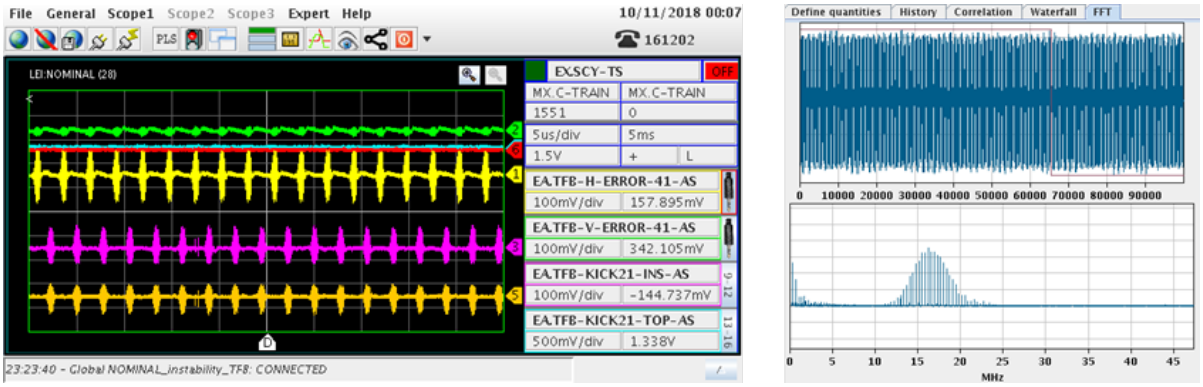

Figure 94: OASIS traces of the unstable NOMINAL cycles at 1551 s. Yellow and green traces refer respectively to the horizontal and vertical signals at the damper pickups. Pink and orange ones refer to the kick applied by the feedback kicker respectively on horizontal and vertical planes. On the right, the FFT of the coherent signal in the horizontal plane: the frequency content is between 15 and 25 MHz.

Similar occurrences were seen also during dedicated MDs along the year (see for examples e-logbook entries on 7/08/2018, 13/11/2018 and 15/11/2018).

The instability mechanism is currently being analysed in detail (41). From an operational point of view, the instability is strongly related to the cooler settings applied during the coasting beam accumulation phase. As described in Sec. 5.10, the final emittance and momentum spread depend strongly on the cooler angle and position. In particular, a change of few tenths of a mrad at the cooler bump can significantly impact the stability margins. Figure 97 shows the cooler bump alongside the signals observed at the damper pickups: a tiny correction of -0.5 mrad of the cooler angle can stabilise the beam without significantly impacting the accumulation process.

This behaviour is compatible with a loss of Landau damping due to the smaller final

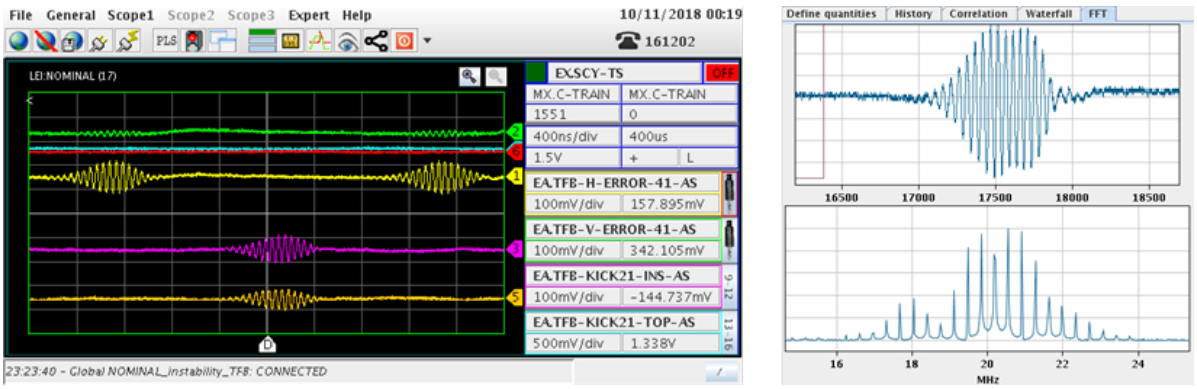

Figure 95: Zoomed view of the instability showing a similar resonant pattern.

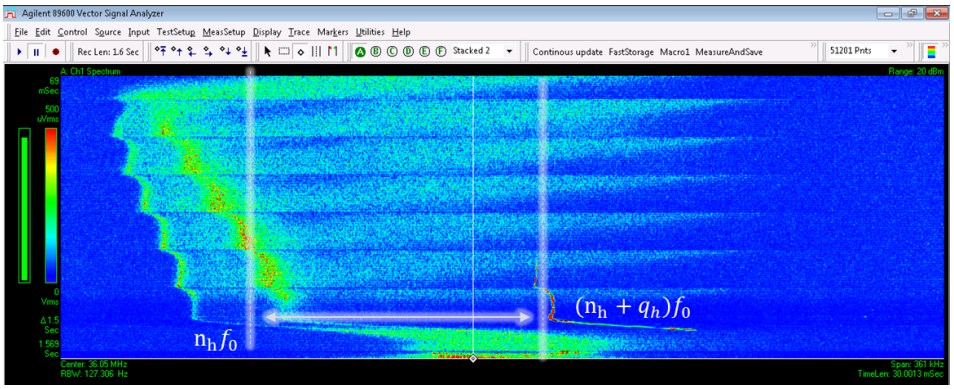

Figure 96: Longitudinal Schottky spectrum around the 100^{th} harmonic of the beam: a side band is arising after the last injection correspondent to the instability observed on the damper pickups.

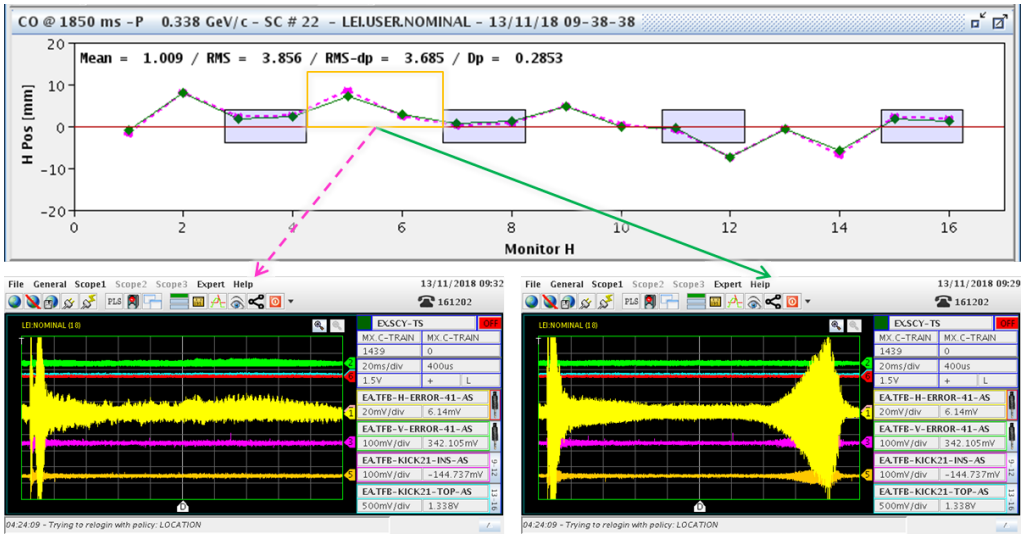

Figure 97: The effect of the horizontal angle on the instability: slightly correcting by -0.5 mrad the cooler angle (highlighted orbit trace) the beam can be made stable.

emittance when the angle of the cooler bump is too flat. Comparing to Fig. 66, the point B (x =10 mm, x' =-1 mrad) increases the final horizontal emittance and relaxes the stability margins, while point A (x =10 mm, x' =0 mrad) allows the maximum cooling rate and smallest final emittance, but limits the stability margins.

When the momentum spread is too small, as in point A, longitudinal instabilities can be observed as well in the typical form of self-bunching (42) as visible in Fig. 98.

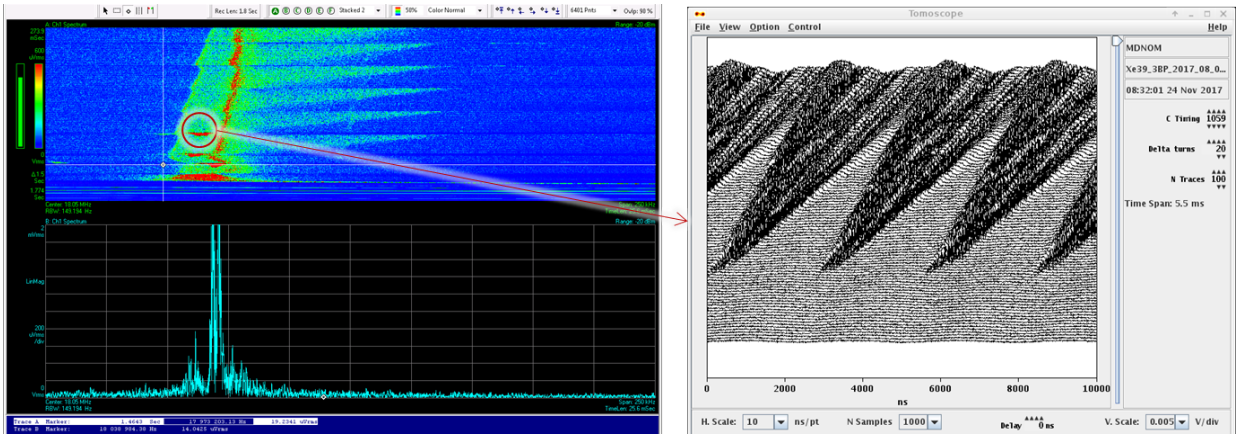

Figure 98: Effect of point A on longitudinal beam stability: on the left, Schottky spectrum showing 3 occurrences of a longitudinal instability, on the right, self bunching observed at the tomoscope during the first instability.

While the cooler horizontal angle is an effective knob to stabilise the beam, it also confirms that stability margins need to be assessed and other parameters (like damper gain and chromaticity) are being studied in simulations during LS2 (e.g. with the recently developed branch of PyHEADTAIL for coasting beam (25)).

6.7 Performance monitoring

In 2018, a performance monitoring website (https://info-leir.web.cern.ch/info-leir/main.htm) was put in place in order to quickly monitor the machine performance reach and stability. Parameters like beam intensity along the injection line, beam position at the available injection line BPMs, mean and standard deviations of the Linac 3 incoming pulse energy distribution, injection and capture efficiency, accumulated and extracted intensities, were monitored and tracked versus time. Starting from this experience, and in the frame of a global effort for all CERN accelerators, a similar tool will be put in place at the restart after LS2 (43).

6.8 Vacuum pressure

A performance degradation was identified on 9 August 2018 in correlation with the local vacuum pressure increase in straight section 4 of the machine as shown in Fig. 100, leading to up to 10% beam loss if above 10^{-9} mbar. The losses could be mitigated applying an horizontal orbit bump in that sector. This issue is still under investigation and has been observed and cured in past operational years using the same strategy.

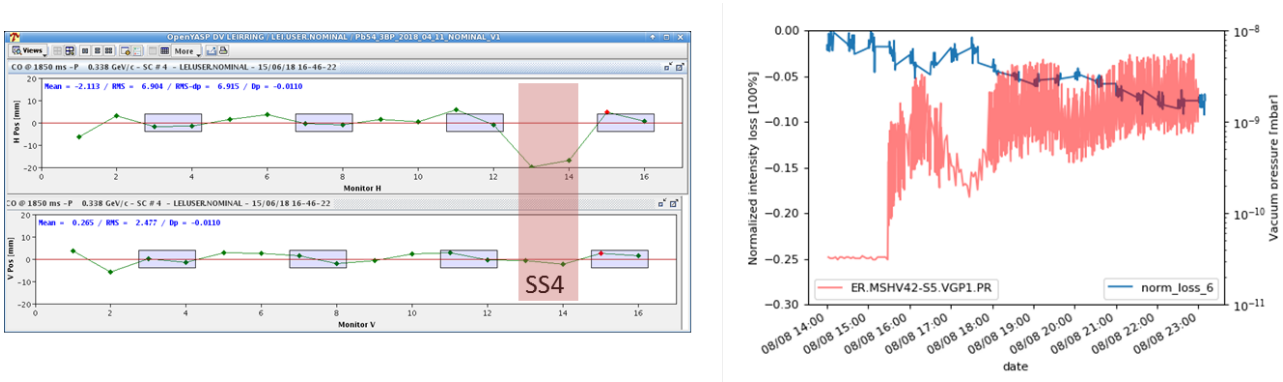

Figure 99: On the left, YASP orbit with highlighted horizontal orbit bump in straight section 4. On the right the effect of the pressure rise (red trace) on beam loss (blue trace).

While the implementation of the bump was known to prevent the pressure rise since 2016 and it is systematically applied to all the cycles played in the LEIR supercycle, it is interesting to notice that only a specific MD cycle accidentally did not implement it, causing a slow pressure increase when it was played. Figure 100 shows the vacuum pressure reading versus time before (red background) and after (green background) the orbit correction implementation in the MD cycle: the correlated pressure spikes disappear allowing a continuous pressure decay.

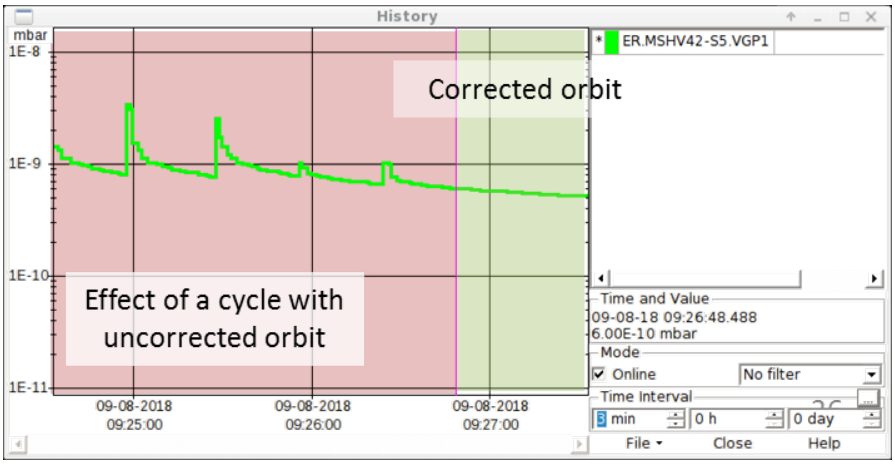

Figure 100: Vacuum pressure reading from the vacuum port MSHV42 before (red background) and after (green background) the orbit correction implementation in the MD cycle to which the pressure spikes were correlated.

7 Machine studies

7.1 Space charge and IBS studies

The equilibrium emittance of the LEIR beam results from the interplay of electron cooling and heating processes like IBS and space charge. Before acceleration, when the electron cooler is switched off and the coasting beam is captured into bunches by means of the RF cavities, a fraction of the beam is lost. This fraction is larger the higher the intensity of accumulated beam. To understand the driving mechanism of the losses, detailed studies of the interplay of space charge forces and excited betatron resonances have been performed for different machine working points. The emittance growth and subsequent losses were simulated with the code *PyORBIT* (44), using a space charge solver based on an adaptive frozen potential. A qualitative agreement with the measurements was found, as reported in (45; 46). Some excited resonances in the tune diagram were identified as a source of losses. However, the results of space charge simulations could not account for all the emittance growth and beam loss observed in the measurements. During 2018, a series of analytical and experimental studies were performed to understand the impact of IBS on the emittance growth.

The results of a static tune scan are shown in Fig. 101. A single pulse is injected from Linac 3 at $t = 245$ ms and the large initial emittances are cooled to their equilibrium values. At $t = 526$ ms the cooler is switched off and the emittances start to grow due to IBS and space charge. At $t = 580$ ms the beam is captured in bunches. As the beam is compressed longitudinally it is more affected by collective effects and the transverse emittance growth is enhanced. The growth depends on the vertical tune and large values are found above the vertical resonance at Q_y=2.66 and above Q_y=2.59, where the normal third order coupling resonance $Q_x + 2Q_y$ crosses the nominal horizontal tune Q_x=1.82.

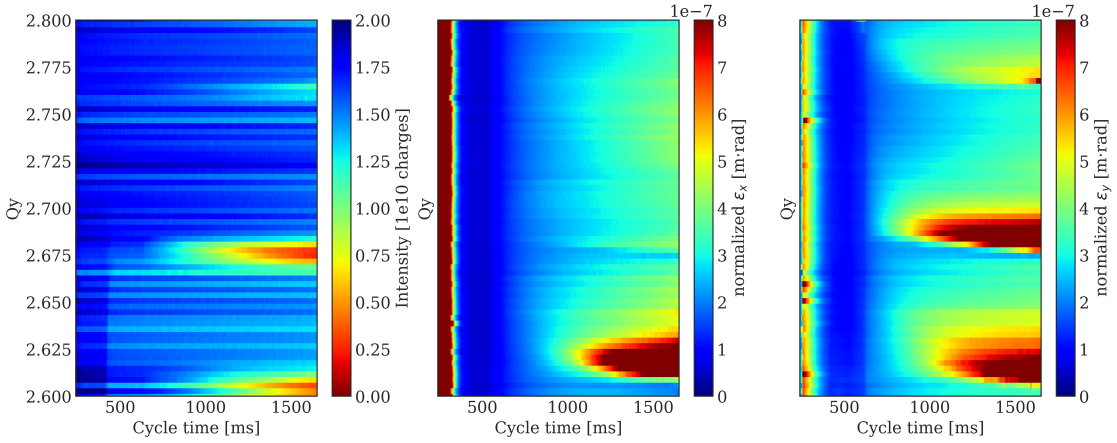

Figure 101: Evolution of the intensity and transverse emittances at the injection field for different vertical tunes with RF capture at 580 ms.

The aperture model of LEIR was carefully updated in 2018 including the bending magnets of the arcs (47). Losses are predicted for geometrical emittances above 26 mm·mrad (horizontal) and 6 mm·mrad (vertical), which correspond to normalized emittances of 2.46 mm·mrad

(horizontal) and 0.57 mm·mrad (vertical) at injection energy. Thus, the losses observed in Fig. 101 (left) are associated to the vertical emittance growth beyond the physical aperture for vertical tunes in the vicinity of the above mentioned resonances, as shown in Fig. 101 (right).

Next, we studied the nature of these resonances to understand if they are driven by space charge or by lattice components (e.g. by sextupoles, fringe fields, etc). The third-order non-systematic coupling resonance $Q_x + 2Q_y = 7$ was excited by sextupolar errors in the lattice and its compensation by means of two normal sextupoles was achieved and reported in (46). The resonance at Q_y=2.66 could be a third-order skew systematic resonance ($3Q_y$=8) excited by skew sextupole components in the lattice. We tried to compensate it with the use of a pair of skew sextupoles with appropriate phase advance. An extended range was used as compared to the study reported in (46), in which only partial compensation had been achieved. We optimized the strength of the sextupoles by performing a dynamic tune scan, i.e. maximizing the transmission while crossing the excited resonance. Almost perfect compensation was achieved, as shown in Fig. 102 (left).

A projection of the above tune scan at a cycle time of $t = 1000$ ms is shown in Fig. 102 (right) for two cases, with no compensation of the resonance at $Q_y = 2.66$ (top), and compensating it with the use of skew sextupoles with optimized strength (bottom). In the latter case, the intensity and the emittance are almost constant along the vertical tune scan, illustrating the compensation of the resonance and furthermore pointing towards IBS as possible source of the growth as discussed below.

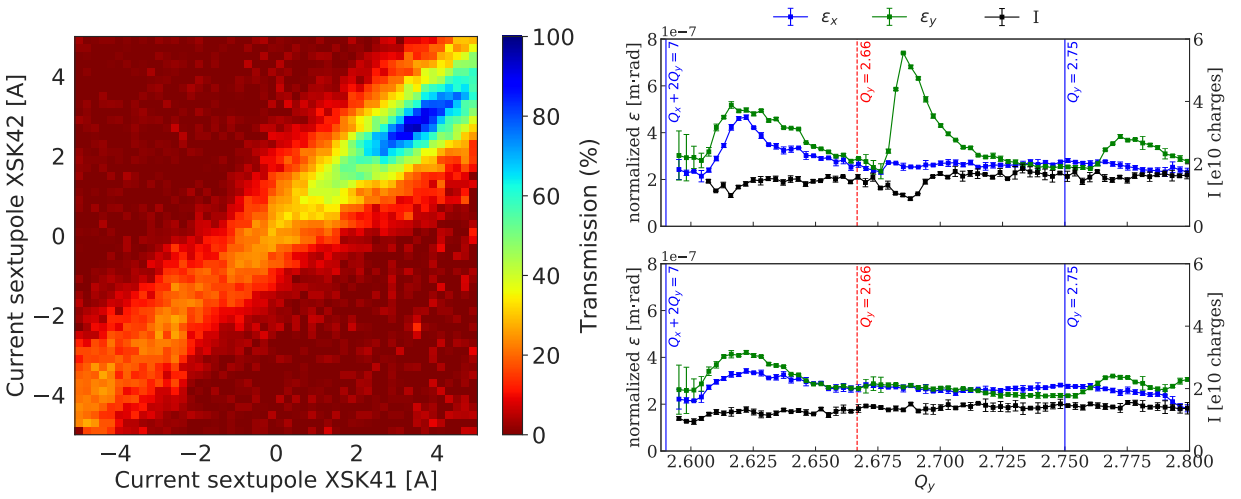

Figure 102: Left: beam transmission while crossing the resonance at Q_y=2.66 as a function of the currents in the sextupoles. Right: measured emittances and intensity as a function of the vertical tune at t=1000 ms for the standard machine settings (top), and after compensating the excitation of the skew resonance $Q_y = 2.66$ by means of a pair of skew sextupoles (bottom).

We performed a comparison of the measured emittance growth with the predicted growth from the analytical IBS calculations using the IBS module included in the MAD-X code (48). A systematic benchmark of different codes and a detailed discussion on the results of the analytical calculations can be found in (49). Figure 103 shows the measured and calculated

emittances for a coasting beam with high intensity and for a bunched beam with low intensity, for the nominal tunes (Q_x=1.82, Q_y=2.72).

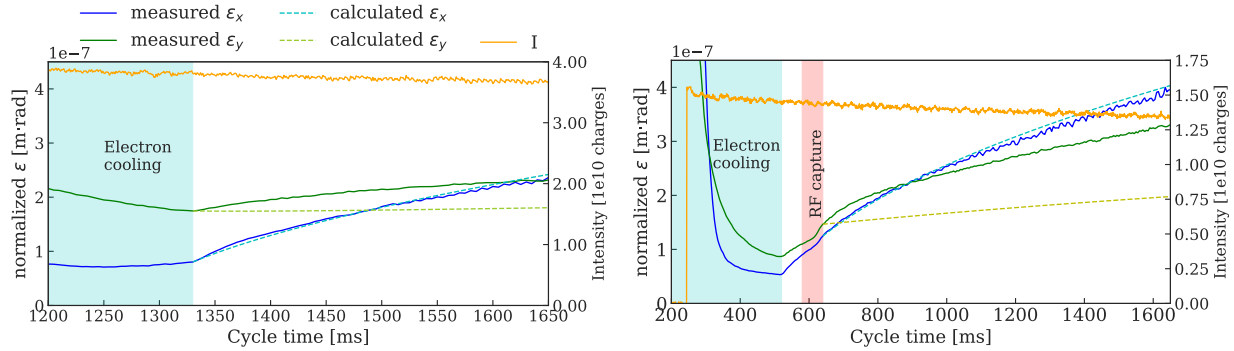

Figure 103: Comparison of the measured emittance blow-up with the calculated emittance blow-up caused by IBS for a coasting beam with high intensity (left) and for a bunched beam with low intensity (right).

A good agreement between the measurements and the IBS calculations, with differences <2.5%, was found for the horizontal emittance growth in both coasting and bunched beam cases. Instead, in the vertical plane, the calculations reproduced only a small fraction of the measured emittance growth, i.e. 3% (calculations) growth compared to the 33% (measurements) for the coasting beam case, and 34% (calculations) compared to 123% (measurements) for the bunched beam case. Investigations about possible sources for the missing vertical blow-up are ongoing. Among them are vertical dispersion and transverse coupling, which are present in the machine (a vertical dispersion of 0.1 m and a coupling coefficient of 0.01 have been measured) but are not included in the lattice model used for the calculations. However, the more likely source of the discrepancy is an instrumental effect of the Ionization Profile Monitor used to measure the beam size caused by the space charge of the circulating beam affecting the trajectories of the ionised residual gas molecules used to measure the profile (50).

7.2 Electron cooling studies

Following the recent development of an electron cooling simulation tool as part of RF-Track (51), a number of dedicated studies were performed to characterize the cooling force and benchmark the new code. Additional electron cooling studies were performed to try to overcome the intensity limitations of LEIR, and to indirectly measure the electron beam parameters and create maps to prepare beams with given characteristics (52).

7.2.1 Cooling force characterization

The longitudinal cooling force between the ions and the electrons was measured directly, and benchmarked with simulations. First the ion bunch was cooled until two conditions were reached: its transverse emittance is reduced, and its average velocity reaches equilibrium with the electrons velocity. A small emittance was needed to render the ion bunch closer to a point-like condition, which eased the measurement of the average cooling force. Once

these conditions were reached, a velocity difference between ions and electron was induced by suddenly changing the electrons kinetic energy by acting on the voltage of the electron gun grid. This velocity difference induced a fresh cooling force that could be measured by tracking the variation of the ions momentum in time, for different ion-electron velocity differences. The force is indeed $F = \Delta p/\Delta t$. Figure 104 shows the reconstructed momentum (left) and a flat plot of the cooling force for different electron velocities (right). In this case, a $^{208}Pb^{54+}$beam was used. The ion-electron velocity difference was measured as the difference in equilibrium ion momentum before and after the electron velocity step. The cooling force was measured as the time derivative of the ion momentum during the first 50 ms after the step. When the relative ions-electrons velocity is large, the ions feel the full range of forces as visible in Fig. 104 (Left).

The same measurement was simulated with RF-Track. The simulation setup reflected the experimental conditions. To achieve good match with the measured cooling force, the following parameters were used: electron density $N_e = 4 \cdot 10^{13}\ e^-/\mathrm{m}^3$, transverse and longitudinal electron beam temperatures respectively of $T_\perp = 0.01$ eV and $T_\parallel = 0.001$ eV. In these simulations, the response of the electrons velocity was assumed to be instantaneous.

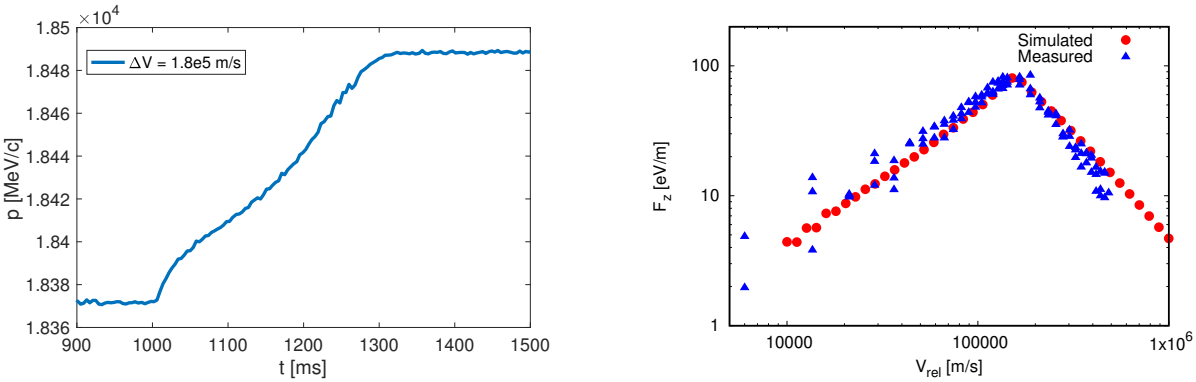

Figure 104: Left: ion mean momentum as a function of time during a measurement starting from ion-electron velocity difference of $1.8 \cdot 10^5$ m/s. Right: the measured cooling force versus the simulated one, as a function of the ion-electron velocity difference.

The variation of the cooling force was also studied as a function of the electron beam current and electron beam profile (from flat, $V_{co}/V_{gr} = 0.2$, to completely hollow, $V_{co}/V_{gr} = 1$, distribution). The result of the measurement is shown in Fig. 105. The theoretical expression of the cooling force shows a linear proportionality with the electron beam density. In addition to such a dependence with the electron beam current, the measurements also showed a shift of the peak with respect to the velocity axis. This could be explained by several effects within the electron gun, e.g. variations of the transverse temperatures with the electron current. Besides, also the response of the electron gun to a variation of the grid potential is not instantaneous, but requires a finite time to reach its target.

7.2.2 Ion acceleration with the Electron Cooler

Emittance blow-up and losses associated to space charge and IBS are observed when the beam is captured in RF buckets. We explored whether capturing at a higher momentum

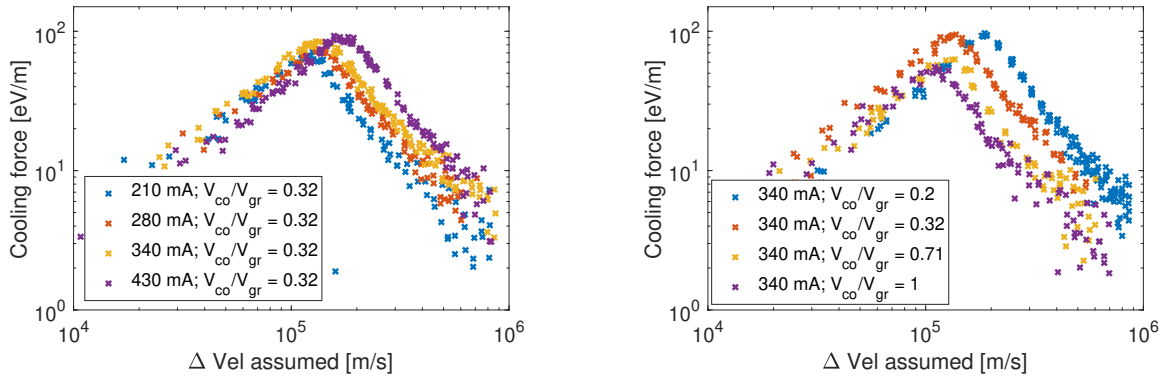

Figure 105: The measured cooling force for different electron beam currents (left) and electron beam profiles (right). Low value for V_{co}/V_{gr} corresponds to a flat e-beam distribution, while $V_{co}/V_{gr} = 1$ corresponds to a completely hollow distribution. $V_{co}/V_{gr} = 0.32$ is close to the operational settings for the NOMINAL cycle (see Sec. 5.3.2).

would be useful to prevent these losses. As Linac 3 could not inject at a higher energy, we aimed to accelerate the coasting beam during the injection plateau by means of the electron cooler. To do so, after the ion beam was cooled to equilibrium, the electron kinetic energy was modified by changing the cathode potential, creating a velocity difference between ions and electrons such that the ions are accelerated towards the new electron velocity (Fig. 106). The fields of all magnets in the ring had to be adapted to the changing momentum of the ion beam to ensure that the orbit stayed centered. A momentum increase of 6% could be achieved in the 1.3 s duration of the injection plateau, with no significant beam loss (52).

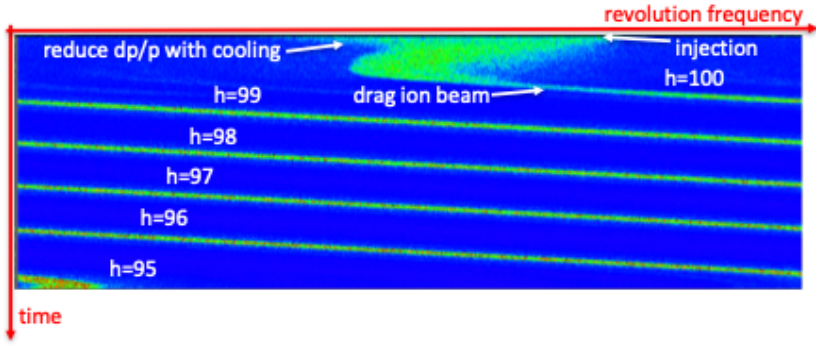

Figure 106: Ion beam acceleration as measured with the longitudinal Schottky system: the increasing beam velocity is observed as a change of revolution frequency such that lower harmonics (h) of the beam signal are observed in the selected frequency range.

We could prove that with a careful setting of the machine parameters it is possible to accelerate a coasting ion beam and capture it at a higher momentum. However, the achieved increase in momentum was not sufficient to significantly reduce emittance growth at RF capture compared to the standard cycle.

7.2.3 Ion acceleration with phase displacement

Phase displacement acceleration was used in the Intersecting Storage Rings to accelerate circulating proton beams without bunching (53). To achieve this the RF frequency is swept from $+\Delta f$ to $-\Delta f$ so that an empty bucket passes through a coasting beam. At each passage of the bucket the beam gains approximately $H_B/2$ of energy, where H_B is the bucket height. This could be used in conjunction with electron cooling to increase the rate at which the coasting beam is accelerated.

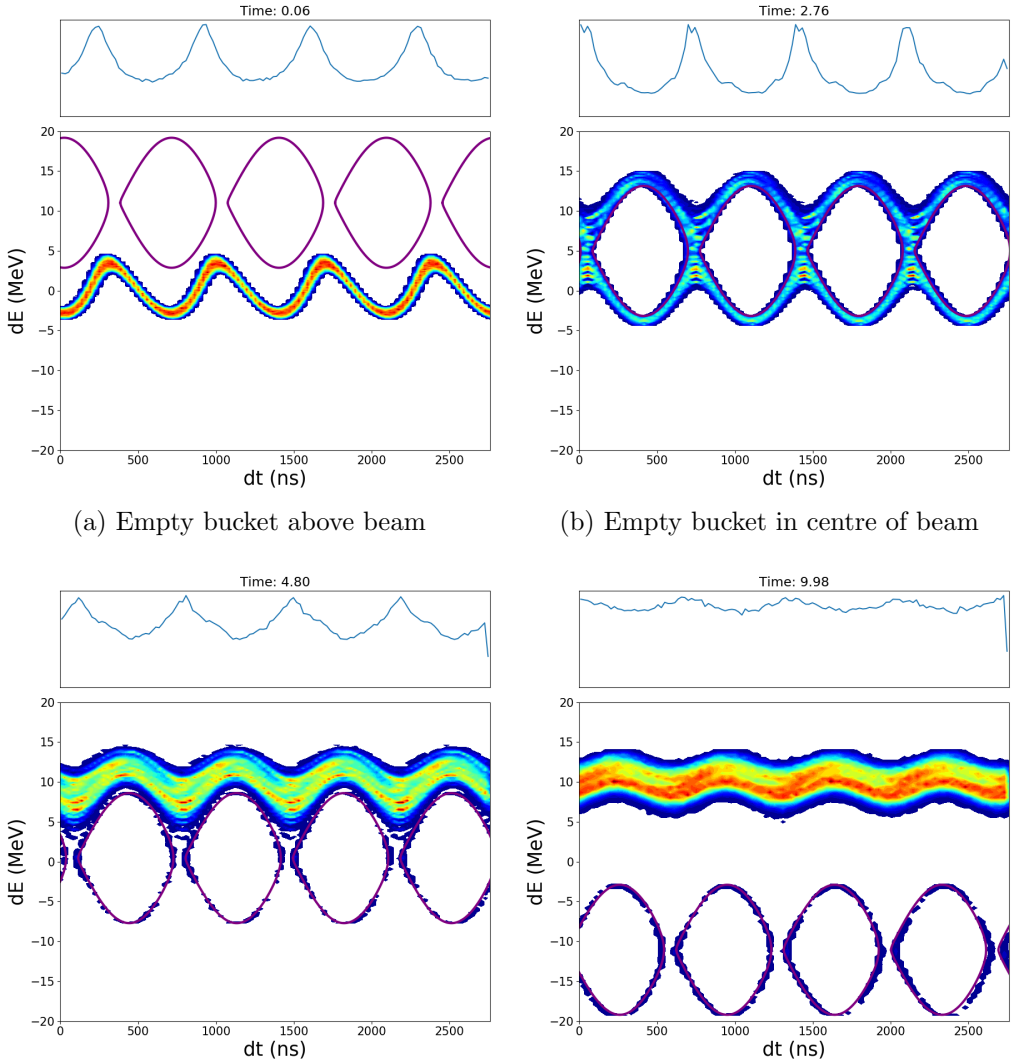

(a) Empty bucket above beam

(b) Empty bucket in centre of beam

(c) Empty bucket at end of passage

(d) Empty bucket prior to drop of RF voltage

Figure 107: Stages of phase displacement acceleration with single passage.

Simulations using the longitudinal beam dynamics code BLonD (54) have been used to show that phase displacement acceleration (PDA) may be possible in LEIR. Figure 107 shows four moments during a simulation of PDA over 10 ms, which raises the coasting beam energy by approximately 10 MeV. It is important to note that PDA will increase the average energy spread of the bunch, however by combining it with e-cooling this effect should be

suppressed. Additionally, as the empty bucket passes through the beam there are peaks created in the line density, this may have a negative effect on the transverse plane depending on the size of the peaks and how long they persist.

In order for the PDA to be useful, multiple steps would be necessary. This could be achieved by alternating between PDA and steps in the magnetic field, which would enable the beam to be kept approximately centred in the beam pipe and allow a greater increase in the average energy. Figure 108 shows how a series of steps in magnetic field results into a step increase in momentum (blue) and RF frequency offset (red).

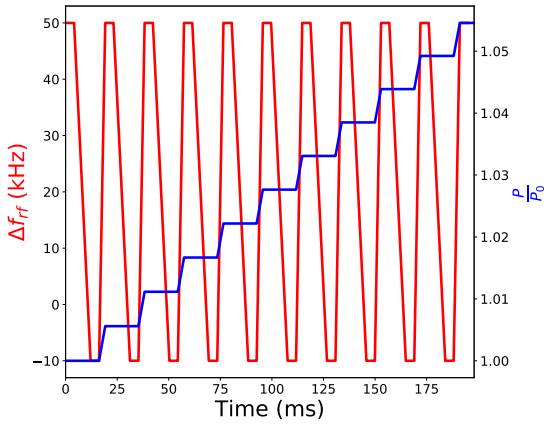

Figure 108: Phase Displacement Acceleration: a series of steps in momentum (blue) and RF frequency offset (red) that can be combined to increase the beam momentum.

The initial and final phase space distribution after the multi-step PDA using the settings in Fig. 108 is shown in Fig. 109. From Fig. 109 it can be seen that more than 100 MeV of kinetic energy, corresponding to approximately 6% momentum increase, can be added to the beam in approximately 200 ms compared to 1.3 s using the e-cooler alone.

It should be noted that, along with the energy spread increase seen with single step PDA, there is also a small number of particles that become trapped on the separatrix as it passes through the beam, these are then left at lower energy when the RF voltage is reduced to zero.

With a more optimal multi-step PDA, combined with e-cooling, it is expected that a faster acceleration of the beam with less negative effects should be possible. This will be studied in simulation and MD in the future.

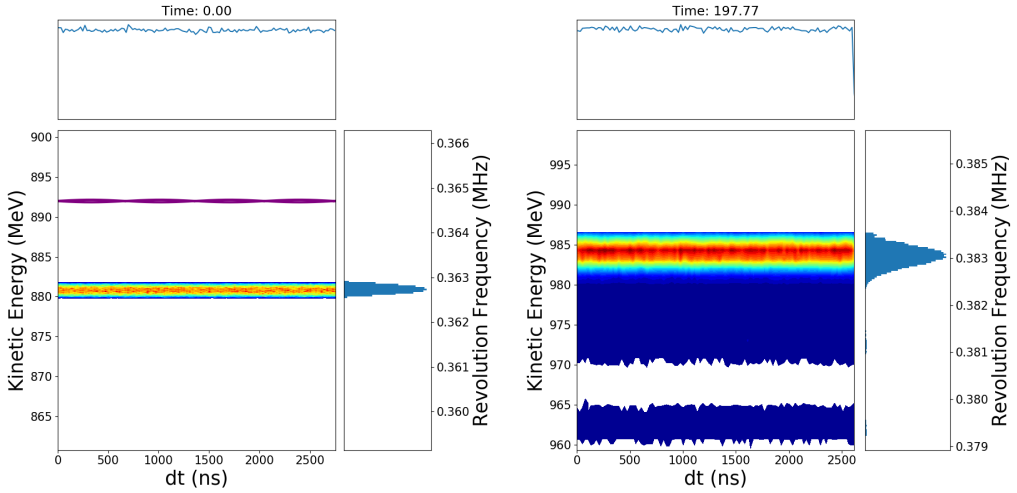

(a) Initial distribution (b) Final distribution

Figure 109: Initial and final states with mutli-step phase displacement acceleration. More than 100 MeV of kinetic energy increase can be achieved by combining multi-step PDA and electron cooling.

7.2.4 Cooling of a bunched beam

Electron cooling in LEIR is applied on coasting beams, before the RF-capture takes place, to reduce the transverse emittance and the momentum spread. We explored whether cooling during and after the RF-capture could be useful to reduce the transverse emittance blow-up and losses caused by space charge and IBS. However, cooling a bunched beam also reduces the bunch length, increasing the beam density and making it more prone to collective effects.

By adjusting the gun voltage of the electron gun, the revolution frequency of the ion beam can be varied, creating an offset compared to the frequency given by the RF, as shown in Fig. 110 on the left.

In order to have sufficient time to study the cooling of a bunched beam, the number of injections was reduced from 7 to 5, the duration of cooling was extended and the RF capture was advanced. The resulting longitudinal distribution can thus be changed from parabolic to flat and hollow (Figs. 110, 111, 112).

To calibrate the resulting beam revolution frequency to the voltage of the electron cooler gun, the RF-cavity was switched off. After setting a specific voltage to the gun, the revolution frequency of the beam was measured with the Schottky pickup. Combining different values of the voltage a calibration curve, shown in Fig. 113, was obtained.

The losses, as a function of the revolution frequency set by the electron cooler, were studied for low intensity beams ($\sim 3 \cdot 10^8$ ions) with both single and double harmonic. For the double harmonic, losses below 4% were measured between the capture and the beginning of the ramp when a flat distribution was produced, while ∼20% were measured for the single harmonic (Figure 114).

On the other hand, for high intensities ($> 6.5 \cdot 10^8$ ions) and for the double harmonic, which was our best case for low intensity, losses were above 35%, as can be seen in Fig. 115.

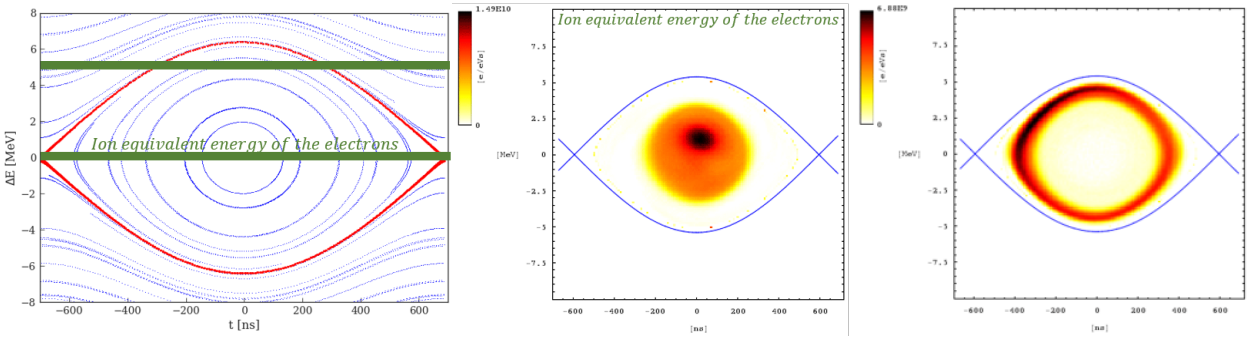

Figure 110: On the left, longitudinal dynamics when the RF acts on the beam: the green lines represent the energy set by the electron cooler and expected by the RF. At the centre, longitudinal phase space of a beam where the velocity of the ions is matched to the RF frequency, on the right, a beam with an offset with respect to the RF frequency creating a hollow distribution.

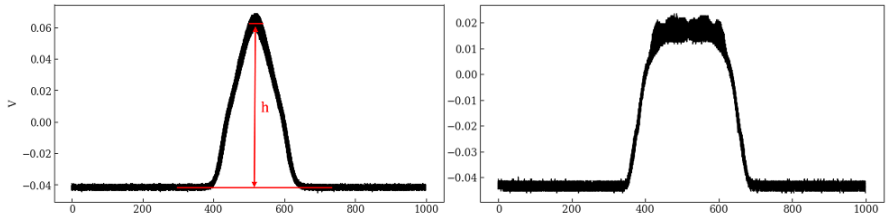

Figure 111: Longitudinal profiles for single harmonic. Well centred beam for $v_{ions} = v_{e^-}$ (left) and flat beam (right).

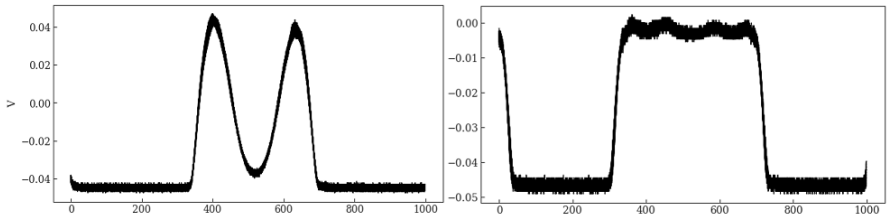

Figure 112: Longitudinal profiles for double harmonic. Well centred beam for $v_{ions} = v_{e^-}$ (left) and flat beam (right).

The results show that for low intensity, the losses between the RF-capture and the ramping were ∼20% when a flat distribution was produced for the single harmonic and ∼4% for the double harmonic. The measurements were repeated for high intensity for the double harmonic and showed losses of more than 35%.

In summary, even though the losses for low intensities could help us reduce the losses during the capture, no reduction of losses could be achieved with high intensity beams.

As aligning the e-cooler equivalent frequency with the RF frequency causes the line density to become significantly peaked it is possible that with a suitable longitudinal heating force the unwanted peak in line density can be reduced, whilst maintaining the cooling effect transversely. RF phase noise is used operationally in the SPS and LHC for longitudinal

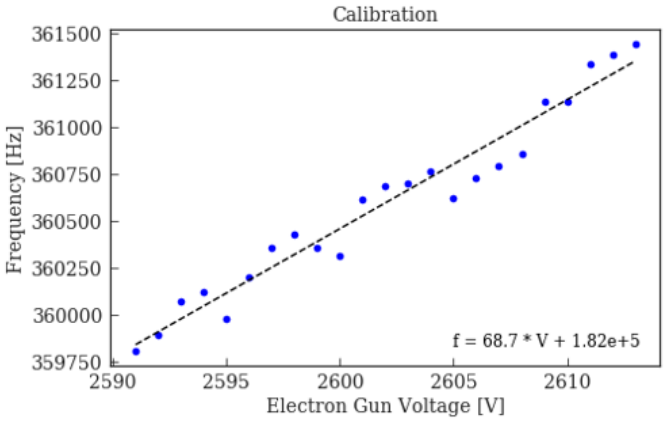

Figure 113: Calibration curve between the electron cooler gun voltage and the revolution frequency.

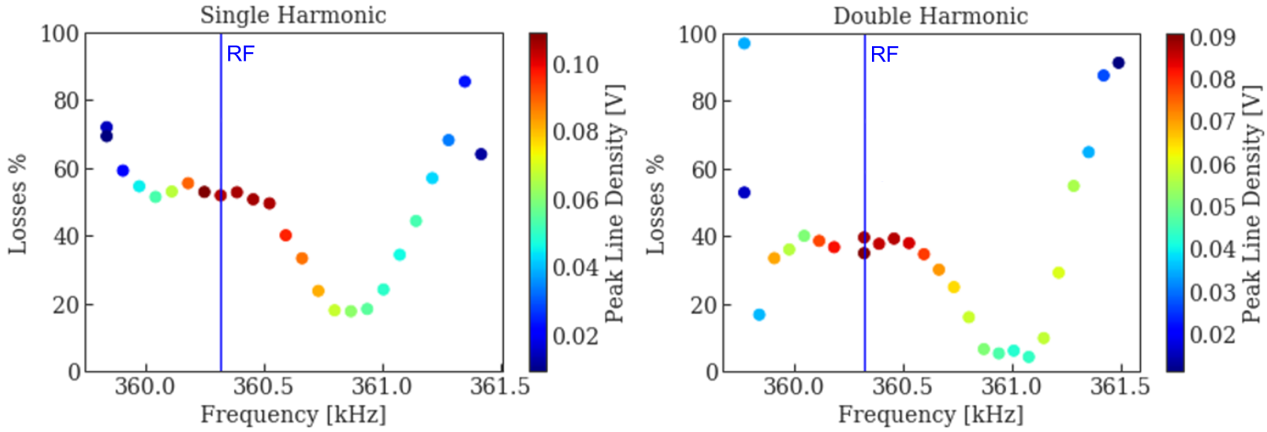

Figure 114: Losses for single and double harmonic as a function of the revolution frequency set by the electron cooler. When the frequency coincides with the RF-frequency the bunch length is strongly reduced and large losses are produced. The minimum losses are found for a frequency for which a flat longitudinal distribution is produced. For large frequency offsets the beam is no longer captured by the RF-bucket.

emittance blow-up, and after a successful reliability run in the PSB in 2018 will also be used after LS2. In LEIR phase noise could provide the heating force needed to prevent excessive increase in longitudinal phase space density during bunched beam cooling.

A BLonD simulation was set up starting with a very longitudinally dense distribution, to which phase noise was applied. Figure 116 shows the initial and final states of the distribution after 100 ms of RF phase noise was applied. Figure 116b shows that significant longitudinal emittance blow-up can be achieved when starting from a very dense distribution (Fig. 116a), it will be studied in MD if phase noise can provide sufficient heating force to counteract the effect of e-cooling in the longitudinal plane.

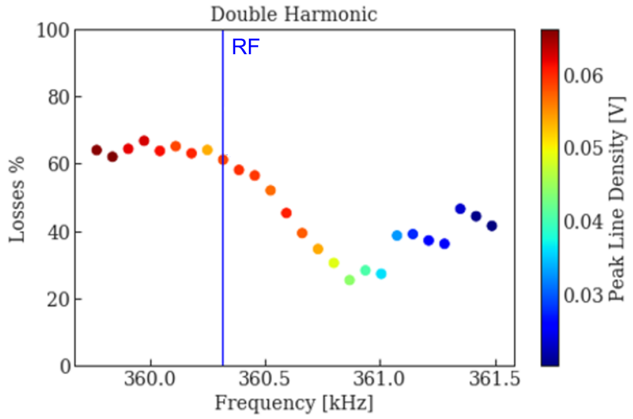

Figure 115: Losses for high intensity and double harmonic as a function of the revolution frequency.

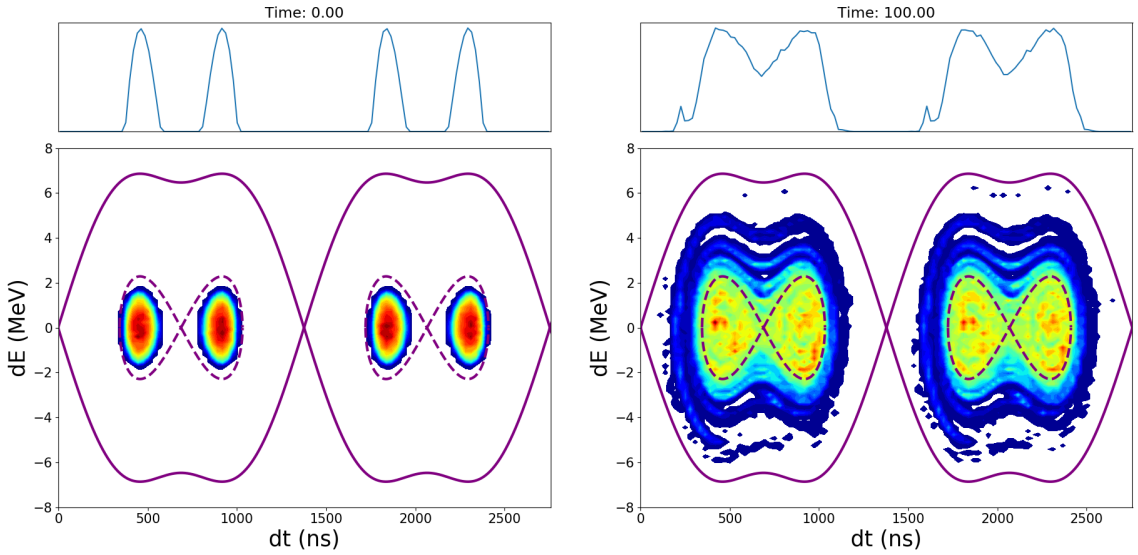

(a) Initial distribution

(b) Final distribution

Figure 116: Initial and final states of BLonD simulation of longitudinal emittance blow-up via RF phase noise.

7.2.5 Cooling maps and equilibrium emittances

Electron cooling reduces the transverse emittances and momentum spread of the beam to the equilibrium values. The equilibrium values were studied as a function of a bump on the ion beam orbit in the cooler section with the following cooling parameters: electron beam current (210, 340 and 430 mA) and electron beam distribution (parabolic, flat and hollow). An example of the cooling maps created as a function of a horizontal bump of the ion orbit is shown in Fig. 117 for a flat electron distribution and 340 mA electron current. It can be observed how the horizontal equilibrium emittance increases with the horizontal angle between the ion and electron beams. The smallest emittance is found for a horizontal bump

with zero angle and an amplitude of around 10 mm, as also shown for the NOMINAL beam in Sec. 5.10.

On the other hand, the vertical equilibrium emittance is independent of the horizontal angle between the ion and electron beams, as expected, and the vertical emittance increases as the overlap between the ion and electron beam decreases. Finally, it can also be seen how the final momentum of the beam depends on the the overlap between the ion and electron beams.

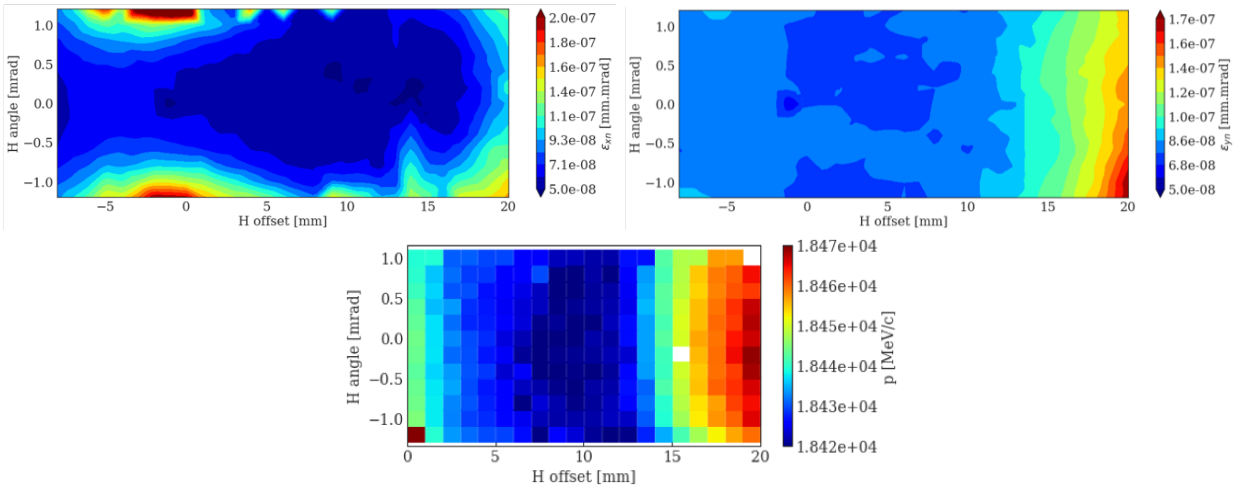

Figure 117: Horizontal equilibrium emittance (left), vertical equilibrium emittance (right), and mean momentum (bottom), as a function of a bump on the ion beam orbit, for a flat electron beam distribution and 340 mA electron current.

The equilibrium emittances were also studied as a function of the ion beam intensity and the tunes of the machine. The ion beam intensity was varied in a continuous manner by mis-steering the ETL.BHN10 dipole in the transfer line and reducing the injection efficiency. The transverse equilibrium emittances and the momentum spread were found to increase with intensity proportionally to I^n. For the nominal working point ($Q_x = 1.82$, $Q_y = 2.72$) the exponent $n \propto 0.4 - 0.6$, as shown in Fig. 118 (left) for the vertical equilibrium emittance. Similar results were obtained in the GSI laboratory for other ion species ($Ti^{22+}, Kr^{36+}, Xe^{54+}, Au^{79+}, U^{92+}$) in the case of IBS dominated beams (55). However, when the equilibrium values were measured as a function of the ion beam intensity for a vertical tune close to an excited resonance, a large increase of the exponent n was found above a threshold intensity, as shown in Fig. 118 (left). This behaviour can be explained when considering the space charge tune spread. For certain working points and above a given intensity the particles can get trapped in an excited resonance causing a large increase of their emittance, as shown in Fig. 118 (right).

7.2.6 Planned improvements

Several MDs have been performed with the aim of either characterising the electron cooler or *shaping* the beam for other studies (e.g. IBS, space charge, RF capture). A number of improvements have been planned (56; 57) in order to improve the performance of the

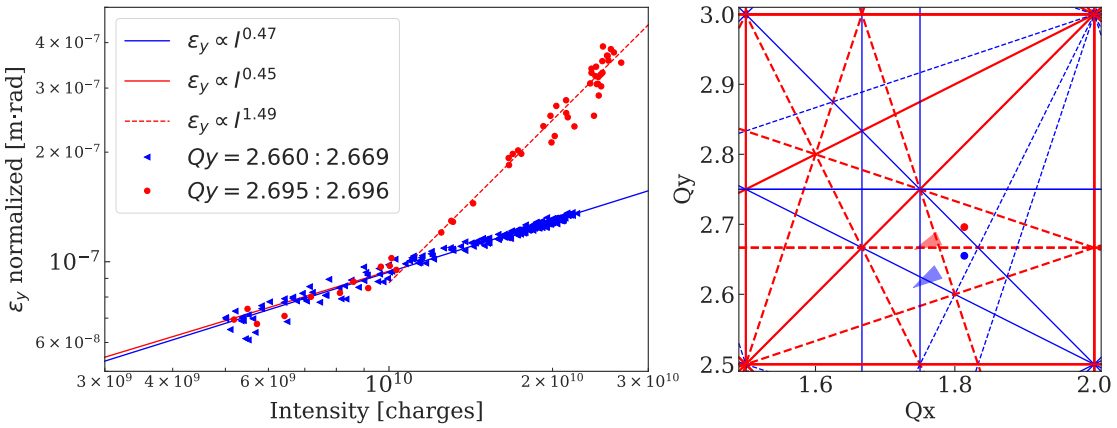

Figure 118: Left: vertical equilibrium emittance as a function of the beam intensity for vertical tunes not affected by the excited resonance at $Q_y = 2.666$ (blue dots) and affected by the excited resonance (red dots). Right: resonance diagram showing the bare tunes and the space-charge tune spreads for the maximum intensity.

electron cooler like checking the GFA (Générateur de Fonction Analogique) modulation of cathode and grid power supplies and re-installing the coupling transformer for grid electrode modulation. This would enable the measurement of the electron beam position, improving the control of the alignment with respect to the ion beam. A new faster switching system is also under development and tests will be made when the machine will restart: if successful it could also be used to modulate the beam intensity.

7.3 Impedance and instability studies

In 2018, the instability studies mainly focused on the identification of the source of the fast vertical instability in LEIR (58; 59). The instability, also observed in the past (see e.g. (60)) occurs when the transverse feedback is switched off, and presents a rise time significantly shorter (more than 100 times) than the one predicted by the current machine impedance model, preventing the accumulation of more than 1 or 2 injections. Because of this, until 2018, LEIR could not be operated without a vertical feedback active on the full injection plateau as shown in Fig. 119.

In 2018, the instability was systematically studied and observed with the vertical Schottky spectrum analyzer. In addition to the past studies, it was possible to observe a repetition pattern on the Schottky spectrum, pointing to coherent lines resonating on multiples of $\simeq$2 MHz (see Fig. 120 on the left). The pattern can be associated with the typical response of a mis-matched transmission line. Quasi-TEM modes can be sustained only in stripline-like devices, and that is the reason why all the LEIR used and un-used pickups terminations were systematically checked with the help of BE/BI.

A detailed investigation was performed and obsolete mis-matched devices were identified. Among these, the ER.UQFHV41, an old LEIR pickup used for beam transfer function measurements, was disconnected and matched after the second technical stop. Repetitive plug in/out tests were done confirming the source of the instability as shown in Fig. 121.

As can be observed from Fig. 120, the repetitive pattern observed when the device was

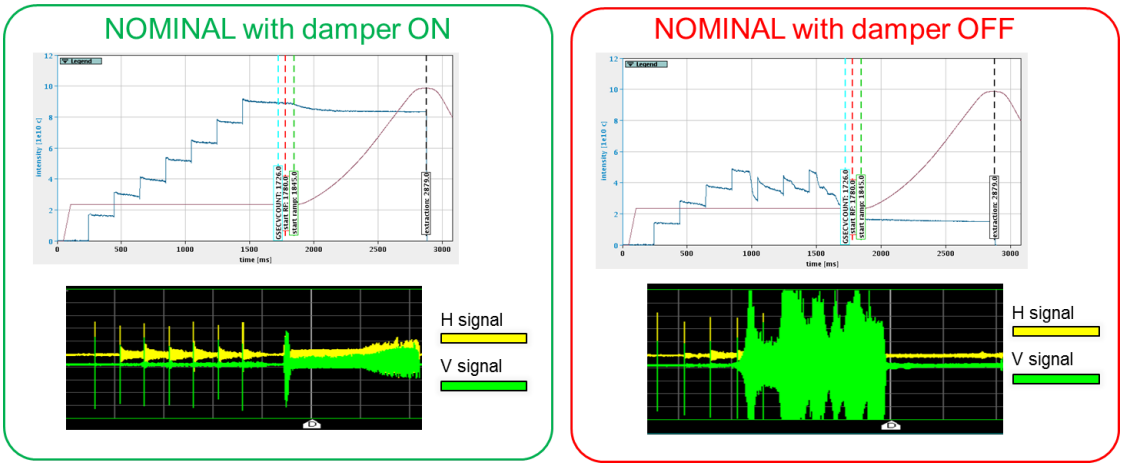

Figure 119: LEIR intensity along the cycle together with the corresponding "activity" signals measured from the transverse feedback pickup. On the left, with active damper only the injection related spikes and activity at capture are visible, on the right, switching off the damper, a fast vertical instability arises inducing large beam loss.

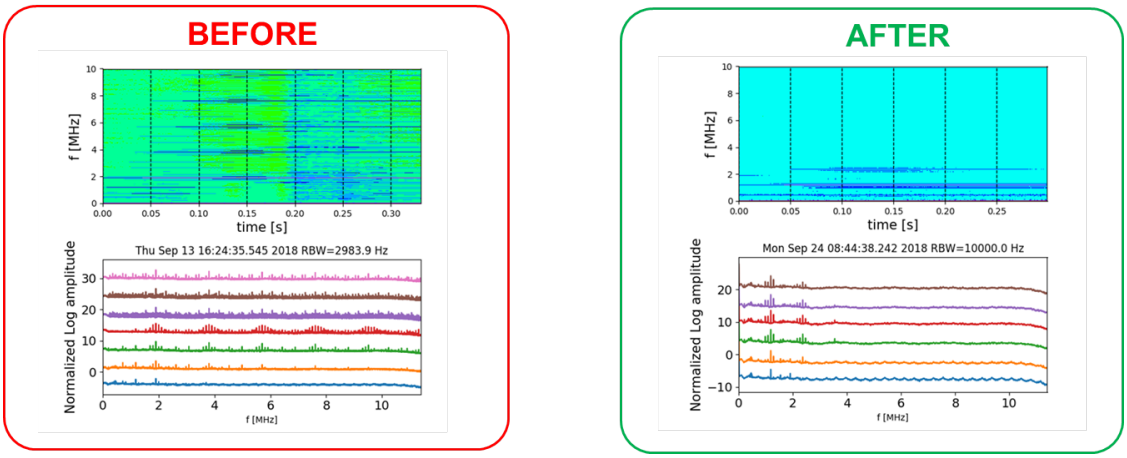

Figure 120: LEIR spectrum along the cycle before and after the termination of the ER.UQFHV41 device. On the top, waterfall frequency spectrum as a function of time, on the bottom, selected spectral pattern on the corresponding dashed lines of the waterfall plot. The coherent lines resonating at ≃2 MHz and multiples are suppressed.

mis-matched is now suppressed. Some resonating pattern is still visible at different frequencies, which could point to similar issue on other machine pickups: a systematic cross-check on other stripline pickups (e.g. the the transverse damper ones) is planned for the restart in 2021 (61).

7.4 Longitudinal beam dynamics studies in 2018

Longitudinal beam dynamics studies in 2018 focused on methods to improve beam transmission through the machine. The two main areas of interest were a faster magnetic cycle, and operation with three harmonics to further increase the bunching factor, without increasing

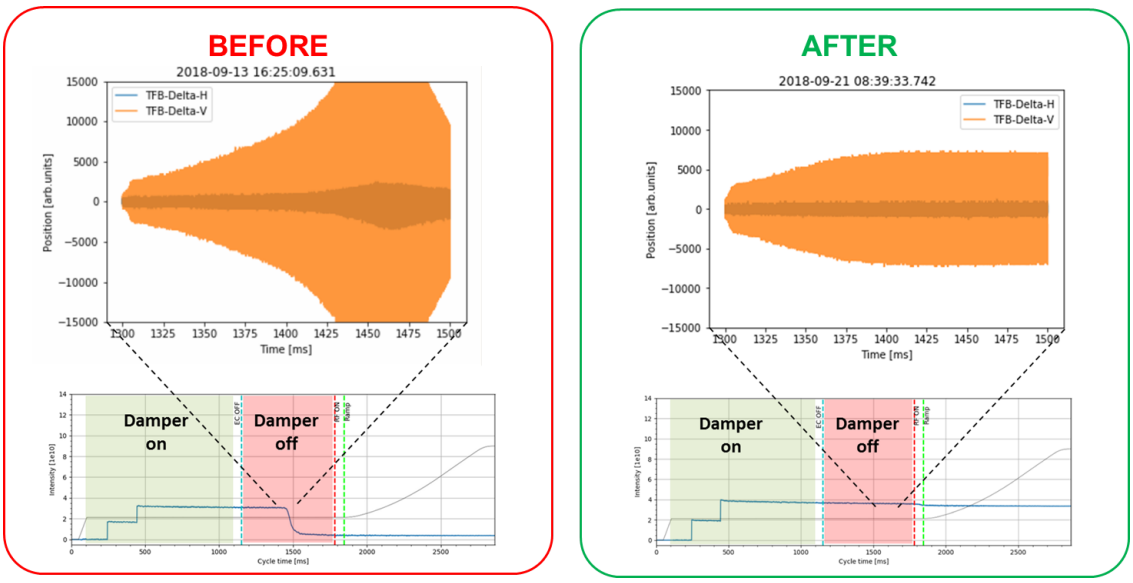

Figure 121: LEIR intensity along the cycle before and after the termination of the ER.UQFHV41 device. The instability without feedback is clearly suppressed.

the longitudinal emittance. In addition, there have been some preliminary simulations to direct the machine development studies planned during Run 3 (62).

7.4.1 Fast ramp cycle with 8 injections

The acceleration cycle in LEIR has a gentler start than necessary, and so a test was done with a faster ramp. Using a faster ramp was expected to have two benefits; first, by increasing the $\beta\gamma^2$ faster the space charge would be reduced, which is expected to reduce transverse losses; second, with a faster ramp the extraction time can be maintained but the flat bottom lengthened, allowing an 8^{th} injection if necessary. Figure 122 shows the original (red) and new (blue) magnetic cycles.

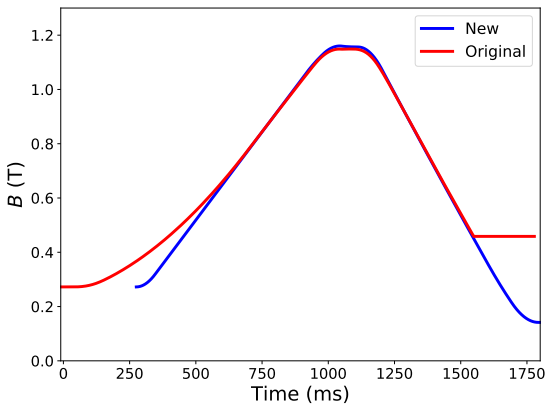

Figure 122: Comparison of the original magnetic cycle and the fast magnetic cycle.

When increasing the ramp rate it is necessary to ensure that adequate RF voltage will

be available to contain the required longitudinal emittance. Figure 123 shows the voltage required at h=2 to maintain a 12 eVs bucket area from the start of acceleration to arrival at the flat-top. There is a small modulation visible on the voltage function for the original cycle, this is not physical but is due to measurement noise. After setting up the fast ramping cycle a new intensity record of 10.5×10^{10} charges was achieved. However, due to operational constraints it was not possible to further optimise the cycle to use it operationally: further activity is therefore planned for post-LS2.

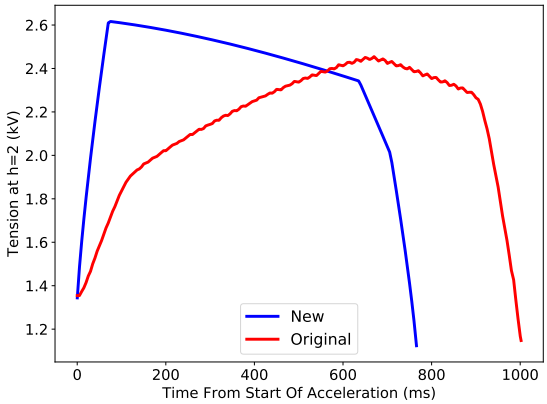

Figure 123: Comparison of the voltage functions that would be required to have acceleration at h=2 with constant 12 eVs bucket area.

7.4.2 Operation with h = 2+4+6

Operationally, the high intensity cycle (NOMINAL) uses 2 harmonics, either h=2 and h=4, or h=3 and h=6 to accelerate and shape the beam respectively. The 4th or 6th harmonic is used in anti-phase with the 2nd or 3rd harmonic to reduce the line density of the bunch, increasing the bunching factor and reducing the effect of space charge. When accelerating two bunches (h=2+4) it is possible to add h=6 to increase the bunching factor even more, therefore further reducing the effect of space charge. Figure 124 shows the tomoscope waterfall at capture with h=2+4 (Fig. 124a) and h=2+4+6 (Fig. 124b).

The 6^{th} harmonic makes slightly longer bunches and brings an additional 5% intensity transmitted with respect to a nominal h = 2+4 cycle. The setting up requires a bit more voltage from the cavities, and both, CRF41 and CRF42, need to be used. The draw back is that there will no longer be a hot spare. However, in the event that a cavity fails, reverting to standard h = 2+4 operation would be possible. It would not be possible to produce 3 bunches with this scheme as h = 9 would be required, which is outside the cavity frequency range. With split and merging in the ramp, 3 bunches could be produced, but this would require substantial LLRF modifications.

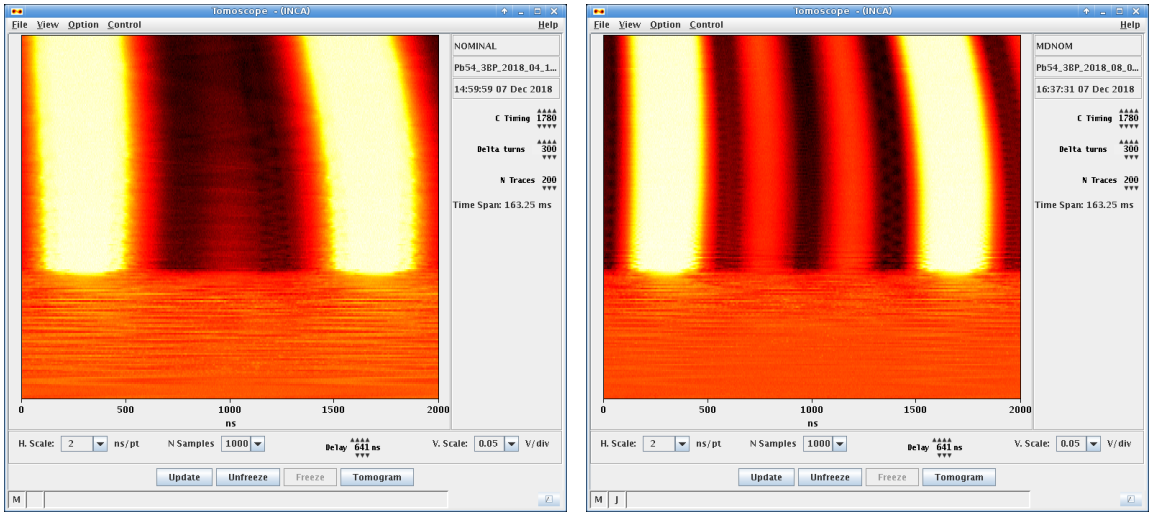

(a) h=2+4 (b) h=2+4+6

Figure 124: Capture comparison h=2+4 and h=2+4+6.

8 Conclusions

A detailed description of the LEIR improvements and achievements during the 2018 run have been presented in this document.

As described in Sec. 2, the operation largely profited from the hardware and software upgrades of the machine. The use of automatic optimization tools eased the accelerator operation and performance recovery. Complex machine learning algorithms are currently being tested to allow faster recovery in case of performance degradation. The new BPMs in the transfer lines allowed easier steering of the injection line, detection of the source of large orbit errors, and monitoring of the energy ramping effectiveness. All the BPMs will be commissioned during 2020 in their actual high frequency operation mode. The new Schottky acquisition system and data processing allowed the injected energy distribution from Linac 3 to be monitored and recording of failure events correlated with the stripper foils degradation. The upgrade of the FESA class is currently being performed which will allow an online use of the tool. The orbit first-turn and turn-by-turn mode of operation were tested for the first time and will be finalized at the machine restart. In particular, the turn-by-turn mode triggered a study for a new kicker system for optics measurements. The new beam dump system was fully commissioned and the temperature rise recorded is well within the specifications. Large improvements were also done on the LSA generation for the $B\rho$ and the management of machine septum parameters. Currently, additional efforts are being made to integrate the LEIR LLRF in the LSA settings management and generation framework, together with damper and electron cooler parameters. This will allow the operation of the systems using high level physics parameters like bucket area, electron velocity, etc. The commissioning of new FGCs of the ring bendings and quadrupoles, is part of the LEIR standardisation and reliability improvement, and it will take place during the hardware commissioning in 2021.

From the RF point of view, the LLRF clocking scheme was upgraded from sweeping to fixed frequency scheme, the frequency program profited from an optimised numerical

implementation, and the frequency offset modulation was moved to DSP for easier parameter control and archiving.

The new LEIR B-train has been fully commissioned and tested through a year-long reliability run, which proved the stability of the system and the advantages related to the improved accuracy brought from the newly installed coil sensors and electronics. Enhanced real time correction of temperature effects and calibration are foreseen at the restart. Observations seem to have put in evidence a large B field decay, which complicated the machine optimization and operation: this could be related to edge effects of the main bendings and additional probes have already being installed to probe the field behaviour once the machine will restart.

From the operation point of view, the main steps of the high intensity NOMINAL beam setup were clearly identified improving substantially the machine reproducibility and the capability of performance recovery in case of perturbations (temperature fluctuation, stripper foils issue, instabilities, etc.). The LEIR injection efficiency was found to be very sensitive to the Linac 3 LLRF settings. These are being upgraded with new LLRF diagnostics which will help to identify long term drifts and improve the reliability of the system. Stray fields from the PS, known to affect the injection efficiency in LEIR, were corrected both on a cycle-by-cycle basis (with the so called *autopilot*) and on a super-cycle basis (with the so called *equalizer*). These mainly correct the effect of the stray fields on the injection line horizontal trajectory acting on the ETL.BHN10 magnet. Additional correctors, in particular for the V plane, are being identified together with a solid algorithm for stray field correction. The stripper foil lifetime has been closely monitored, and the strategy of stripper foil exchange every two weeks has been implemented in order to have stable operation. The horizontal bump in sector 4 has been found to be very effective in mitigating vacuum pressure rise, as also observed in the past. In order to improve the understanding of the source of the issue, beam dynamics simulations are planned during LS2 with the updated machine aperture model. A deeper understanding of the electron cooler settings allowed optimization of the machine for high accumulated and extracted intensity. The possibility of measuring the electron beam position, and switching on the cooler gun to allow more precise cooling force measurements, is presently under investigation.

The largest part of these improvements occurred prior to the LHC ion run, allowing a smooth preparation of the high intensity NOMINAL beam (both in 2+4 and 3+6 flavours) to deliver to the ion chain. Accounting for the full LHC run, the extracted intensity was $9.1{\cdot}10^{10}$ charges on average, with a typical value of $9.4{\cdot}10^{10}$ charges. In the case of NOMINAL 3+6, whose operation followed the one of NOMINAL 2+4, the performance largely profited from the previous setup allowing for extracted intensity of $8.9{\cdot}10^{10}$ charges on average and with a typical value of $9.4{\cdot}10^{10}$ charges. The performance of the machine has been tracked with the help of a dedicated website and it is now followed up within a CERN forum.

From the machine development, significant effort was put on the study of the interplay of space charge and IBS on the capture losses. The compensation of the resonance at $Q_y = 2.66$ clearly showed a significant emittance growth which could be due to IBS. The measurement of the emittance growth in coasting and bunched beam was found to be in very good agreement with respect to IBS simulations only in the horizontal plane. On the vertical plane, part of the disagreement could be due to a significant distortion of the IPM signal from ion beam space charge on the ionised gas. Simulation studies are in progress in order

to quantify and eventually cure this effect. The possibility of further reducing the capture losses was investigated with electron cooler acceleration, phase displacement simulations and bunched beam cooling. At the moment the gain is only marginal. On the other hand, a cycle with a faster ramp will be investigated at the restart of the machine after LS2. In 2018 the source of the fast coherent vertical instability was identified thanks to a careful check of the stripline pickup terminations: the old BTF pickup was matched and the instability suppressed. A horizontal instability was observed, in particular during the LHC run, and suppressed by adjusting of the horizontal bump in the cooler. Simulations are in progress in order to assess the stability margins against it.

9 Abbreviations

The following abbreviations are used in this manuscript:

AD	Antiproton Decelerator
ADC	Analog-to-Digital Converter
BCT	Beam Current Transformer
BPM	Beam Position Monitor
BTF	Beam Transfer Function
CGAFG	Controls Generic Arbitrary Function Generator
CTIM	Central TIMing
CVORB	Arbitrary waveform generator
DC	Direct Current
DSP	Digital Signal Processing
EE	from LEIR to ETL - LEIR extraction line
EI	from ETL to LEIR - LEIR injection line
ELENA	Extra Low Energy Antiproton ring
ETL	LEIR injection and extraction line
ETP	LEIR to PS transfer line
FE	Finite Elements
FESA	Front-End Software Architecture
FFT	Fast Fourier Transform
FGC	Function Generator/Controllers
FMR	Ferro-Magnetic Resonance
GCPW	Grounded Coplanar Waveguide
GFA	Générateur de Fonction Analogique
GUI	Graphical User Interface
HLRF	High Level RF
IBS	Intra Beam Scattering
ITE	Ions to LEIR transfer line
IPM	ionization Profile Monitor
LEAR	Low Energy Antiproton Ring
LEIR	Low Energy Ion Ring
LHC	Large Hadron Collider
LIU	LHC Injectors Upgrade
LLRF	Low Level RF
LS2	Long Shutdown 2
LSA	LHC System Architecture
MAD	Methodical Accelerator Design
MD	Machine Development
OASIS	Open Analogue Signal Information System
PCI	Peripheral Component Interconnect
PDA	Phase Displacement Acceleration
PLC	Programmable Logic Controller

PPM	Pulse to Pulse Modulation
PS	Proton Synchrotron
PSB	PS Booster
RBAC	Role-Based Access Control
RF	Radio Frequency
RL	Radial Loop
RMS	Root Mean Square
SEM	Secondary Emission Monitor
SPS	Super Proton Synchrotron
TEM	Transverse Electro-Magnetic
WR	White Rabbit
YASP	Yet Another Steering Program
YETS	Year-End Technical Stop
YIG	Yttrium Iron Garnet

References

[1] H. Damerau, A. Funken, R. Garoby, S. Gilardoni, B. Goddard, K. Hanke, A. Lombardi, D. Manglunki, M. Meddahi, B. Mikulec, G. Rumolo, E. Chaposhnikova, M. Vretenar, and J. Coupard, "LHC Injectors Upgrade, Technical Design Report, Vol. I: Protons," Tech. Rep. CERN-ACC-2014-0337, CERN, Geneva, Switzerland, Dec 2014. http://cds.cern.ch/record/1976692.

[2] J. Coupard, H. Damerau, A. Funken, R. Garoby, S. Gilardoni, B. Goddard, K. Hanke, D. Manglunki, M. Meddahi, G. Rumolo, R. Scrivens, and E. Chapochnikova, "LHC Injectors Upgrade, Technical Design Report, Vol. II: Ions," Tech. Rep. CERN-ACC-2016-0041, CERN, Geneva, Switzerland, Apr 2016. https://cds.cern.ch/record/2153863.

[3] M. J. D. Powell, "An efficient method for finding the minimum of a function of several variables without calculating derivatives," *The Computer Journal*, vol. 7, pp. 155–162, 01 1964. http://dx.doi.org/10.1093/comjnl/7.2.155.

[4] J. A. Nelder and R. Mead, "A Simplex Method for Function Minimization," *The Computer Journal*, vol. 7, pp. 308–313, Jan. 1965. http://dx.doi.org/10.1093/comjnl/7.4.308.

[5] M. Benedikt, P. Collier, V. Mertens, J. Poole, and K. Schindl, eds., *LHC Design Report, Vol.3*. CERN Yellow Reports: Monographs, 2004, CERN, Geneva, Switzerland. https://cds.cern.ch/record/823808.

[6] L. Søby, G. Baud, M. Bozzolan, and R. Scrivens, "New Beam Position Monitors for the CERN LINAC3 to LEIR Ion Beam Transfer Line," in *Proceedings, 7th International Beam Instrumentation Conference (IBIC 2018)*, September 9-13, 2018, Shanghai, China. https://doi.org/10.18429/JACoW-IBIC2018-TUPB14.

[7] J. Tan, "Experimental Results from LEIR Schottky System," Tech. Rep. CERN-AB-Note-2008-013, CERN, Geneva, Switzerland, Mar 2008. https://cds.cern.ch/record/1093343.

[8] D. M. L. Alves *et al.*, "Status of Schottky FESA class," *LIU-Ions PS injectors Beam Dynamics Working Group*, 29-10-2019, CERN, Geneva, Switzerland. https://indico.cern.ch/event/859465/.

[9] G. Baud, O. Marqversen, and V. Kain, "Orbit and turn-by-turn system performances in 2018," *LIU-Ions PS injectors Beam Dynamics Working Group*, 12-03-2019, CERN, Geneva, Switzerland. https://indico.cern.ch/event/799313/.

[10] N. Biancacci and V. Kain, "Analysis of turn by turn data acquired in 2018," *LIU-Ions PS injectors Beam Dynamics Working Group*, 15-10-2019, CERN, Geneva, Switzerland. https://indico.cern.ch/event/855164/.

[11] O. Marqversen, "First Turn Trajectory," *LIU-Ions BDWG*, 09 2018. https://indico.cern.ch/event/756879/.

[12] C. D. Paolo *et al.*, "Installation of an External Dump in the LEIR ETL Transfer Line, EDMS n.1746660," no. LEI-TD-EC-0001, 14-09-2017, CERN, Geneva, Switzerland. https://edms.cern.ch/document/1746660/1.0.

[13] E. Chaudet *et al.*, "LEIR dump drawings," no. ST0785371_01, 08-11-2017, CERN, Geneva, Switzerland. https://edms.cern.ch/document/1710404/AA.

[14] C. D. Paolo, "Thermo-mechanical analysis and conceptual design of the new beam dump in the LEIR facility at CERN," Tesi di Laurea Magistrale, Politecnico di Torino, 2019, CERN, Geneva, Switzerland. https://edms.cern.ch/document/1895238/1.

[15] A. Beaumont, M. Buzio, and G. Boero, "Ferrimagnetic resonance field sensors for particle accelerators," *Review of Scientific Instruments*, vol. 90, no. 6, 2019. https://doi.org/10.1063/1.5097508.

[16] C. Carli, "Magnetic cycle editing," Internal Communication.

[17] S. Hirlander, "LEIR_Magnetic_Cycle-generic," http://gitlab.cern.ch/LEIR-LN3/LEIR_Magnetic_Cycle-generic.ipynb.

[18] J. M. Cravero and S. Joffe, "Installation of MAXIDISCAP power converters for Linac3 and LEIR transfer line pulsed quadrupoles," EDMS 1841822 - L3-R-EC-0002, 09-10-2019, CERN, Geneva, Switzerland. https://edms.cern.ch/document/1841822/1.0.

[19] M. E. Angoletta, M. Jaussi, and J. Molendijk, "New LLRF capabilities and beam results for the second year of ELENAs commissioning," *CERN-ACC-NOTE-2019-0050*, 2019, CERN, Geneva, Switzerland. https://cds.cern.ch/record/2703432.

[20] C. Grech, M. Buzio, and N. Sammut, "A magnetic measurement model for real-time control of synchrotrons," *IEEE Transactions on Instrumentation and Measurement*, pp. 1–8, 2019. https://doi.org/10.1109/TIM.2019.2904073.

[21] N. Biancacci *et al.*, "Bfield decay observation and plans," *LIU-Ions PS injectors Beam Dynamics Working Group*, 05-11-2019, CERN, Geneva, Switzerland. https://indico.cern.ch/event/857598/.

[22] V. Kain and R. Scrivens, "BPMs and Additional Grids in the LEIR Injection Line," no. LEI-BP-ES-0001, p. 4 p, 06-03-2019, CERN, Geneva, Switzerland. https://edms.cern.ch/document/1698402/2.0.

[23] M. Bozzolan *et al.*, "LEIR Injection BPMs status update," *LIU-Ions PS injectors Beam Dynamics Working Group*, 06-08-2019, CERN, Geneva, Switzerland. https://indico.cern.ch/event/838898/.

[24] C. Carli, S. Maury, and D. Mohl, "Combined longitudinal and transverse multiturn injection in a heavy ion accumulator," in *Proceedings of the 1997 Particle Accelerator Conference (Cat. No.97CH36167)*, 1997, Vancouver, BC, Canada. http://dx.doi.org/10.1109/PAC.1997.749900.

[25] N. Biancacci, "PyHEADTAIL for coasting beams," *178th HSC meeting*, 27-05-19, CERN, Geneva, Switzerland. https://indico.cern.ch/event/819216/.

[26] A. Saa Hernandez, "Cooling maps in LEIR, or equilibrium emittances as a function of the ion orbit," *Electron cooling meeting*, 08-11-2018, CERN, Geneva, Switzerland. https://indico.cern.ch/event/770398/.

[27] N. Biancacci, H. Bartosik, A. Huschauer, M. Migliorati, E. Métral, T. Rijoff, B. Salvant, and R. Scrivens, "LEIR Impedance Model and Coherent Beam Instability Observations," in *Proceedings, 8th International Particle Accelerator Conference (IPAC 2017)*, May 14-19, 2017, Copenhagen, Denmark. https://doi.org/10.18429/JACoW-IPAC2017-WEPIK094.

[28] H. Bartosik, S. Hancock, A. Huschauer, and V. Kain, "Space charge driven beam loss for cooled beams and mitigation measures in the CERN Low Energy Ion Ring," in *Proceedings, 57th ICFA Advanced Beam Dynamics Workshop on High-Intensity and High-Brightness Hadron Beams (HB2016): Malmö Sweden, July 3-8, 2016*. http://dx.doi.org/10.18429/JACoW-HB2016-TUAM5X01.

[29] R. Alemany Fernandez *et al.*, "Update on LLRF parameters in LSA," *LIU-Ions PS injectors Beam Dynamics Working Group*, 19-11-2019, CERN, Geneva, Switzerland. https://indico.cern.ch/event/861568/.

[30] S. C. P. Albright and M. E. Angoletta, "Frequency Modulated Capture of Cooled Coasting Ion Beams," in *Proceedings, 10th International Particle Accelerator Conference (IPAC 2019)*, May 19-24, 2019, Melbourne, Australia. http://dx.doi.org/10.18429/JACoW-IPAC2019-WEPMP021.

[31] M. Martini, "Injection of the Lead Ion Beam for LHC into the PS," tech. rep., CERN-PS-AE-Note-2001-012, 2001, CERN, Geneva, Switzerland. https://cds.cern.ch/record/2270958.

[32] C. Carli *et al.*, "Design of the LEIR Transfer Lines," tech. rep., CERN-PS-AE-Note-2002-218, 2002, CERN, Geneva, Switzerland. https://cds.cern.ch/record/2318300.

[33] H. Bartosik *et al.*, "Recent beam performance achievements with the Pb-ion beam in the SPS for LHC physics runs," in *Proceedings, 10th International Particle Accelerator Conference (IPAC 2019): Melbourne, Australia, May 19-24 2019*. http://jacow.org/ipac2019/papers/mopgw069.pdf.

[34] N. Biancacci *et al.*, "Performance and reliability with ions from Linac3 to PS," *LHC Injectors Upgrade Workshop*, 13-15 February 2019, Montreaux, Switzerland. https://indico.cern.ch/event/790954.

[35] H. Bartosik *et al.*, "Transverse beam quality and stability in the SPS (protons and ions)," *LHC Injectors Upgrade Workshop*, 13-15 February 2019, Montreaux, Switzerland. https://indico.cern.ch/event/790954.

[36] R. Scrivens, "Test of Required Stability of RF Parameters on Linac3 with Pb," EDMS 2038110, 2019, CERN, Geneva, Switzerland. https://edms.cern.ch/document/2038110/1.

[37] G. Bellodi *et al.*, "Overview of Linac3 operation in 2018," *LIU-Ions PS injectors Beam Dynamics Working Group*, 05-02-2019, CERN, Geneva, Switzerland. https://indico.cern.ch/event/793971/.

[38] A. Huschauer *et al.*, "Injection line studies," *LIU-Ions MD wrap up meeting 1*, 15-01-2016, CERN, Geneva, Switzerland. https://indico.cern.ch/event/816834/.

[39] N. Biancacci *et al.*, "Discussion on stray field compensation on LEIR injection line," *LIU-Ions PS injectors Beam Dynamics Working Group*, 14-05-2019, CERN, Geneva, Switzerland. https://indico.cern.ch/event/816834/.

[40] N. Biancacci, "LEIR intensity limitations," *SPS/LEIR training*, 28-05-2019, CERN, Geneva, Switzerland. https://indico.cern.ch/event/822753/.

[41] N. Biancacci, "Horizontal instability observed in LEIR during 2018 run," *HSC meeting*, 9-12-2019, CERN, Geneva, Switzerland. https://indico.cern.ch/event/865539/.

[42] N. Biancacci, "Impedance and Beam Transfer Function Studies," *LIU-Ions PS injectors Beam Dynamics Working Group*, 16-01-2018, CERN, Geneva, Switzerland. https://indico.cern.ch/event/687751/.

[43] N. Biancacci *et al.*, "Performance tracking parameters for the ion chain," *LIU-Ions PS injectors Beam Dynamics Working Group*, 18-06-2019, CERN, Geneva, Switzerland. https://indico.cern.ch/event/827952/.

[44] A. Shishlo, S. Cousineau, J. Holmes, and T. Gorlov, "The particle accelerator simulation code pyorbit," *Procedia Computer Science, International Conference On Computational Science, ICCS 2015*, vol. 51, pp. 1272 – 1281, 2015. https://doi.org/10.1016/j.procs.2015.05.312.

[45] A. Huschauer, H. Bartosik, S. Hancock, and V. Kain, "Progress in the Understanding of the Performance Limitations in the CERN Low Energy Ion Ring," no. CERN-ACC-2017-239, p. 4, 2017. https://cds.cern.ch/record/2289166.

[46] A. Saa Hernandez, D. Moreno, H. Bartosik, N. Biancacci, S. Hirlander, and A. Huschauer, "Space charge studies on LEIR," *Journal of Physics: Conference Series*, vol. 1067, Sep. 2018. https://doi.org/10.1088/1742-6596/1067/6/062020.

[47] D. Moreno *et al.*, "LEIR Aperture Database," *LIU-Ions PS injectors Beam Dynamics Working Group*, 26-06-2018, CERN, Geneva, Switzerland. https://indico.cern.ch/event/738562/.

[48] F. Antoniou and F. Zimmermann, "Revision of Intrabeam Scattering with Non-Ultrarelativistic Corrections and Vertical Dispersion for MAD-X," Tech. Rep. CERN-ATS-2012-066, May 2012, CERN, Geneva, Switzerland. https://cds.cern.ch/record/1445924.

[49] A. S. Hernandez *et al.*, "Summary of Space charge and IBS studies (measurements and simulations) in LEIR," *LIU-Ions PS injectors Beam Dynamics Working Group*, 14-05-2019, CERN, Geneva, Switzerland. https://indico.cern.ch/event/816834/.

[50] A. Saa Hernandez, "Space charge and IBS effect in LEIR," *4th ICFA Mini-Workshop on Space Charge*, 4-6 November 2019, CERN, Geneva, Switzerland. https://indico.cern.ch/event/828559.

[51] A. Latina, H. Bartosik, N. Biancacci, R. Corsini, D. Gamba, S. Hirlander, and A. Huschauer, "Electron Cooling Simulation and Experimental Benchmarks at LEIR," in *Proceedings, 9th International Particle Accelerator Conference (IPAC 2018)*, Vancouver, BC Canada, April 29 - May 4, 2018. https://doi.org/10.18429/JACoW-IPAC2018-TUPAF039.

[52] D. Gamba *et al.*, "BE Newsletter Issue n.25," tech. rep., CERN-BE-Note-2019-001, 18-02-2019, CERN, Geneva, Switzerland. https://cds.cern.ch/record/2659571.

[53] K. N. Henrichsen and M. J. De Jonge, "Acceleration by phase displacement in the ISR," no. CERN-ISR-RF-MA-74-21, p. 4 p, Apr. 1974, CERN, Geneva, Switzerland. https://cds.cern.ch/record/312835.

[54] C. B. L. D. code, "BLonD," no. http://blond.web.cern.ch.

[55] M. Steck, K. Beckert, H. Eickhoff, B. Franzke, F. Nolden, and P. Spadtke, "Electron cooling of heavy ions at GSI," in *Proceedings of International Conference on Particle Accelerators*, pp. 1738–1740 vol.3, May 1993. https://doi.org/10.1109/PAC.1993.309117.

[56] A. Saa Hernandez and N. Biancacci, "LEIR e-cooler operational experience and needs," *E-Beam Working Group*, 10-07-2019, CERN, Geneva, Switzerland. https://indico.cern.ch/event/829076/.

[57] G. Tranquille, "Status and plans for hardware interventions on LEIR e-cooler," *E-Beam Working Group*, 10-07-2019, CERN, Geneva, Switzerland. https://indico.cern.ch/event/829076/.

[58] N. Biancacci *et al.*, "BE Newsletter Issue n.24," tech. rep., CERN-BE-Note-2018-007, 13-12-2018, CERN, Geneva, Switzerland. https://cds.cern.ch/record/2651040.

[59] N. Biancacci, "Impedance localisation and identification," in *Proceedings, ICFA mini-Workshop on Mitigation of Coherent Beam Instabilities in particle accelerators (MCBI)*, 23-27 Sep. 2019, Zermatt, Switzerland. https://indico.cern.ch/event/775147.

[60] N. Biancacci, E. Métral, M. Migliorati, and T. L. Rijoff, "LEIR impedance model and coherent beam instability observations," in *Proceedings, Injector MD Days*, pp. 129–132, CERN. Geneva, Switzerland, March 23-24, 2017. https://doi.org/10.23727/CERN-Proceedings-2017-002.129.

[61] G. Kotzian *et al.*, "Transverse damper: outcome of matching load inspection and plans for 2021," *LIU-Ions PS injectors Beam Dynamics Working Group*, 02-04-2019, CERN, Geneva, Switzerland. https://indico.cern.ch/event/809078/.

[62] S. Albright, "Overview of longitudinal beam dynamics studies in 2018," *LIU-Ions PS injectors Beam Dynamics Working Group*, 02-04-2019, CERN, Geneva, Switzerland. https://indico.cern.ch/event/809078/.